Master Thesis

Cooling Circuit Design for the Large-Scale Liquid Argon Detectors in the ICARUS Experiment

Hannah Kirsch

06.07.2016

Supervision: Dr. Torsten Koettig, CERN

Assignment: Prof. Dr.-Ing. Steffen Grohmann, KIT

Second Corrector: Prof. Dr.-Ing. Dr. h. c. Wilhelm Schabel, KIT

Institute of Technical Thermodynamics
and Refrigeration

KIT - university of the state of Baden-Württemberg and
national research center of the Helmholtz Association

Karlsruher Institut für Technologie

Institute of Technical Thermodynamics and Refrigeration (ITTK)

Head: Prof. Dr. habil. rer. nat. Sabine Enders

Engler-Bunte-Ring 21
76131 Karlsruhe, Germany

Phone: +49 721-608-4-2332
Fax: +49 721-608-4-2335
E-Mail: steffen.grohmann@kit.edu
Web: www.ttk.kit.edu

KIT-Campus South | ITTK | Engler-Bunte-Ring 21 | 76131 Karlsruhe, Germany

Official in charge: Prof. Dr.-Ing. Steffen Grohmann
Our reference:
Date: 27.10.2015

Thesis Topic

Cooling circuit design for the large-scale liquid argon detectors in the ICARUS experiment

Type: Master Thesis

Focus: ■ Literature study ☐ Theory ■ Design ■ Experiment

Supervision: Dr. Torsten Koettig (CERN), +41 22 767.7944, torsten.koettig@cern.ch

Assignment: Prof. Dr.-Ing. Steffen Grohmann

Scope of Work

The objective of this master thesis is to investigate design details of a liquid nitrogen cooling system for the large-scale liquid argon detectors in the ICARUS experiment. The thesis will focus on the design of the two-phase cooling circuit and its functional specification for cool-down, steady-state operation and warm-up. The special demands of large-volume liquid argon vessels are to be considered, especially in terms of cryogenic safety.

The thesis project comprises the following work packages:

- Study of the project for the ICARUS detector upgrade at CERN
- Literature research related to two-phase flow cooling options and related thermodynamic parameters
- Measurement of the pressure drop in the existing mock-up structure of the ICARUS thermal shield panels in the Cryolab at CERN
- Comparison of the numerical calculations of pressure drop in two-phase flow conditions (vertical and horizontal flow directions) with the experimental data
- Study of the cool-down behavior of the mock-up panel with regard to the full-scale detector cool-down strategy consisting of 42 parallel panel circuits
- Safety analysis of the cooling system

The master thesis shall be written in English language. A two-sided summary in German must be submitted together with the thesis.

Name of Student: Kirsch, Hannah Marie

Start of Work: 06.01.2016

27.10.2015, Prof. Dr.-Ing. S. Grohmann

Selbständigkeitserklärung

Hiermit erkläre ich, dass ich folgende Arbeit selbständig verfasst und keine anderen als die von mir angegebenen Quellen und Hilfsmittel benutzt habe, die wörtlich oder inhaltlich übernommene Stellen als solche kenntlich gemacht und die Satzung des Karlsruher Instituts für Technologie (KIT) zur Sicherung guter wissenschaftlicher Praxis in der jeweils gültigen Fassung beachtet habe. Ich erkläre mich damit einverstanden, dass die Arbeit in die Bibliothek eingestellt und kopiert werden darf.

Datum Unterschrift

Acknowledgements

First of all, I would like to express my sincere gratitude to Professor Grohmann. He encouraged me to participate in the Technical Student Programme at CERN and supported my application. By his personal support he made this external Master Thesis possible.

Special thanks also goes to my supervisor at CERN, Dr. Torsten Koettig. He made it easy to feel at home at the Cryolab. I really appreciated his vivid introduction into the world of particles and accelerators as well as cryogenics. His theoretical and practical support was crucial for this work.

Moreover, many thanks to all the staff, PhD students, fellows, students and technicians of the Cryolab I met during my stay at CERN. Here, in particular, Dario Santandrea should be mentioned, with whom I worked together on the ICARUS project.

Zusammenfassung

Der ICARUS Detektor wurde entwickelt, um Neutrinos zu detektieren und das Phänomen der Neutrinooszillation näher zu untersuchen. Der Detektor wird mit flüssigem Argon gefüllt und arbeitet bei Umgebungsdruck, wodurch die Temperatur des Detektors auf die Sättigungstemperatur des Argons von 87 K festgelegt ist. Damit die Wechselwirkungen zwischen den Neutrinos und den Argon Atomen möglichst genau rekonstruiert werden können, müssen Temperaturgradienten innerhalb des Argons und die daraus resultierenden Konvektionen minimiert werden. Daher ist der ICARUS Detektor mit einem thermischen Schild, das nahezu den ganzen Wärmeeintrag aus der Umgebung abschirmt, ummantelt. Das thermische Schild wird mit siedendem Stickstoff auf Detektortemperatur gekühlt. Das Kühlsystem des thermischen Schildes arbeitet bei einem Druck von 2,8 bar, was dem Sättigungsdampfdruck von Stickstoff bei 87 K entspricht. Als Kühlmittel wurde Stickstoff im Siedezustand gewählt, da in erster Näherung bei Annahme einer druckverlustfreien Strömung die Temperatur während des Verdampfens des Stickstoffs konstant bleibt. Ein Druckverlust einer Strömung im Zweiphasengebiet ist jedoch immer mit einem Temperaturabfall korreliert. Aus diesem Grund ist es wichtig, den Druckverlust der Stickstoff-Zweiphasenströmung über die Länge des Kühlsystems genau bestimmen zu können.

Im Rahmen dieser Masterarbeit wird der Druckverlust einer Stickstoff-Zweiphasenströmung unter den Bedingungen, wie sie später im thermischen Schild auftreten werden, untersucht. Dies entspricht einem Druck von 2,8 bar, Massenstromdichten von $20\,\mathrm{kg\,m^{-2}\,s^{-1}}$ bis $70\,\mathrm{kg\,m^{-2}\,s^{-1}}$ und Gasgehalten bis zu 70 %. Da die Wechselwirkungen der Gas- und der Flüssigphase einer Zweiphasenströmung noch nicht vollständig verstanden sind, basieren viele in der Literatur dargestellten Duckverlustkorrelationen auf empirischen Daten, was deren Übertragbarkeit auf andere Fluide sowie Drücke und Massenstromdichten einschränkt. Die berechneten Druckverluste der Stickstoff-Zweiphasenströmung über die Länge des thermischen Schildes mit Hilfe verschiedener ausgewählter Korrelationen aus der Literatur weichen stark voneinander ab. Dies unterstreicht die Notwendigkeit, den Druckverlust im Bereich der interessierenden Bedingungen experimentell zu untersuchen.

Nach einer kurzen Einführung in die Physik der Neutrinos und in das Konzept des ICARUS Detektors werden die theoretischen Grundlagen einer Zweiphasenströmung insbesondere des Druckverlustes in der Zweiphasenströmung behandelt. Es wird ein Überblick

über einige in der Literatur existierende empirische Korrelationen für den Gasanteil und den Reibungsdruckverlust gegeben. Das nächste Kapitel beschreibt das in Matlab® entwickelte mathematische Modell um den Druckverlust von Stickstoff-Zweiphasenströmungen im Druckbereich von 2,6 bar bis 2,9 bar zu berechnen. Das Programm koppelt die Energieerhaltungsgleichung mit der Impulserhaltungsgleichung, um dem Phänomen Rechnung zu tragen, dass sich der Gasgehalt einer Zweiphasenströmung sogar unter adiabatischen Bedingungen aufgrund des Druckverlustes über die Rohrlänge ändert. Im Mittelpunkt des darauffolgenden Kapitels steht der Versuchsaufbau zur Bestimmung des Druckverlustes einer siedenden Stickstoffströmung unter den oben genannten Bedingungen. Die Teststrecke wird unter quasi-adiabatischen Bedingungen betrieben und setzt sich aus einem horizontalen, einem vertikal aufwärtsgerichteten und einem vertikal abwärtsgerichteten Teil zusammen. Die erhaltenen Messdaten stellen eine erste Datenbank für den Druckverlust von Stickstoff im Zweiphasengebiet unter den oben genannten Bedingungen dar. Durch einen Vergleich der Messdaten mit den berechneten Daten aus dem Matlab® Programm wird die Korrelation für den Gasanteil und den Reibungsdruckverlust der untersuchten Stickstoff-Zweiphasenströmung bestimmt, die die Messdaten mit der geringsten Abweichung wiedergibt. Die Korrelation nach Rouhani für den Gasgehalt sowie das Modell nach Müller-Steinhagen und Heck für den Reibungsdruckverlust bilden am besten die gemessenen Daten für eine horizontale Strömung oder vertikale Aufwärtsströmung ab. Bei vertikaler Abwärtsströmung tritt, im Gegensatz zu der Berechnung, in den gemessenen Werten keine Drucksteigerung auf. Zudem wird das Abkühlverhalten des Versuchsaufbaus ausgehend von Raumtemperatur untersucht. Im letzten Teil dieser Arbeit werden die durch den Versuchsaufbau erhaltenen Erkenntnisse angewendet, um den Druckverlust im realen Kühlsystem des thermischen Schildes des ICARUS Detektors zu berechnen und ein Vorschlag für die Gestaltung des Kühlsystems wird unterbreitet. Das Kühlsystem kann die Forderung nach einem Temperaturgradienten von maximal 500 mK einhalten. Da sich in kryogenen Systemen bei ungewolltem Wärmeeintrag hohe Drücke aufbauen können, werden die an die erforderlichen Sicherheitsvorkehrungen gegen exzessiven Überdruck in Form von Sicherheitsventilen oder Berstscheiben gesetzten Anforderungen betrachtet.

Contents

1 Nomenclature

A	cross-section (m^2)
C	flow coefficient (-)
C_0	parameter drift-flux model (-)
c_p	specific heat capacity ($\frac{J}{kg \cdot K}$)
d	inner diameter (m)
f	friction factor (-)
F_D	parameter flow pattern map Taitel and Dukler (-)
g	acceleration due to gravity ($\frac{m}{s^2}$)
G	mass flow density / mass velocity ($\frac{kg}{m^2 \cdot s}$)
h	enthalpy ($\frac{J}{kg}$)
i	momentum flow density / momentum velocity ($\frac{kg}{m \cdot s^2}$)
J	volumetric flow density / volumetric velocity ($\frac{m^3}{m^2 \cdot s}$)
K_D	parameter flow pattern map Taitel and Dukler (-)
K_d	safety valve discharge coefficient (-)
L	length (m)
$\dot{m}$	mass flow ($\frac{kg}{s}$)
N	boiling delay factor (-)
P	power (W)
p	pressure (bar)
T	temperature (K)
$\dot{q}$	heat flux ($\frac{W}{m^2}$)
$\dot{Q}$	heat flow (W)
Re	Reynolds number (-)
S	slip ratio (ratio of velocity vapour phase to velocity liquid phase) (-)
t	time (s)
u	velocity ($\frac{m}{s}$)
u_{vj}	parameter drift-flux model ($\frac{m}{s}$)
v	specific volume ($\frac{m^3}{kg}$)
$\dot{V}$	volumetric flow ($\frac{m^3}{s}$)

x	flow quality (-)
X	Lockart-Martinelli parameter (-)
z	length along z-axis (m)

Greek letters

ϵ	void fraction (-)
κ	ideal isentropic coefficient (-)
λ	thermal conductivity ($\frac{\mathrm{W}}{\mathrm{m \cdot K}}$)
α_{d}	rupture disk discharge coefficient (-)
μ	dynamic viscosity ($\mathrm{Pa \cdot s}$)
ν	kinematic viscosity ($\frac{\mathrm{m}^2}{\mathrm{s}}$)
ρ	density ($\frac{\mathrm{kg}}{\mathrm{m}^3}$)
ϕ	two-phase multiplier (-)
φ	inclination angle of the pipe
ω	factor describing compressibility (-)

Subscripts

0	set pressure conditions
b	back pressure conditions
c	critical point
crit	sonic flow
cs	cross-sectional
f	frictional
g	gravitational
hom	homogeneous
in	flow inlet
l	liquid
m	melting
mom	momentum
out	flow outlet
p	pipe
r	reduced
sat	saturation
tot	total
v	vapour, evaporation
vol	volumetric
2ph	two-phase

2 Introduction

CERN, whose name originally derived from Conseil Européen pour la Recherche Nucléaire, is the European Organization for Nuclear Research located along the French-Swiss border near Geneva. CERN was founded in the year 1954 as Europe's first joint venture and nowadays belongs to the best research organizations for particle physics around the globe. Physicists as well as engineers are dedicated to explore the fundamental structure of our universe - the constituents of matter and the forces between them. A complex of particle accelerators increases the speed of particles almost to the speed of light and let them collide purposely. Detectors provide information about the particle interactions and the released fragments. The technology used is at the forefront of science combining knowledge from 21 member states and many collaborations.[1]

A collaboration between the US Fermi National Accelerator Laboratory (Fermilab), the Italian Institute for Nuclear Physics (INFL) and CERN is currently working on the ICARUS neutrino experiment. The large-scale ICARUS T600 detector is designed to be filled with liquid argon and to detect neutrinos allowing research in the field of neutrino oscillations [2]. The Cryolab at CERN was assigned the task to investigate the details of the thermal shield design for the ICARUS T600 detector taking into account the constraints given by the experiment. The thermal shield is actively cooled with boiling nitrogen and operates at a pressure of 2.8 bar, which corresponds to a saturation temperature of 87 K. The thermal shield should have a temperature gradient less than 500 mK. Theoretically, not considering the pressure drop along the cooling circuit, the temperature stays constant during evaporation in the chosen two-phase flow regime. The only temperature change is caused by the small pressure drop along the cooling loop. Due to the strict temperature constraints, it is important to study the pressure drop of nitrogen two-phase flow along the cooling circuit of the thermal shield in different orientations of the flow in respect to gravity.

The objective of this master thesis is to investigate the proposed design of the thermal shield of the ICARUS detector especially the pressure drop along the nitrogen two-phase flow cooling circuit. After a short introduction to the fundamentals of neutrino physics and the design of the ICARUS T600 detector, the presented master thesis introduces the distinctive characteristics of two-phase flow such as flow quality, flow pattern, void fraction

and two-phase pressure drop. At the same time it gives an overview of the existing literature of two-phase flow. As the mechanism of two-phase flow have not been fully understood yet, most phenomena, especially the void fraction and the frictional pressure drop, are described by empirical correlations. This makes it difficult to utilize these correlations at other applications as they were originally developed for, e.g. changing fluid properties, range of mass flow or pipe diameter. Applying selected models from literature to boiling nitrogen at the conditions of the ICARUS thermal shield show rather high deviations, underscoring the need for a study of nitrogen two-phase flow at that conditions. The following part of the master thesis describes the developed Matlab® program for computing the pressure drop of nitrogen two-phase flow. Subsequently, the experimental setup, designed to measure the pressure drop of nitrogen two-phase flow, is presented and the obtained measurement results are presented and discussed. The measurements have been conducted in a quasi-adiabatic test section, comprising a horizontal, vertical upward and vertical downward part. The pressure has been regulated at 2.8 bar, the mass velocity has been varied in a range of about $20\,\mathrm{kg\,m^{-2}\,s^{-1}}$ to $70\,\mathrm{kg\,m^{-2}\,s^{-1}}$ and the two-phase area has been scanned from flow qualities close to zero to about 70 %. The best correlations for nitrogen two-phase flow at the conditions of the ICARUS thermal shield are determined by comparing the measurement data with the calculated data of the program applying different correlations. Moreover, the cool-down behaviour of the experimental setup is studied. The findings of the experimental setup enable an up-scaling to the large-scale thermal shield. The last part of this master thesis proposes a design for the real cooling system of the ICARUS T600 thermal shield including basic safety considerations.

3 Important basics of neutrino physics

In the year 1930 Wolfgang Pauli postulated the existence of a further lepton today called neutrino. During studies of the radioactive β^--decay several physicians figured out that the generated electrons show a continuous energy spectrum. But if, as previously assumed, during a β^--decay a neutron decays only into a proton and an electron, the energy of the electron should be constant according to the law of energy conservation. By introducing a third emitted uncharged particle, the neutrino, Pauli was now able to explain the continuous energy spectrum of the electrons. Thus, the released energy of the β^--decay is distributed between three particles, whereby the sum of the energy of the electron and the neutrino has to be constant. At one extreme, the electron absorbs the total kinetic energy, whereas the neutrino absorbs no energy. This corresponds to the upper limit of the observed electron energy spectrum. At the other extreme, the neutrino carries away all the energy. This corresponds to the lower limit of the observed electron energy spectrum. Finally, in the year 1956 Cowan and Reines succeeded in verifying electron neutrinos emitted by a nuclear reactor [3]. The following reaction describes the β^--decay of a neutron (It is not sure if neutrinos are Dirac particles or Majorana particles. In the latter case the particle and antiparticle would be identical [4]):

$$\mathrm{n} \longrightarrow \mathrm{p}^+ + \mathrm{e}^- + \bar{\nu}_\mathrm{e} \quad . \tag{3.1}$$

Neutrinos are abundant. Almost 10^{11} neutrinos are penetrating the earth per square centimetre and second [4]. There are mainly four different natural sources of neutrinos [3]:

- Solar neutrinos of various energy are created by the sequence of nuclear fusion reactions in the sun.
- Cosmic neutrinos are generated by the explosion of stars, known as supernova.
- Atmospheric neutrinos are formed when pions, originally released in the particle shower of atmospheric reactions triggered by cosmic rays, decay.
- Reactor neutrinos are evolved by multiple reactions, e.g. β^--decay.

In accelerators and laboratories neutrinos are produced artificially by mostly shooting accelerated protons with a high energy on a fixed target. The sputtered kaons and pions

are instable and neutrinos are released in the course of their decay series. One challenge is to focus the beam of neutrinos as the kaons and pions are escaping from the target material at many different angles. As neutrinos are neutral it is impossible to focus them by the means of electromagnetic fields. The only possibility is to already concentrate the charged kaons and pions [5]. Nevertheless, neutrinos are not easy to detect as they are uncharged and are only interacting with matter by weak interaction via charged-current reactions (W-exchange) or neutral-current reactions (Z-exchange) [3].

Neutrinos feature some special characteristics. The idea of neutrino oscillations was first proposed by Pontecorvo in the 1950s [3]. According to the present accepted model three different types of neutrinos exist: electron neutrinos ν_e, myon neutrinos ν_μ, and tau neutrinos ν_τ. These so-called flavour states are defined by the following matrix [4]:

$$\begin{pmatrix} \nu_\mathrm{e} \\ \nu_\mu \\ \nu_\tau \end{pmatrix} = \begin{pmatrix} \mathrm{U_{e1}} & \mathrm{U_{e2}} & \mathrm{U_{e3}} \\ \mathrm{U}_{\mu 1} & \mathrm{U}_{\mu 2} & \mathrm{U}_{\mu 3} \\ \mathrm{U}_{\tau 1} & \mathrm{U}_{\tau 2} & \mathrm{U}_{\tau 3} \end{pmatrix} \cdot \begin{pmatrix} \nu_1 \\ \nu_2 \\ \nu_3 \end{pmatrix} \quad , \tag{3.2}$$

where each neutrino (ν_e, ν_μ, ν_τ) is a mixture of different mass states with specified mass (ν_1 to ν_3). Depending on the mixing proportion of the three mass states the flavour state is determined. That means, if a neutrino with a specific energy is emitted, the different mass states of this neutrino will travel at different velocities. Hence, while moving the mixture of the mass states is changing and the neutrino forms another flavour state [3]. The periodically changing probability of the transformation is described by equation (3.3). The oscillation probability depends on the difference of the squared masses of each state. The more distinct the mass differences are, the higher is the frequency of the oscillation [4].

$$\mathrm{P}_{\nu_\mathrm{x} \to \nu_\mathrm{y}} = \sin^2 2\theta \sin^2 \left(\frac{1}{4} \frac{\Delta \mathrm{m}^2_\mathrm{xy} \mathrm{c}^4}{\hbar \mathrm{c}} \frac{\mathrm{L}}{\mathrm{pc}} \right) \tag{3.3}$$

θ is the Cabbibo angle, $\hbar$ is the reduced Planck constant, c is the speed of light, m is the mass, p is the momentum and L is the distance the particle travelled.

Neutrino oscillation experiments are mostly based on one of the two following fundamental principles. There is always a source, which emits a specific flavour of neutrinos, as well as the detector is especially sensitive for one specific flavour state. According to equation (3.3), the probability of neutrino oscillations from one flavour to another depends on the energy of the neutrinos and on the distance between neutrino production and detection. By varying these two parameters, the sensitivity of the detector for one specific oscillation process (e.g.: myon neutrino $\longrightarrow$ tau neutrino) can be increased maximizing the probability of that special process with respect to the others. Either one quantifies the

disappearance of one flavour state of neutrinos by measuring a lower flux than expected or one quantifies the appearance of one flavour state, which is not generated by the source [5]. One of several neutrino detectors is the ICARUS T600 detector, which will be introduced in the next chapter. Last year, Takaaki Kajita and Arthur B. McDonald were awarded the Nobel Prize in Physics for their unambiguous evidence of neutrino oscillations [6].

Since the last few years physicians have even considered an additional, yet unknown flavour state of neutrinos. Some data anomalies have been observed in several neutrino oscillation experiments, especially at short distances, too few or too many neutrinos of one kind with respect to expectations. The potentially new flavour state is designated as sterile state as it shows no or very rare interaction with ordinary matter. It should have a far larger mass difference with standard neutrinos and their oscillation probability should be very high at short distances [7].

From the oscillation feature another important characteristic of neutrinos can be deduced. If neutrinos are oscillating between the different flavour states and equation (3.3) holds, neutrinos, by implication, must possess a mass and the different kinds of neutrinos must have a different mass. However, it has not been possible so far to measure the exact mass of neutrinos [4]. The mass of all kinds of neutrinos is by a factor 10^6 smaller than the mass of their corresponding charged particles and lies below the threshold of $2.3\,\mathrm{eV\,c^{-2}}$ for electron neutrinos, $0.17\,\mathrm{MeV\,c^{-2}}$ for myon neutrinos and $15.5\,\mathrm{MeV\,c^{-2}}$ for tau neutrinos [6]. It is assumed that, in correspondence with the mass of the other leptons, the mass of the different neutrino flavours is increasing by each generation. That means, the electron neutrino is the lightest and the tau neutrino is the heaviest [6]. If neutrinos have a mass, they could also help to explain the still unsolved problem of dark matter [3].

4 The neutrino detector "ICARUS T600"

The ICARUS T600 detector ("Imaging Cosmic and Rare Underground Signal") is the largest Liquid-Argon Time Projection Chamber (LAPC) constructed and functional up to now. It has been designed to detect neutrinos allowing research in the field of neutrino oscillations. From May 2010 to June 2013 the detector was installed in the underground Gran Sasso Laboratory, Italy. It collected data from cosmic rays as well as using a beam of myon neutrinos generated at CERN and sent 732 km through the earth to Gran Sasso [7, 8]. The neutrinos at CERN were produced by protons from the SPS (Super Proton Synchrotron) hitting a beryllium target. The released mesons are decaying into myons and then into electrons creating mainly myon neutrinos and a fraction of electron neutrinos (concentration of electron neutrinos about $1 - 2\,\%$). Hence, the ICARUS T600 detector aimed to study mainly oscillations from myon neutrinos to tau neutrinos [5]. It detected 2500 neutrinos during the three years of experiments. At the end of 2014 the detector was brought to CERN where it is refurbished and upgraded within the WA-104 program. In 2017, the detector will be sent to Fermilab, USA. It is expected to operate within a series of three detectors at a distance of 600 m from the neutrino beam source, which produces neutrinos at lower energy. The forthcoming experiments at Fermilab should further investigate the phenomena of neutrino oscillations and collect data, which especially enable researchers to validate or invalidate the theory of the so-called sterile flavour state of neutrinos [7, 8].

4.1 The ICARUS T600 detector as Liquid-Argon Time Projection Chamber (LAPC): neutrino detection concept

The idea of the Liquid-Argon Time Projection Chamber (LAPC) was originally developed by Rubbia in 1977 [9]. It should satisfy the needs for a neutrino detector with a large sensitive mass, which delivers specific information about time, topology and energy of the detected particle events. The interaction of a neutrino and an argon atom results in an ionization of the latter producing an electron and an anion as well as a discharge of photons at an energy level in the ultraviolet light range. The photons are detected instantly by photomultipliers and the charged particles are separated by the electric field and drift

towards the electrodes where they are detected. With all these signals a 3-D-image of the particle tracks is captured and the drift velocity of the electrons is computed providing calorimetric details of the incident.

Rubbia regarded liquid argon as an appropriate target material for neutrinos as listed below.

- Liquid argon has a high density ($\rho_{\mathrm{LAr}} = 1396\,\mathrm{kg\,m^{-3}}$ for $p_{\mathrm{sat}} = 1\,\mathrm{bar}$ and $T_{\mathrm{sat}} = 87\,\mathrm{K}$) enhancing the probability of an interaction with a neutrino.
- Argon is an inert noble gas with a completely filled valence shell. It allows electrons to pass through unimpededly. The high electron mobility is an essential property of the target material as otherwise the electrons emitted by a neutrino-argon interaction are recaptured on their way to the cathode and cannot be detected. Consequently, the argon also has to be very pure what brings up the next point.
- Liquid argon is easy to purify as most organic contaminations are frozen out at $p_{\mathrm{sat}} = 1\,\mathrm{bar}$ and $T_{\mathrm{sat}} = 87\,\mathrm{K}$. In contrast oxygen, which easily traps electrons, is not frozen out at $T = 87\,\mathrm{K}$ because of its low melting point ($T_{\mathrm{m,O_2}} = 54\,\mathrm{K}$ at $p = 1\,\mathrm{bar}$). Therefore, special filters are inserted in the argon cooling circuit to keep the oxygen content below 0.1 ppb. One possible source of oxygen can be the outgassing of metals.
- Argon is relatively cheap.
- Argon at ambient pressure can be liquefied by liquid nitrogen at a moderate pressure of 2.8 bar.

In contrast, xenon as an additional noble gas with a high density ($\rho_{\mathrm{LXe}} = 2944\,\mathrm{kg\,m^{-3}}$ for $p_{\mathrm{sat}} = 1\,\mathrm{bar}$ and $T_{\mathrm{sat}} = 165\,\mathrm{K}$) is much more expensive and not available at large quantities. Moreover, it cannot simply be liquefied at ambient pressure by liquid nitrogen as the saturation temperature of xenon at ambient pressure lies above the critical temperature of nitrogen ($T_{\mathrm{c,N_2}} = 126\,\mathrm{K}$, $p_{\mathrm{c,N_2}} = 34\,\mathrm{bar}$). That would require a transcritical cooling process at extreme pressure.

4.2 Components and thermodynamic operation conditions of the ICARUS T600 detector

The ICARUS T600 detector is composed of two mirrored modules with the following dimensions each: width 3.6 m, height of 3.9 m, length 19.6 m. The detector has a capacity of 760 tons (476 tons active mass) of liquid argon. Each module is again divided along the long side into two chambers by a cathode, which is hence shared between the two

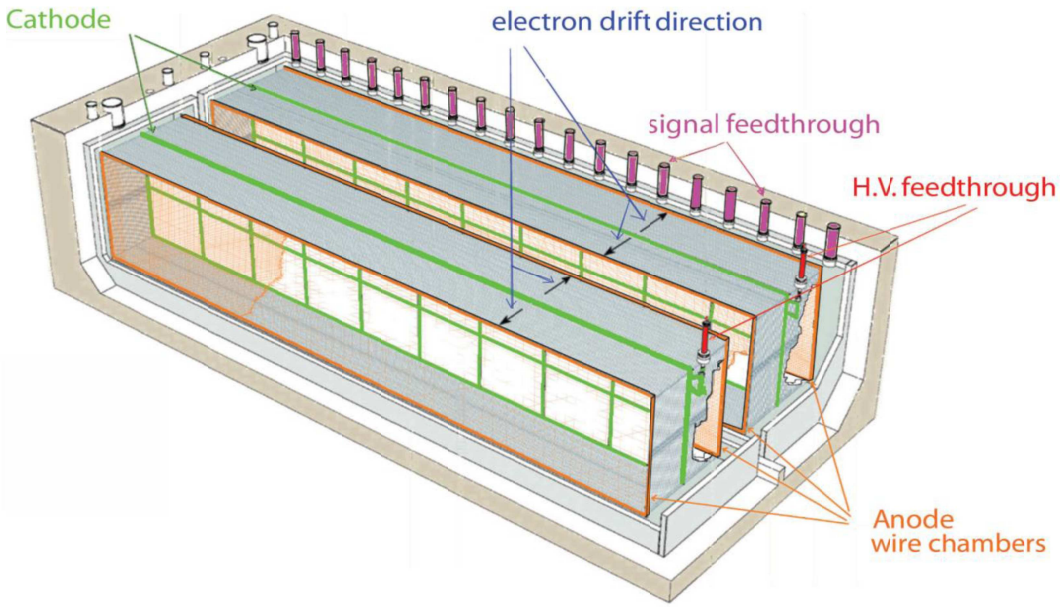

Fig. 4.1: Schematic of the ICARUS T600 detector [8].

chambers of one module. On the opposite side of the cathode all four chambers have an anode. This anode consists of around 54000 wires, which are arranged with a 3 mm pitch in three different parallel planes at different angles of 0°, ± 60°. The created uniform electric field has an intensity of 500 V m^{-1}. The photomultipliers are mounted behind the anode [8]. Figure 4.1 illustrates the design of the ICARUS T600 detector.

The whole ICARUS T600 detector is located inside a cryostat. Because of the detector's large size its operation is only feasible at ambient pressure. Thereby, the operation temperature of the detector is specified at 87.2 K, the saturation temperature of argon at ambient pressure. Due to safety reasons the pressure in the detector must be kept within a small margin of +20 mbarg and −5 mbarg. This implies a careful choice of the safety equipment. The pressure relief valves must have set points near ambient pressure, but should at the same time be leak-tight. This pressure range corresponds, assuming saturation conditions, to an allowed temperature range of +187 mK and −48 mK. The liquid argon is cooled by boiling nitrogen as a coolant. The pressure of the nitrogen has to be kept at around 2.8 bar. At ambient pressure the melting point of argon is with 83.8 K not much lower than the saturation temperature of 87.2 K. Freezing argon, meaning a pressure reduction

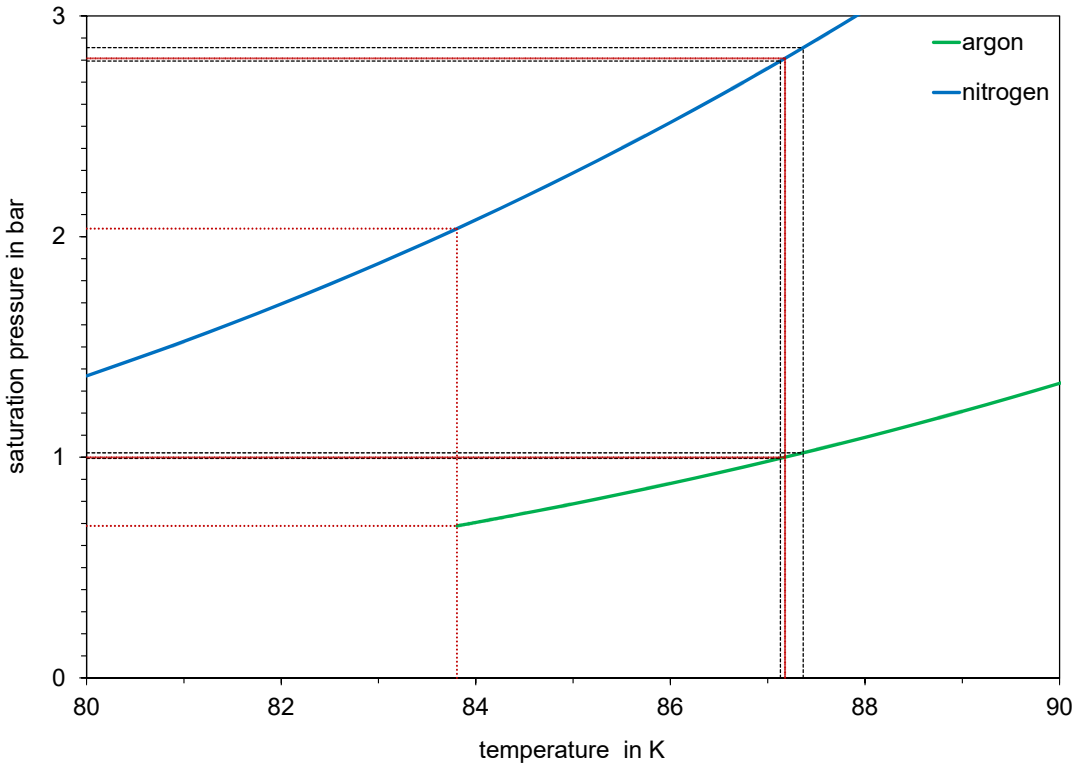

Fig. 4.2: Pressure-temperature-diagram with vapour pressure curves of argon and nitrogen. Indicated are the maximal variations of the argon pressure (limits of the cryostat) and its implications for the stability of the nitrogen cooling loop around 2.8 bar.

of the cooling nitrogen system below approximately 2.04 bar, must be prevented under all circumstances. Figure 4.2 shows the p-T-diagram with the vapour pressure curves of argon (in green) and nitrogen (in blue) highlighting the thermodynamic relations. The red line shows the operation of the argon-boiling nitrogen cooling system at the nominal point of 1 bar pressure. The black dashed lines indicate the small margin, in which the system has to be stabilized. The red dotted line shows the conditions at the melting point of argon at ambient pressure.

4.3 The thermal shield of the ICARUS T600 detector and its cooling concept

Owing to the strict constraints mentioned above it is crucial to properly insulate the cryostat against the environment diminishing the heat input from the outside. Liquid argon has a low thermal conductivity ($\lambda_{\mathrm{LAr}} = 0.13\,\mathrm{W\,m^{-1}\,K^{-1}}$ at $p_{\mathrm{sat}} = 1\,\mathrm{bar}$ and $T_{\mathrm{sat}} = 87\,\mathrm{K}$)

enabling to maintain big temperature gradients in liquid argon, causing convection. Such convectional flow of liquid argon inside the detector should be prevented as it disturbs the precise detection of the particle events. Because of the detector's large size the vessel is not vacuum-insulated but insulated by the help of an actively cooled thermal shield and a 600 mm thick polyurethane foam insulation. It is important to emphasize that the cooling system of the thermal shield is independent from the main cooling system of the liquid argon.

The Cryolab at CERN was assigned the task to support the design of the thermal shield for the ICARUS T600 detector. The thermal shield is responsible of reducing the heat input from the surrounding environment into the cryostat and thus enables to keep the liquid argon inside the detector within the required temperature range. The thermal shield should be at the same temperature of 87 K as the liquid argon inside the detector to minimize the driving temperature gradient of the heat transfer. As coolant for the thermal shield nitrogen in the two-phase flow condition was chosen and the thermal shield is kept at dry nitrogen gas atmosphere. Theoretically, not taking into account the pressure drop, the nitrogen two phase flow can absorb a large amount of heat ($\Delta h_\mathrm{v} = 185\,\mathrm{kJ\,kg^{-1}}$ at $T_\mathrm{sat} = 87\,\mathrm{K}$) without changing temperature, as the temperature is constant during evaporation. However, a pressure decrease due to a pressure drop along the thermal shield always corresponds to a temperature decrease in the two-phase area. The temperature change is normally much smaller than in single-phase flow, but has to be taken into account due to the strict temperature constraints of the thermal shield. To realize a saturation temperature of 87 K the cooling system has to be operated at 2.8 bar. The thermal shield should meet the following conditions: It should be able to handle an outer heat flux density of $20\,\mathrm{W\,m^{-2}}$ along one shield panel of approximately 11 m including the shield width. At the same time the maximum temperature gradient should be less than 500 mK. It should be made by aluminium 1050A with a very high purity characterized by a low weight and a high thermal conductivity in comparison for example to ordinary steel ($\lambda_\mathrm{Al1050A} = 270\,\mathrm{W\,m^{-1}\,K^{-1}}$ at 87 K). By the help of an Ansys simulation as well as an experimental setup the thermal shield was designed as a combination of several panels. Each 4 mm thick panel has a width of 472 mm. In the middle of each panel the pipe with an inner diameter of 10 mm is located (see figure 4.3). Each panel will be extruded with that geometry. The panels are assembled around the whole detector. There are 42 C-shaped panels at the bottom and top as well as at the long side of each module of the detector and there are 8 vertical panels at both frontal sides of each module. The manifold for the inlet of the nitrogen two-phase flow into each panel is between the two modules at the bottom of the detector and consequently the outlet is at the top. It is planned for the nitrogen two-phase flow to have two horizontal flow sections and one vertical upward flow section,

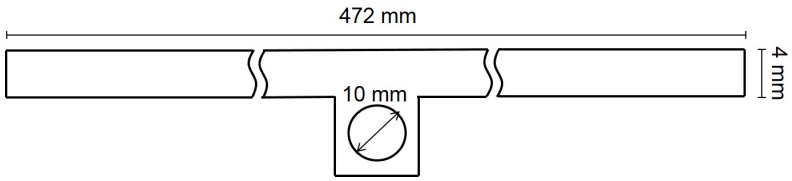

Fig. 4.3: Drawing of one cooling panel stating the dimensions.

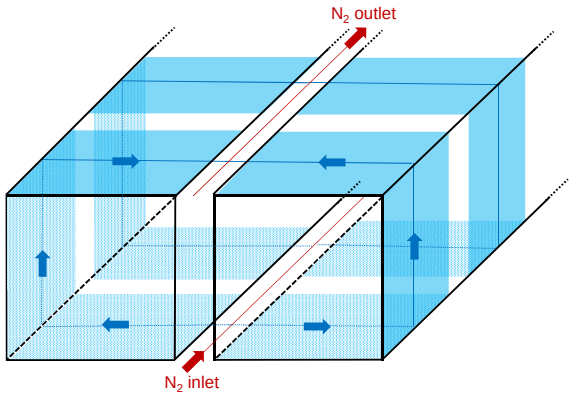

Fig. 4.4: Schematic of the cooling panels around the ICARUS T600 detector.

see picture 4.4. A mass flow of $2\,\mathrm{g\,s^{-1}}$ nitrogen in each panel is necessary to fulfil the requirements of a temperature gradient less than 500 mK, see Ansys simulation figure 4.5. The in total sixteen panels at the front and back side require a mass flow of $0.7\,\mathrm{g\,s^{-1}}$ each, as they are smaller. The total mass flow through the thermal shield is $179.2\,\mathrm{g\,s^{-1}}$. The inlet flow quality is chosen to be 10 %.

In a further step the pressure drop within the thermal shield, leading to a temperature drop, should be investigated, which is the focus of the presented work.

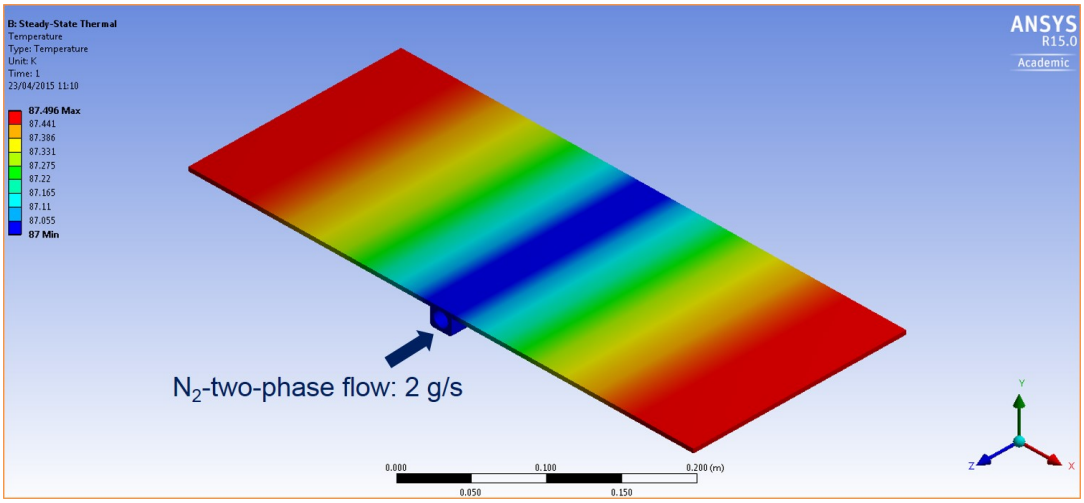

Fig. 4.5: Ansys simulation of the heat distribution in the cross-section of one cooling panel. The temperature rises from the middle of the panel towards the edges. Dark blue indicates the lowest temperature of 87 K and red indicates the highest temperature of 87.496 K, Courtesy D. Santandrea.

5 Nitrogen two-phase flow as refrigerant for the cooling of the thermal shield

Two-phase flow describes the condition if a liquid and gaseous substance is flowing simultaneously through a piping device. The gaseous substance can be the corresponding vapour to the liquid as well as another gas such as air. As in the case of nitrogen two-phase flow the former is true, the gaseous substance is in the following always referred to as vapour. Two-phase flow is essentially different from single-phase flow because of the interaction between the two phases. Since the second half of the nineteenth century a lot of research has been performed in the field of two-phase flow [10]. A good introduction to two-phase flow provide [11] and [12] and the content of this chapter is, unless otherwise specified, based on them.

5.1 Important characteristics of two-phase flow

The condition of two-phase flow is characterized by the following three important attributes: the flow quality, the flow pattern and the void fraction.

5.1.1 Flow quality

One characteristic parameter of two-phase flow is the flow quality x, see equation (5.1). The flow quality indicates the ratio of the mass flow of the vapour phase to the total mass flow.

$$x = \frac{\dot{m}_\mathrm{v}}{\dot{m}_\mathrm{l} + \dot{m}_\mathrm{v}} = \frac{\dot{m}_\mathrm{v}}{\dot{m}_\mathrm{tot}} \tag{5.1}$$

5.1.2 Flow pattern

However, the flow quality is not able to completely characterize the state of two-phase flow. The distribution of the two phases across the cross-sectional area of the pipe, the so-called flow pattern, is essential for further analysis of the flow giving information about the extent of the phase boundary and the interaction of the two phases. Momentum exchange as well as mass and heat transfer between the two phases, thus pressure drop and heat transfer

coefficients are influenced by the flow regime. In addition to the fluid properties the flow quality x and the mass flow density G are crucial to define the flow pattern. Moreover, the interaction between the two phases is influenced by gravity and consequently by the angle of the pipe. In horizontal pipes the gravity works orthogonal to the flow direction, whereas in vertical pipes the gravity works in or against the flow direction. In the following, the flow pattern for horizontal and vertical pipes are described.

For horizontal flow, the flow pattern map according to Taitel and Dukler [13] is recommended in literature [11, 12, 14]. That flow pattern map of Taitel and Dukler is based on an analytical theory, which predicts the transitions between the various flow regimes. The distribution of the two phases is determined by the balance of physical forces, mainly buoyancy forces, surface forces and pressure differences. Figure 5.2 shows the flow pattern map according to Taitel and Dukler. Four different dimensionless quantities are used to define the flow regime. On the x-axis the Lockart-Martinelli parameter X is plotted; the primary vertical y-axis indicates the parameter K_D and the secondary y-axis indicates the parameters T_D or respectively F_D. The parameter K_D describes the transition from stratified to wavy flow. It is dependent on the viscosity of the liquid phase because the waves are formed by shear stress between the vapour and the liquid phase. The parameter T_D describes the transition from slug to bubble flow. It considers the ratio between the frictional pressure drop of the liquid phase if the liquid phase is assumed to flow alone in the pipe and the buoyancy of the vapour phase. The parameter F_D describes the transition from wavy to slug or annular flow. It is dependent on the density ratio of both phases and the Froude number, which is defined as the ratio of the flow inertia force to gravity. To define the flow pattern the following procedure has to be complied with. The limiting curve between slug or wavy and annular flow is denoted as $A(X)$. If $F_\mathrm{D}(X) < A(X)$, draw K_D versus X. If $F_\mathrm{D}(X) \geq A(X)$ as well as $X \leq 2$ draw $F_\mathrm{D}(X)$ versus X, otherwise draw T_D versus X.

$$X = \left(\frac{\Delta p_\mathrm{l}}{\Delta p_\mathrm{v}} \right)^{0.5} \tag{5.2}$$

$$K_\mathrm{D} = \left(\frac{G^3 \cdot x^2 \cdot (1-x)}{(\rho_\mathrm{l} - \rho_\mathrm{v}) \cdot \rho_\mathrm{v} \cdot \mathrm{g} \cdot \mu_\mathrm{l}} \right)^{0.5} \tag{5.3}$$

$$T_\mathrm{D} = \left(\frac{\frac{\Delta p_\mathrm{l}}{\Delta L}}{(\rho_\mathrm{l} - \rho_\mathrm{v}) \cdot \mathrm{g}} \right)^{0.5} \tag{5.4}$$

$$F_{\mathrm{D}} = \frac{G \cdot x}{\left((\rho_{\mathrm{l}} - \rho_{\mathrm{v}}) \cdot \rho_{\mathrm{v}} \cdot \mathrm{g} \cdot d\right)^{0.5}} \tag{5.5}$$

Figure 5.1 illustrates the different flow regimes for horizontal flow, which can be described as follows.

- Bubble flow (1):
  The vapour phase forms small spherical bubbles within the liquid phase, which stay, due to bouncy forces, mainly in the upper part of the tube.

- Stratified flow (2):
  With increasing flow quality the two phases are almost separated completely into two layers. The liquid phase is located in the lower part of the tube, whereas the vapour phase is present in the upper part of the tube. No waves occur at the phase boundary.

- Wavy flow (3):
  If the total mass flow is increasing the shear stress at the phase boundary gets a noticeable influence. The conditions are comparable to those of stratified flow, but waves are created at the phase boundary because of the higher velocity of the vapour phase in comparison to the liquid phase.

- Slug flow (4):
  The liquid and the vapour phase are still more or less separated into two layers. However, waves are occasionally very large occupying the whole cross-section of the tube. In the surrounding of these large waves bubbles in the liquid phase as well as droplets in the vapour phase are entrained.

- Annular flow (5):
  At high flow qualities the urge of minimizing energy dissipation caused by friction becomes predominant and gravitational forces are overcome. The liquid flows in the outer part of the tube fully wetting the wall. Nonetheless, the liquid film is thicker at the bottom of the tube owing to gravity. Some droplets are dispersed in the vapour core.

- Mist flow:
  If the flow quality is further increasing the liquid is not able to maintain the film on the inner wall of the tube. The liquid forms small droplets and is dispersed in the vapour phase. One speaks of dry-out.

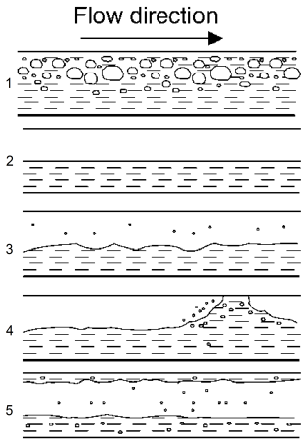

Fig. 5.1: Flow pattern for horizontal flow from [12].

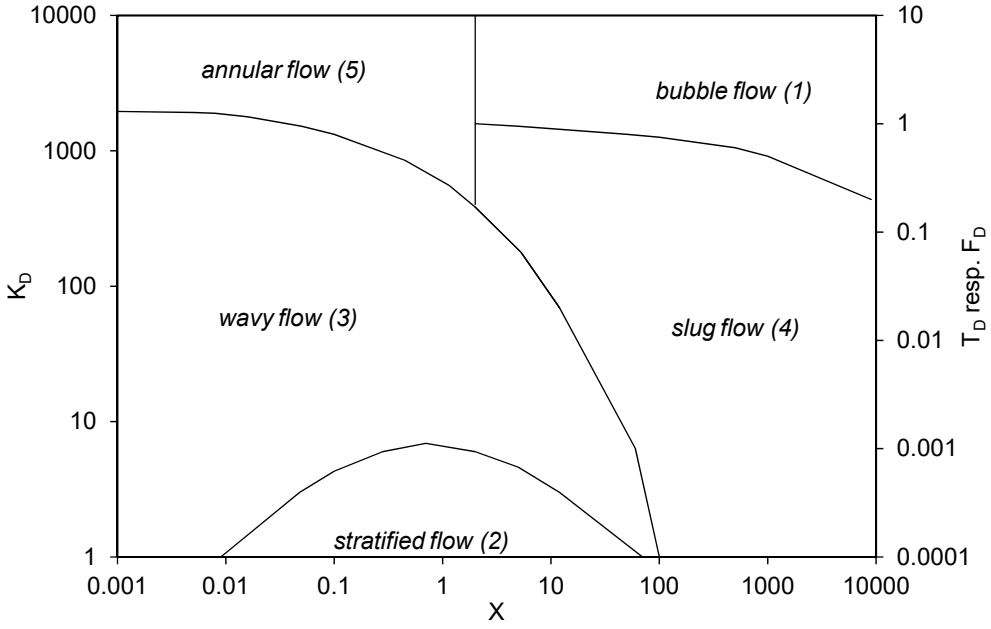

Fig. 5.2: Flow pattern map according to Taitel and Dukler for horizontal flow. The parameter K_D describes the transition from stratified to wavy flow. The parameter T_D describes the transition from slug to bubble flow. The parameter F_D describes the transition from wavy to slug or annular flow.

For vertical upward flow the flow pattern map according to Hewitt and Roberts [15] is recommended in literature [11, 12, 14]. That flow pattern map according to Hewitt and Roberts is, in contrast to the flow pattern map of Taitel and Dukler, derived from extensive experimental data. The flow pattern of different flows were visually observed by simultaneous x-ray and flash photography. Figure 5.4 shows the flow pattern map according to Hewitt and Roberts. The momentum flux of the liquid as well as the vapour phase are plotted on the horizontal and vertical axis, see equation (5.6) and equation (5.7). In the original map the quantities are expressed in Imperial units.

$$i_{\mathrm{l}} = \frac{(G \cdot (1 - x))^2}{\rho_{\mathrm{l}}} \tag{5.6}$$

$$i_{\mathrm{v}} = \frac{(G \cdot x)^2}{\rho_{\mathrm{v}}} \tag{5.7}$$

Figure 5.3 illustrates the different flow regimes for vertical upward flow, which can be described as follows:

- Bubble flow (1):
  The vapour phase forms small spherical bubbles within the liquid phase, which are homogeneously distributed throughout the cross section of the tube.

- Slug flow (2):
  With increasing flow quality the bubbles are growing due to the higher probability of coalescence. Slug flow is characterized by many bubbles, some of them are very large (several times the tube diameter in length). The shape of the large bubbles is like a bullet with a hemispherical nose and a blunt tail end. The tube wall is always wetted by liquid.

- Chaotic or churn flow (3):
  If the velocity is increasing the fluid starts oscillating up and down but the net flow stays upward. Instability results from the gravity and shear forces attacking the fluid from different directions. Bubbles at all sizes appear randomly across the whole cross section.

- Wispy annular flow (4):
  The liquid is predominantly present around the tube wall. The core of the tube contains the vapour phase with swarms of droplets.

- Annular flow (5):
  At very high gas flow rates the gravity is overcome. The liquid is homogeneously

distributed around the outer part of the tube and the vapour phase at the centre of the tube may contain some droplets.

- Mist flow:
  If the flow quality is further increased a dry-out similar to horizontal flow occurs.

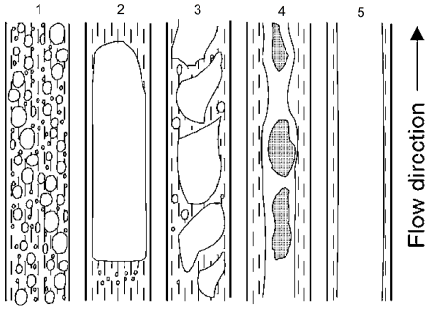

Fig. 5.3: Flow pattern for vertical upward flow from [12].

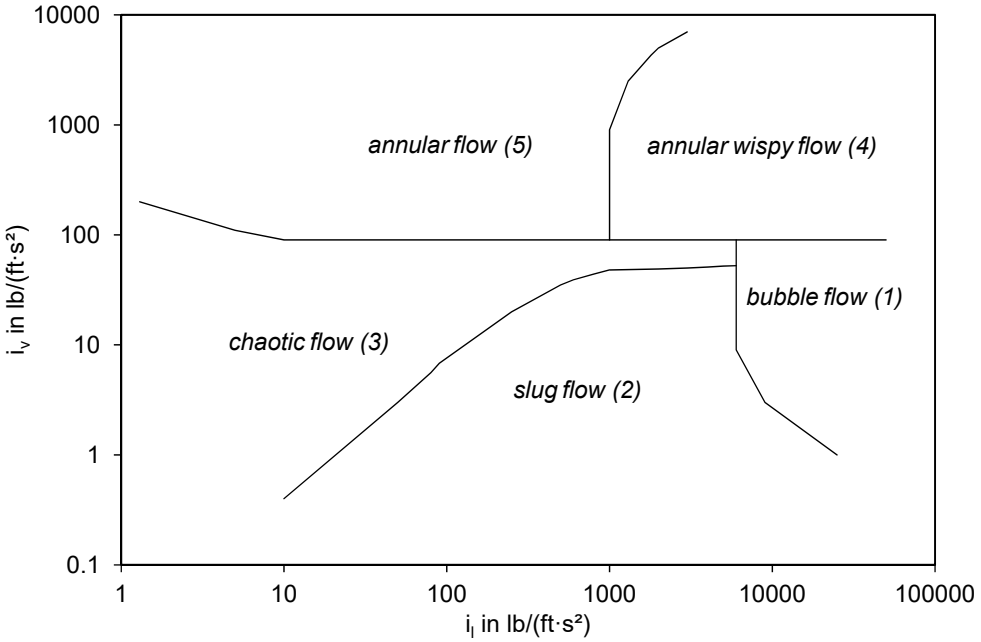

Fig. 5.4: Flow pattern map according to Hewitt and Roberts for vertical upward flow.

Recognized flow pattern maps for vertical downward flow doesn't exist in literature. According to [14] the flow patterns for vertical downward flow are similar to those for vertical upward flow.

It is important to note that all flow pattern maps mentioned above were developed for adiabatic flow conditions. However, there exist also flow pattern maps for diabatic conditions such as the flow pattern map according to Kattan or Wojtan. The implementation is much more complex and big differences to the adiabatic flow pattern maps are only visible at very high heat loads where the transition to mist flow and the prediction of the onset of dry-out is of interest [16].

5.1.3 Void fraction

Another important characteristic of two-phase flow is the void fraction ϵ. That property takes into account that the two-phase flow is not uniform, but discontinuously fluctuating. Consequently, the local void fraction ϵ^* at a specific location, see equation (5.8), shall vary with time. The function R equals one, if vapour is present and zero, if liquid is present. The variables x, y and z represent the three spatial dimensions. An average void fraction ϵ can be obtained by integrating the local void fraction ϵ^*, see equation (5.9). B represents a line, a surface or a volume.

$$\epsilon^*(x, y, z) = \frac{\int R(x, y, z)\, dt}{\int dt} \tag{5.8}$$

$$\epsilon = \frac{\int \epsilon^*(B)\, dB}{\int dB} \tag{5.9}$$

The local void fraction ϵ^* can be integrated over the volume of the tube leading to equation (5.10) by including the definition of the flow quality according to equation (5.1).

$$\epsilon_{\text{vol}} = \frac{\dot{V}_{\text{v}}}{\dot{V}_{\text{v}} + \dot{V}_{\text{l}}} = \frac{\frac{\dot{m}_{\text{v}}}{\rho_{\text{v}}}}{\frac{\dot{m}_{\text{v}}}{\rho_{\text{v}}} + \frac{\dot{m}_{\text{l}}}{\rho_{\text{l}}}} = \frac{\rho_{\text{l}} \cdot x}{\rho_{\text{l}} \cdot x + (1 - x) \cdot \rho_{\text{v}}} \tag{5.10}$$

Usually, the local void fraction is integrated over the cross-sectional area of the tube yielding to the equation (5.14). This equation is derived by coupling the equations of the velocity of the vapour phase, see equation (5.11), and the liquid phase, see equation (5.12), with the slip factor S defined as the velocity ratio of the vapour phase to the liquid phase, see equation (5.13). The velocities of both phases can be expressed with the respective mass flow through the part of the cross-sectional area that is occupied by the respective phase. The rearranged equation (5.14), see equation (5.15), shows that normally the cross-

sectional void fraction ϵ_{cs} is bigger than the flow quality x, as $\rho_l \rho_v^{-1} \gg 1$, and hence, $\rho_l \rho_v^{-1} S^{-1} > 1$. Only at the critical point, where the density difference of the liquid and vapour phase vanishes, the void fraction corresponds to the flow quality.

$$u_v = \frac{\dot{m}_v}{\rho_v \cdot A \cdot \epsilon_{cs}} = \frac{\dot{m} \cdot x}{\rho_v \cdot A \cdot \epsilon_{cs}} \tag{5.11}$$

$$u_l = \frac{\dot{m}_l}{\rho_l \cdot A \cdot (1 - \epsilon_{cs})} = \frac{\dot{m} \cdot (1 - x)}{\rho_l \cdot A \cdot (1 - \epsilon_{cs})} \tag{5.12}$$

$$S = \frac{u_v}{u_l} \tag{5.13}$$

$$\epsilon_{cs} = \frac{\rho_l \cdot x}{\rho_l \cdot x + (1 - x) \cdot \rho_v \cdot S} \tag{5.14}$$

$$\frac{1}{x} - 1 = \left(\frac{\rho_l}{\rho_v}\right) \cdot \frac{1}{S} \cdot \left(\frac{1}{\epsilon_{cs}} - 1\right) \tag{5.15}$$

The slip ratio S can be quantified by different correlations, over which Yu Xu et al. [17] gives a good overview. All these correlations are empirical and semi-empirical, as the underlying detailed mechanism are still field of research. Nevertheless, Levy [18] and later Fujie [19] as well as Huq and Loth [20] developed some analytical correlations of the void fraction.

1. Homogeneous correlation:
   The homogeneous correlation, not accounting for any interaction between the liquid and the vapour phase, assumes that both phases propagate at the same velocity and hence $S = 1$, compare equation (5.16). It is important to emphasize that the cross-sectional void fraction according to the homogeneous correlation corresponds to the volumetric void fraction in equation (5.10). It is only a function of the flow quality and the density of both phases $\epsilon_{cs,hom} = \epsilon_{vol} = f\left(x, \rho_v(p,T), \rho_l(p,T)\right)$. The homogeneous void fraction has a limited application range, favourable at conditions where the two phases move almost at the same velocity. That is the case for bubble or mist flow, where the dispersed phase has almost the same velocity as the continuous phase, and for high pressures near the critical pressure, where the density difference between the two phases vanishes.

   $$\epsilon_{hom} = \frac{\rho_l \cdot x}{\rho_l \cdot x + (1 - x) \cdot \rho_v} \tag{5.16}$$

2. Heterogeneous correlation:
   According to the heterogeneous correlation, accounting for the interaction between the liquid and the vapour phase, the velocities of both phases are not similar and, hence, $S \neq 1$. The cross-sectional void fraction according to the heterogeneous correlation and the volumetric void fraction do not conform but are connected by equation (5.17). If $S > 1$, then $\epsilon_{\mathrm{cs}} < \epsilon_{\mathrm{v}}$ applies, and if $S < 1$, then $\epsilon_{\mathrm{cs}} > \epsilon_{\mathrm{v}}$ applies. In the following the cross-sectional void fraction ϵ_{cs} is always used and referred to by just ϵ.

$$\epsilon_{\mathrm{vol}} = \frac{\epsilon_{\mathrm{cs}}}{\frac{1}{S} \cdot (1 - \epsilon_{\mathrm{cs}}) + \epsilon_{\mathrm{cs}}} \qquad \Longleftrightarrow \qquad \epsilon_{\mathrm{cs}} = \frac{\epsilon_{\mathrm{vol}}}{S \cdot (1 - \epsilon_{\mathrm{vol}}) + \epsilon_{\mathrm{vol}}} \tag{5.17}$$

   The heterogeneous correlations can again be divided as follows:

   a) $K \cdot \epsilon_{\mathrm{hom}}$ correlations:
      The simplest heterogeneous void fraction correlations are the $K \cdot \epsilon_{\mathrm{hom}}$ correlations. They are based on the homogeneous correlation multiplying the homogeneous void fraction with a factor K. Referring to [17], the correlation according to Crisholm and the correlation according to Massena are the two correlations of this category that predict best the reviewed literature data.

   b) Slip ratio correlations:
      The slip ratio correlations express the slip ratio as a function of the flow quality as well as fluid properties such as the density and the dynamic viscosity:

$$S = f\left(\left(\frac{1-x}{x}\right)^{p}\left(\frac{\rho_{\mathrm{v}}}{\rho_{\mathrm{l}}}\right)^{q}\left(\frac{\mu_{\mathrm{l}}}{\mu_{\mathrm{v}}}\right)^{r}\right) \quad . \tag{5.18}$$

      Referring to [17], the correlations according to Smith, Premoli et al. as well as Osmachkin and Borisov are the three correlations of this category that predict best the reviewed literature data.

   c) Drift-flux correlations:
      Drift flux correlations have the following form, see equation (5.19). The drift flux velocity u_{vj} accounts for local phase velocity differences and is defined as the velocity of the vapour with respect to the mixture. The parameter C_0 takes into account the effects of density and velocity distribution and is the ratio of the mean mixture volumetric flux to the area average volumetric flux. If $C_0 = 1$ the distribution is uniform, whereas if $C_0 \neq 1$ it is wide, more precisely, if $C_0 < 1$ the vapour concentration at the wall is greater, and if $C_0 > 1$, the vapour concentration in the core of the pipe is higher. The drift flux velocity u_{vj}

and the parameter C_0 are subject to certain boundary conditions. If the void fraction approaches zero and the liquid just starts boiling, the drift flux velocity u_{vj} and the parameter C_0 approaches zero assuming the bubbles be formed in the boundary layer at the wall with an initial velocity of zero; or the drift flux velocity u_{vj} and the parameter C_0 are within their range when assuming the bubbles be formed in the fluid due to flashing. If the void fraction approaches one and the flow becomes all vapour the drift flux velocity vanishes and C_0 becomes one. If the pressure approaches the critical pressure the flow becomes homogeneous and $u_{\mathrm{vj}} \to 0$ and $C_0 \to 1$, whereas if the pressure approaches zero $u_{\mathrm{vj}} \to \infty$. In compliance with the mass conservation one obtains the following equations for the velocity of the liquid, see equation (5.22), and vapour phase, see equation (5.21), enabling to calculate the slip ratio S [21, 22].

$$\epsilon = \frac{J_{\mathrm{v}}}{C_0 \cdot J + u_{\mathrm{vj}}} \quad \text{with} \tag{5.19}$$

$$J = J_{\mathrm{v}} + J_{\mathrm{l}} = \frac{x \cdot G}{\rho_{\mathrm{v}}} + \frac{(1-x) \cdot G}{\rho_{\mathrm{l}}} \tag{5.20}$$

$$u_{\mathrm{v}} = \frac{C_0 \cdot G + \rho_{\mathrm{l}} \cdot u_{\mathrm{vj}}}{C_0 \cdot \epsilon \cdot \rho_{\mathrm{v}} + (1 - C_0 \cdot \epsilon) \cdot \rho_{\mathrm{l}}} \tag{5.21}$$

$$u_{\mathrm{l}} = \frac{(1 - C_0 \cdot \epsilon) \cdot G - \epsilon \cdot \rho_{\mathrm{v}} \cdot u_{\mathrm{vj}}}{(1-\epsilon)\left[C_0 \cdot \epsilon \cdot \rho_{\mathrm{v}} + (1 - C_0 \cdot \epsilon) \cdot \rho_{\mathrm{l}}\right]} \tag{5.22}$$

Referring to [17], the correlation according to Rouhani or the correlation proposed by the authors themselves are the two correlations of this category that predict best the reviewed literature data. The original correlation according to Rouhani [23] is based on the correlation according to Zuber and Findlay [24], but many different modifications of the Rouhani correlation exist in literature. In this work the version of the Rouhani correlation as defined in [17] is used. Especially for horizontal flow the correlation according to Steiner, a modification of the Rouhani correlation, is also frequently recommended in literature [11, 12, 25]. The correlation according to Chexal-Lellouche [21, 22, 26] includes all inclinations of the pipe.

d) Miscellaneous correlations:
Miscellaneous other correlations can't be classified in one of the four categories mentioned above. Many of them are using the Lockart-Martinelli parameter X. Referring to [17], the correlation according to Yashar et al. and the correlation according to Huq and Loth are the two correlations of this category that predict best the reviewed literature data.

Heterogeneous correlations, by factoring in the interaction between the vapour and the liquid phase, reflect the dependency of the void fraction on the flow pattern, thus, the mass velocity and the flow direction. By referring to equation (5.14) the following general conclusion can be drawn. If the vapour phase flows faster than the liquid ($S > 1$), normally the case for vertical upward and horizontal flow, the homogeneous void fraction ϵ_{hom} is the upper threshold for the void fraction. If the velocity of the liquid phase exceeds the velocity of the vapour phase ($S < 1$), potentially the case for vertical downward flow due to gravity effects, the homogeneous void fraction is the lower threshold for the void fraction.

In the following the focus is on selected void fraction correlations: the homogeneous void fraction, the correlation according to Crisholm as $K \cdot \epsilon_{\text{hom}}$ correlation and the drift-flux correlations according to Rouhani, Steiner and Chexal-Lellouche. Figure 5.5 shows the void fraction according to these correlations versus the flow quality and figure 5.6 shows the dependency of the void fraction on the mass flow. Both figures are calculated for nitrogen two-phase flow at the saturation conditions of $p_{\text{sat}} = 1\,\text{bar}$ and $T_{\text{sat}} = 87\,\text{K}$. Figure 5.5 shows the dependency of the void fraction on the flow direction. In general, the void fraction increases with increasing flow quality. The slope is larger at low flow qualities. The void fraction correlation according to Rouhani as defined in [17] (referred to as Rouhani I) violates the boundary condition of $\epsilon = 1$ at $x = 1$ and, hence, fails to predict the void fraction at high flow qualities. The version of the Rouhani correlation according to [27] would solve this problem. Comparing Steiner and Rouhani, the void fraction of Steiner (horizontal flow) is over the whole range of the flow quality greater than the void fraction of Rouhani, preferable used for vertical upward flow. That corresponds to the description of the previous paragraph. On the contrary, according to Chexal-Lellouche, the void fraction for horizontal flow lies only above the void fraction for vertical upward flow for flow qualities smaller than 25 %. The correlation according to Chexal-Lellouche for vertical downward flow and the heterogeneous correlation predict the highest void fractions. Figure 5.6 reflects the fact, that the void fraction increases with increasing mass velocity [28]. Of course, the homogeneous correlation as well as the correlation according to Crisholm don't take this phenomena into account. However, the correlation according to Chexal and Lellouche predicts a moderate increase of the void fraction, whereas Rouhani and Steiner predict a sharper rise of the void fraction with growing mass velocity. Moreover, as most of these

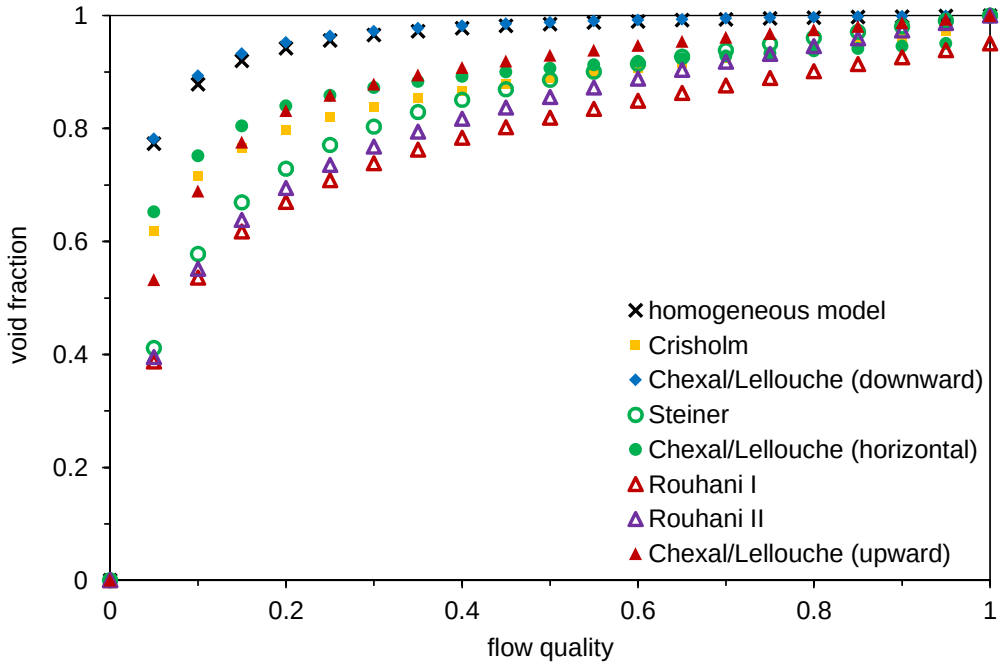

Fig. 5.5: Void fraction according to different correlations versus flow quality for a mass velocity of $25.5\,\mathrm{kg\,m^{-2}\,s^{-1}}$, calculated for nitrogen two-phase flow at saturation conditions $p_{\mathrm{sat}} = 1\,\mathrm{bar}$ and $T_{\mathrm{sat}} = 87\,\mathrm{K}$. Only the correlation according to Chexal-Lellouche distinguishes between different inclinations of the pipe. The correlation of Rouhani is often recommended in literature for vertical upward flow. The correlation of Steiner is often recommended in literature for horizontal flow. For the correlation of Crisholm the angle of the pipe is not specified.

void fraction correlations are derived from experiments conducted with water and steam, water and air or refrigerants like R134a, it cannot be concluded automatically that they are also applicable for nitrogen. One special feature of nitrogen is its low density ratio of the liquid to the vapour phase in comparison with customary refrigerants and particularly water ($\rho_{\mathrm{N_2,l}}\,\rho_{\mathrm{N_2,v}}^{-1} = 65$ at $p_{\mathrm{sat}} = 1\,\mathrm{bar}$ and $T_{\mathrm{sat}} = 87\,\mathrm{K}$). Thus, owing to the lack of correlations for nitrogen two-phase flow, the experimental small-scale measurement setup built up in the Cryolab enables an interesting study, which will contribute to extend the general knowledge of the refrigerant nitrogen used in several different applications, such as the ICARUS detector's thermal shield.

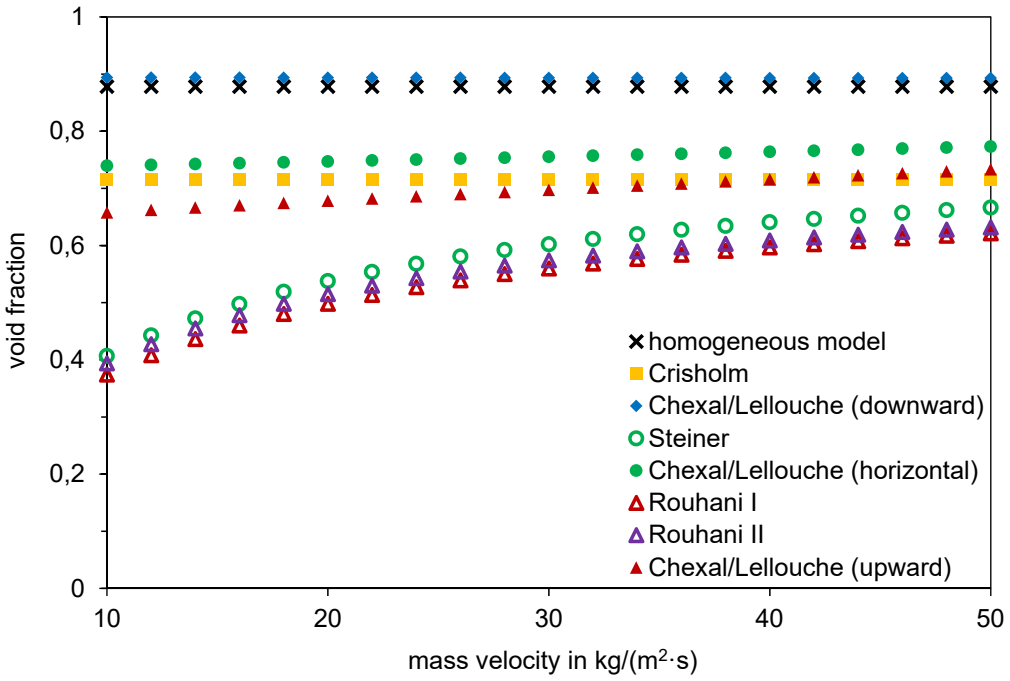

Fig. 5.6: Void fraction according to different correlations versus mass velocity for a flow quality of 10 %, calculated for nitrogen two-phase flow at saturation conditions $p_{\mathrm{sat}} = 1\,\mathrm{bar}$ and $T_{\mathrm{sat}} = 87\,\mathrm{K}$. Only the correlation according to Chexal-Lellouche distinguishes between different inclinations of the pipe. The correlation of Rouhani is often recommended in literature for vertical upward flow. The correlation of Steiner is often recommended in literature for horizontal flow. For the correlation of Crisholm the angle of the pipe is not specified.

5.2 Pressure drop in two-phase flow

The total pressure drop of two-phase flow along a pipe is the sum of the gravitational, frictional and momentum pressure drop:

$$\Delta p = \Delta p_{\mathrm{g}} + \Delta p_{\mathrm{f}} + \Delta p_{\mathrm{mom}} \quad . \tag{5.23}$$

5.2.1 Gravitational pressure drop in two-phase flow

The gravitational pressure drop is calculated, in analogy to single-phase flow, by the following equation:

$$\Delta p_{\mathrm{g}} = \rho_{\mathrm{2ph}} \cdot \mathrm{g} \cdot \sin(\varphi) \cdot L \quad . \tag{5.24}$$

The two-phase density $\rho_{2\text{ph}}$ is defined according to equation (5.25). If the homogeneous void fraction ϵ_{hom}, see equation (5.16), is used, the equation for the two-phase density simplifies to equation (5.26). As can be seen in figure 5.5, the void fraction according to various heterogeneous correlations is always smaller than the homogeneous void fraction, except for vertical downward flow. Consequently, the two-phase density calculated with the heterogeneous void fraction is higher than the homogeneous two-phase density, except for vertical downward flow, where it is the other way around.

$$\rho_{2\text{ph}} = (1 - \epsilon) \cdot \rho_{\text{l}} + \epsilon \cdot \rho_{\text{v}} \tag{5.25}$$

$$\rho_{2\text{ph,hom}} = \frac{\rho_{\text{l}} \cdot \rho_{\text{v}}}{\rho_{\text{l}} \cdot x + \rho_{\text{v}} \cdot (1 - x)} \tag{5.26}$$

The gravitational pressure drop only affects the total pressure drop if the pipe is not horizontal. In literature it is still discussed if for two-phase vertical downward flow the gravitational pressure drop results in a pressure gain, as well-known from single-phase flow, or if the pressure gain is negligible due to the buoyancy forces of the vapour [10].

5.2.2 Frictional pressure drop in two-phase flow

The frictional pressure drop accounts for the friction caused by wall roughness as well as interfacial roughness. It is calculated according to empirical or semi-empirical models, which are based on the well-known single-phase frictional pressure drop. The friction factor is normally independent of the wall roughness as the two-phase flow interaction effects prevail over the effects of the wall roughness [29].

$$\Delta p = f \cdot \frac{L}{d} \cdot 0.5 \cdot \rho \cdot u^2 = f \cdot \frac{L}{d} \cdot 0.5 \cdot \frac{G^2}{\rho} \quad \text{with} \tag{5.27}$$

$$f = f(Re), \quad Re = \frac{G \cdot d}{\mu} \tag{5.28}$$

The models can be categorised as follows [30]:

1. Homogeneous models:
   The two-phase frictional pressure drop is calculated by the universal equation (5.27) using the total mass velocity and two-phase properties averaged between the vapour and liquid properties. The models differ in determining the two-phase properties. According to [30], the models of Beattie-Whalley, McAdams et al. and Cicchitti et al. are the homogeneous models that predict best the reviewed literature data.

2. Separated flow models:
   Separated flow models obtain the two-phase frictional pressure drop by multiplying the single-phase frictional pressure drop (liquid or vapour phase) by a two-phase multiplier ϕ^2, see equation (5.29). Separated flow models allow, by defining different case-dependent two-phase multipliers, to consider that the two-phase frictional pressure drop is influenced by the flow pattern, hence varying with the flow direction and the flow regime. However, only some pressure drop models like [16, 25] are flow-pattern based. As proofed in literature and previous measurements of two-phase pressure drop of carbon dioxide at CERN demonstrated, the heat input has no or at high heat inputs of several $\mathrm{kW\,m^{-2}}$ only marginal impact on the frictional pressure drop [31, 32].

$$\left(\frac{\Delta p}{\Delta L}\right)_{\mathrm{2ph}} = \left(\frac{\Delta p}{\Delta L}\right)_{\mathrm{l}} \cdot \phi_{\mathrm{l}}^2 = \left(\frac{\Delta p}{\Delta L}\right)_{\mathrm{v}} \cdot \phi_{\mathrm{v}}^2 \tag{5.29}$$

   a) $\phi_{\mathrm{l}}^2, \phi_{\mathrm{v}}^2$ - method:
      The $\phi_{\mathrm{l}}^2, \phi_{\mathrm{v}}^2$ - method determines the single-phase pressure drop of the vapour and the liquid phase assuming that the respective flow propagates alone in the pipe. Well-known representative of this kind of model is the model according to Lockart and Martinelli. According to [30], only the model of Sun and Mishima predicts the reviewed literature data with a sufficient accuracy.

$$\left(\frac{\Delta p}{\Delta L}\right)_{\mathrm{l}} = f_{\mathrm{l}} \frac{(G(1-x))^2}{2 \cdot d \cdot \rho_{\mathrm{l}}}, \quad \left(\frac{\Delta p}{\Delta L}\right)_{\mathrm{v}} = f_{\mathrm{v}} \frac{(G \cdot x)^2}{2 \cdot d \cdot \rho_{\mathrm{v}}} \tag{5.30}$$

   b) $\phi_{\mathrm{l0}}^2, \phi_{\mathrm{v0}}^2$ - method:
      The $\phi_{\mathrm{l0}}^2, \phi_{\mathrm{v0}}^2$ - method determines the single-phase pressure drop of the vapour and the liquid phase assuming that the total flow is in the respective state. Well-known representatives of this kind of model are the models according to Friedel [33], Müller-Steinhagen and Heck [34], Gronnerud [35] and Crisholm. According to [30], the models of Souza and Pimenta and Cavallini also predict the reviewed literature data with a sufficient accuracy. Only the model of Müller-Steinhagen and Heck has been developed by pressure drop measurements of, amongst others, nitrogen.

$$\left(\frac{\Delta p}{\Delta L}\right)_{\mathrm{l}} = f_{\mathrm{l0}} \frac{G^2}{2 \cdot d \cdot \rho_{\mathrm{l}}}, \quad \left(\frac{\Delta p}{\Delta L}\right)_{\mathrm{v}} = f_{\mathrm{v0}} \frac{G^2}{2 \cdot d \cdot \rho_{\mathrm{v}}} \tag{5.31}$$

The frictional pressure drop plotted versus the flow quality shows a characteristic curve with a maximum of the pressure drop at a flow quality of approximately 80 % or slightly

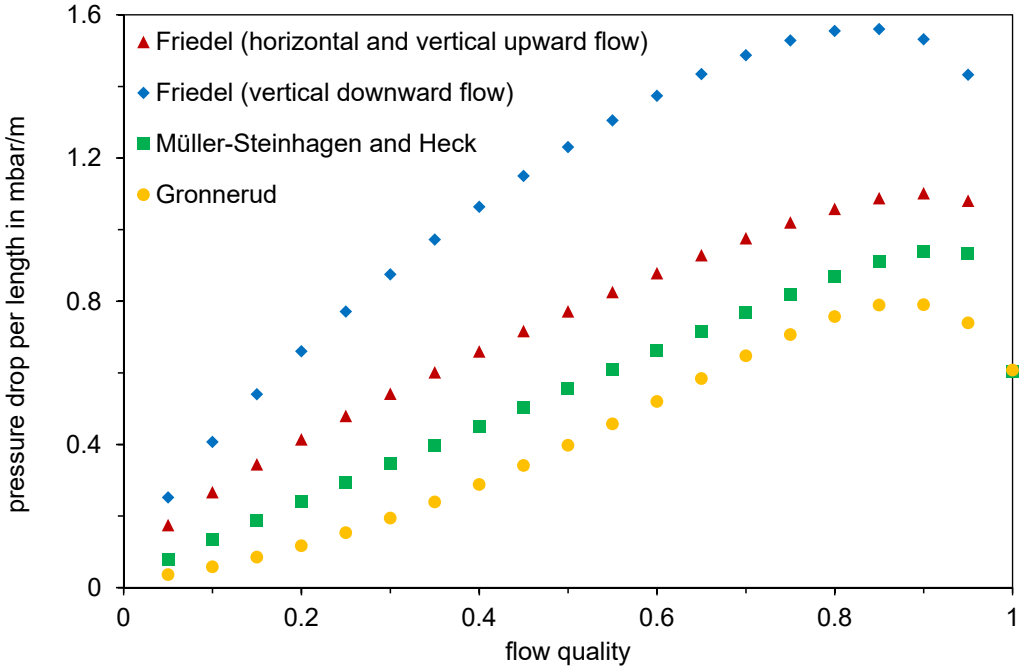

Fig. 5.7: Frictional pressure drop according to different models versus flow quality for a mass flow of $2\,\mathrm{g\,s^{-1}}$ in a pipe with an inner diameter of 10 mm , calculated for nitrogen two-phase flow at saturation conditions $p_{\mathrm{sat}} = 1\,\mathrm{bar}$ and $T_{\mathrm{sat}} = 87\,\mathrm{K}$. Only the model according to Friedel distinguishes between the inclination of the pipe.

above. After passing through the maximum the frictional pressure drop decreases to the frictional pressure drop of single-phase vapour flow. Figure 5.7 shows the course of the two-phase frictional pressure drop calculated by selected models according to Friedel, Müller-Steinhagen and Heck as well as Gronnerud versus the flow quality for the conditions in the ICARUS detector's thermal shield (nitrogen flow at saturation conditions of $p_{\mathrm{sat}} = 1\,\mathrm{bar}$ and $T_{\mathrm{sat}} = 87\,\mathrm{K}$). The model of Friedel proposes two different models, one for horizontal and vertical upward flow and the other for vertical downward flow. The frictional pressure drop in the latter case is higher as gravity and the buoyancy forces counteract. The frictional pressure drop model according to Friedel is the most conservative one at existing conditions.

5.2.3 Momentum pressure drop in two-phase flow

Unlike single-phase flow, the momentum pressure drop has to be factored in the total pressure drop for two-phase flow. It accounts for the pressure drop owing to the acceleration of molecules during the evaporation process, as molecules from the slower liquid phase enter the faster vapour phase.

$$\Delta p_{\mathrm{mom}} = G^2 \left\{ \left(\frac{(1-x)^2}{(1-\epsilon)\cdot\rho_{\mathrm{l}}} + \frac{x^2}{\epsilon\cdot\rho_{\mathrm{v}}} \right)_{out} - \left(\frac{(1-x)^2}{(1-\epsilon)\cdot\rho_{\mathrm{l}}} + \frac{x^2}{\epsilon\cdot\rho_{\mathrm{v}}} \right)_{in} \right\} \tag{5.32}$$

In general, the momentum pressure drop is higher at low flow qualities as the change of the void fraction at low flow qualities is more distinct. The absolute value of the momentum pressure drop can be several orders of magnitude smaller than the absolute value of the gravitational as well as frictional pressure drop. When the difference of the flow qualities at the inlet and outlet is large, particularly the case in non-adiabatic flow, or if the difference of the densities between the vapour and the liquid phase is huge, especially true at low system pressure, the momentum pressure drop can have a considerable contribution to the overall pressure drop.

6 Numeric model for nitrogen two-phase flow pressure drop

The numerical program described in this chapter calculates the two-phase pressure drop and has been developed for nitrogen two-phase flow at saturation conditions close to $p_{\mathrm{sat}} = 2.8\,\mathrm{bar}$ and $T_{\mathrm{sat}} = 87\,\mathrm{K}$. Different correlations for the void fraction as well as for the frictional pressure drop of two-phase flow can be integrated into the program by embedding different subfunctions into the main program. A measurement campaign is planned to validate the program and to allow to chose the void fraction and frictional pressure drop correlations from the literature, that describe best nitrogen two-phase flow at conditions similar to those of the ICARUS detector's thermal shield. Subsequently, if the program is able to reproduce the measurement data with a satisfying accuracy, the overall pressure drop over the real large-scale ICARUS thermal shield can be computed and the final design can be defined.

The mathematical description for the two-phase pressure drop has been implemented in Matlab®. The flow chart in the appendix B illustrates the simplified program structure. First of all, the user has to specify the following input parameters: pipe dimensions (inner diameter, length and orientation), the flow conditions (mass flow and heat flux), and the inlet conditions (saturation pressure and either enthalpy or flow quality). The exact fluid properties of nitrogen (saturation temperature and enthalpies, densities, viscosities of both phases as well as surface tension of liquid phase) at saturation pressures in the range of 2.6 bar to 2.9 bar are calculated with the embedded function "fluid properties". The function comprises the corresponding fit functions of NIST data. Knowing the fluid properties, the enthalpy or the flow quality (the quantity which has not been defined before by the user) can be calculated as well as the void fraction and the average density. The inlet conditions are referred to as "0" and the pressure drops at the pipe inlet are set to zero. The length of the pipe is discretizised in N 1 mm long parts. The outlet conditions of the previous part are the inlet conditions of the subsequent part, numerically realized by a for-loop. In each loop run the new outlet enthalpy of the part is determined according to the first law of thermodynamics, see equation (6.2). Equation (6.2) is derived from equation (6.1), which represents the one-dimensional energy equation for a steady-state

open system with one material flow. The program assumes a homogeneous distribution of the heat load over the length of the pipe, that means, each part has a heat load of $\dot{Q}/N$. Based on the outlet enthalpy other important characteristics of the flow (flow quality, void fraction, average density) can be computed, which are then used to finally determine the momentum, gravitational, frictional and total pressure drop over the part. An iterative computation is necessary as the outlet enthalpy is, among other variables, a function of the outlet fluid properties, which correspond to the a priori unknown outlet saturation pressure. Consequently, as a first step, the outlet fluid properties are approximated by the inlet values, and their real values and the exact pressure drop are then approached by an iteration, numerically realized by a do-while-loop. The do-while-loop is aborted if the difference of the outlet pressure calculated in the current loop run and the one calculated in the previous loop run is smaller than 10^{-7} bar. As mentioned above, different correlations for the void fraction and the frictional pressure drop can be included in the program. If the pipe has several sections with different orientations, the calculation has to be done sectionwise, with outlet values of the previous section being the inlet values of the subsequent section. In the following, the following naming convention is used: program refers to the Matlab® program, correlation refers to the void fraction correlation for two-phase flow and model refers to the frictional pressure drop model for two-phase flow.

$$\dot{Q} + \not{\mathcal{R}} = \dot{m} \left[\left(h + \frac{u^2}{2} + \mathrm{g}z \right)_{out} - \left(h + \frac{u^2}{2} + \mathrm{g}z \right)_{in} \right] \tag{6.1}$$

$$h_{\mathrm{out}} = h_{\mathrm{in}} + \frac{\dot{Q}}{\dot{m}} - 0.5 \cdot G^2 \left(\frac{1}{\rho_{\mathrm{out}}^2} - \frac{1}{\rho_{\mathrm{in}}^2} \right) - \mathrm{g} \cdot (z_{\mathrm{out}} - z_{\mathrm{in}}) \tag{6.2}$$

7 Small-scale setup for nitrogen two-phase flow pressure drop measurements

A small-scale experimental setup has been built in the Cryolab to measure the pressure drop of nitrogen two-phase flow at saturation conditions of $p_{\mathrm{sat}} = 2.8\,\mathrm{bar}$ and $T_{\mathrm{sat}} = 87\,\mathrm{K}$. The pressure drop has been determined in a quasi-adiabatic test section, comprising a horizontal, vertical upward and downward part, varying the mass flow and the flow quality.

7.1 Design and instrumentation of the experimental setup

Figure 7.1 shows the piping and instrumentation diagram (P&ID) of the small-scale experimental setup and figure 7.2 illustrates the ideal thermodynamic process (no pressure drop, no additional heat load) of the measurement in the p-h diagram. The setup has mostly been taken over from a previous one, which has been designed to perform a measurement campaign aiming to determine the temperature profile of the ICARUS detector's thermal shield in order to validate the ANSYS simulation shown in figure 4.5. The setup has been modified and substantially upgraded to measure the pressure drop in three different oriented pipe sections. Liquid nitrogen is supplied from a 500 l Dewar. The subsequent precooler filled with liquid nitrogen is operated at ambient pressure and allows to subcool the nitrogen flow. Theoretically, assuming an infinite heat transfer surface, the nitrogen flow could be cooled down to 78 K, the saturation temperature of nitrogen at ambient pressure. However, in practice, a finite heat transfer surface and heat load of the connection pipes and feedthroughs cease the nitrogen flow to a temperature between 82 K and 85 K depending on the total mass flow. Heater EH001 allows to adjust the initial point for the isenthalpic Joule-Thomson expansion, realized by a needle valve, so that the flow quality after the expansion into the two-phase area is around $1 - 2\,\%$. The two-phase area is entered by an expansion and not by heating in order to prevent instabilities of the system due to boiling delay effects. The thermodynamic equilibrium is assumed to be reached instantaneously. The heater EH003 after the test section fully evaporates the flow, so that the mass flow can be determined by a Venturi flowmeter at ambient temperature

conditions. The cartridge heater EH002 shall tune the flow quality for the real test section. A detailed drawing of the cartridge heater device can be found in the appendix A. It has been designed with an annular gap of 1 mm representing an optimum between pressure drop and heat transfer. The test section is made out of a copper tube with an inner diameter of 6 mm. Its geometry is depicted in figure 7.3. It consists of a horizontal part with a length of 3.2 m, a vertical upward part and a vertical downward part with a length of 1 m each. The horizontal part of the test section is approximated by a spiral due to limited space inside the cryostat. The curvature radius of the spiral is so large, that it should not affect the pressure drop of the nitrogen flow. To guarantee quasi-adiabatic conditions of the test section the following technically feasible solutions were implemented. Firstly, MLI (multi-layer insulation) is put around the sample. Secondly, a thermal shield, externally covered with MLI, is mounted around the sample. Thirdly, the lowest top plate of the insert is actively cooled by means of the sample outlet nitrogen flow and also cools the linked shield. All three above mentioned measures reduce the heat input by radiation into the test section. Finally, the whole cryostat is set to a vacuum pressure of 10^{-4} mbar before cool down to diminish heat transfer by convection. The special pressure tab device averages the pressure drop over the pipe cross-section by means of four evenly distributed holes, shown in the appendix A. At the beginning of the capillaries, connecting the pressure tab devices with the pressure sensors at the top of the cryostat, little heaters (H1-H6) are attached to ensure that there is no liquid column in the capillaries distorting the pressure drop measurements. The pressure in the test section is measured by pressure sensor PTN03 and regulated with outlet valve CVN02. The attenuation volume (AV) helps to stabilize the pressure inside the test section. The mass flow in the test section is measured by the Venturi flowmeter and is regulated with inlet valve CVN01. The pressure and mass flow control is further discussed in section 8.3.

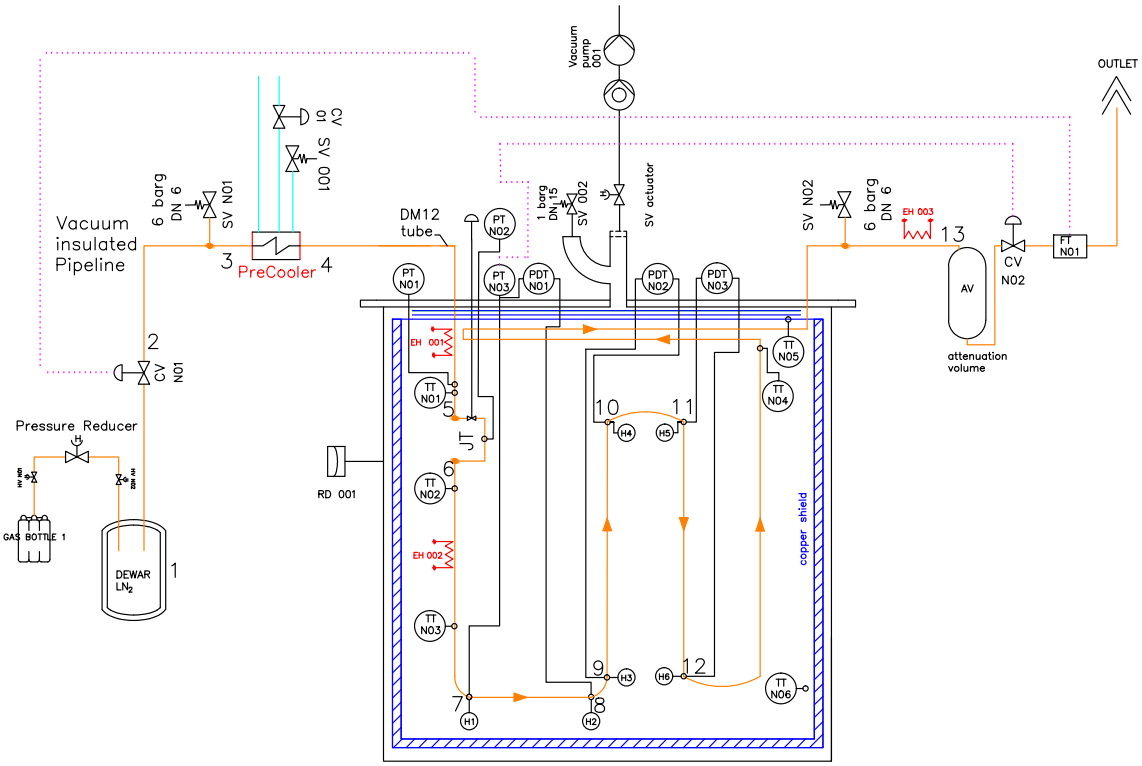

Fig. 7.1: P&ID of the experimental setup to measure the two-phase pressure drop of nitrogen. The actual quasi-adiabatic test section is inserted into the cryostat (outer shell) and comprises a horizontal part (7-8), a vertical upward part (9-10) and a vertical downward part (11-12).

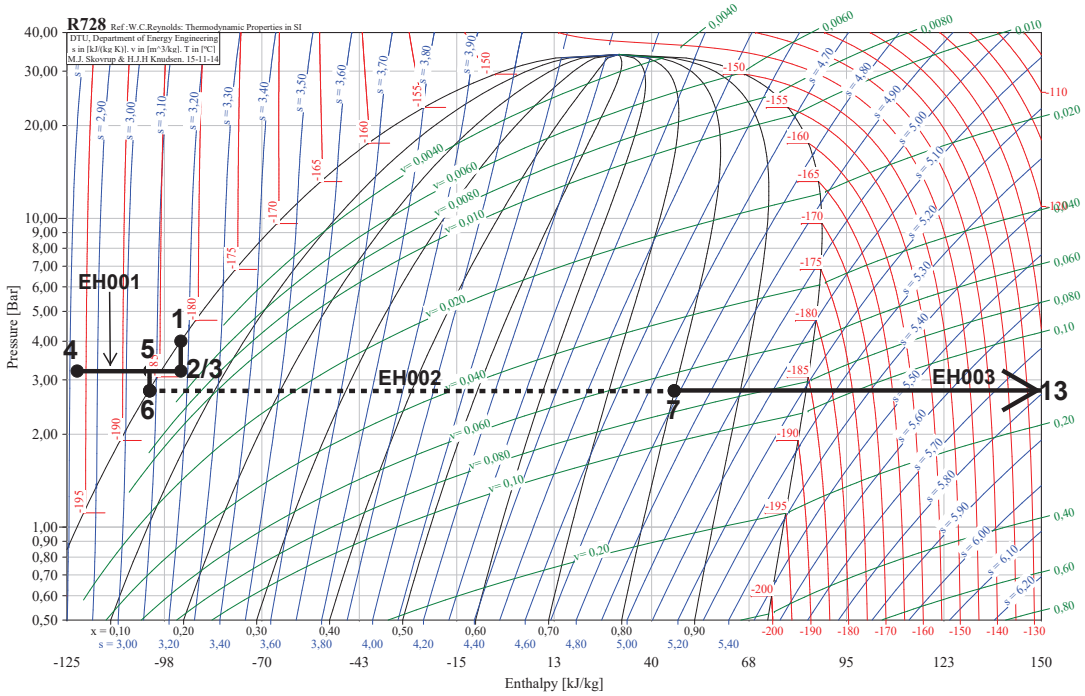

Fig. 7.2: Pressure-enthalpy diagram of nitrogen showing the ideal thermodynamic process (no pressure drop, no additional heat input) in the measurement setup. Heater EH002 allows to tune the conditions in the test section. The numbers correspond to the numbers used in the P&ID, see figure 7.1. Point 7 can be adjusted stepwise from point 6 to a flow quality of 80 %. The points 8-12 correspond with point 7.

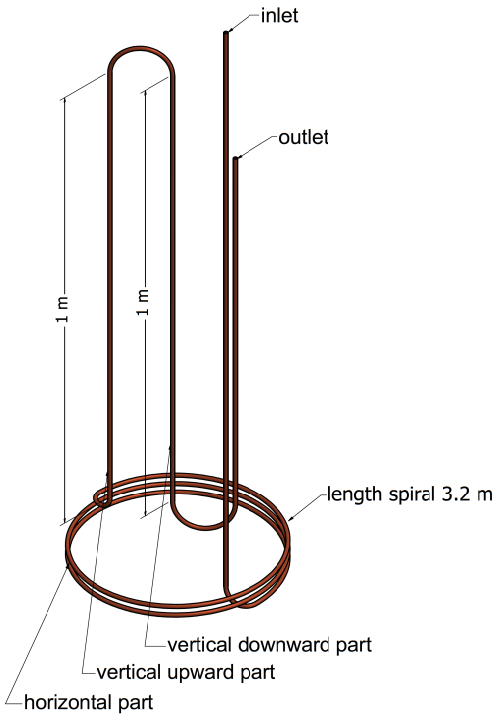

Fig. 7.3: Three-dimensional drawing of the copper test section consisting of a horizontal part (approximated by a spiral), a vertical upward part and a vertical downward part.

7.2 Uncertainty of the two-phase flow pressure drop measurements

The uncertainty of the measurement has been evaluated by the following method, which estimates the maximum error and specifies a range, in which the true value is allocated. It has to be noted that systematic errors are not included in this measurement uncertainty evaluation. Assuming that the value A is calculated from the values Z_1 to Z_n, which are directly measured, then the maximum error of the value A is determined by equation (7.1). The errors of the single values ΔZ_1 to ΔZ_n are obtained by the measuring instruments accuracy specified by the manufacturer plus the noise of the measurement signal, which is calculated by the standard deviation of the signal. As the signal noise is high compared to the reference accuracies, due to the instabilities in two-phase flow, and it is the only statistical error, the signal noise is added to the accuracies to determine the maximum error.

$$\Delta A = \sum_{1}^{n} \left| \frac{\partial A}{\partial Z_\mathrm{n}} \cdot \Delta Z_\mathrm{n} \right| \tag{7.1}$$

The following measuring instruments have been used.

- WIKA absolute pressure transmitter: *model S-10* [A]
- ROUSEMOUNT differential pressure transmitter: model 3051C [B]
- KEITHLEY DMM multimeter: *199 System DMM Scanner* [C]
- FLUKE PHILIPS system multimeter: *PM 2534* [D]
- NATIONAL INSTRUMENTS PXI: *NI PXI 8115* [E]

Table 7.1 gives an overview of the accuracies of the used measuring instruments according to the manufacturers. If data for the temperature effect, the pressure effect and the long-term stability exists, it is included in table 7.1. As all measuring instruments have been calibrated at known calibration points at the beginning of the measurement campaign, a time period of one year is assumed for the long-term stability. The temperature difference in the Cryolab is assumed to be a maximum of 5 K.

Tab. 7.1: Accuracy specifications of the used measuring instruments according to the manufacturers. The letters A to E refer to the individual measuring instruments as listed.

	reference accuracy	long-term stability
[A]	$\pm 0.25\,\%\ span$	$\pm 0.2\,\%\ span$ /1 year
[B]	$\pm 0.04\,\%\ span$	$\pm 0.2\,\%\ URL$ /10 years
[C]	$\pm \left(0.09\,\%\ reading + 2 \cdot 10^{-3}\right)$	
[D]	$\pm (0.20\,\%\ reading + 0.01\,\%\ range)$	
[E]	$\pm (12\,ppm\ reading + 0.5\,ppm\ range)$	

	temperature effect	pressure effect
[A]	$\pm 0.2\,\%\ span$ /10 K	
[B]	$\pm (0.025\,\%\ URL + 0.125\,\%\ span)$ /28 K	$\pm \left(\frac{0.05\,\%\ URL}{68.95\,\mathrm{bar}} + \frac{0.1\,\%\ reading}{68.95\,\mathrm{bar}}\right)$
[C]		
[D]		
[E]		

1. Error bars pressure drop:
   The pressure drop is directly measured by the Rousemount differential pressure transmitter. The signal of the differential pressure transmitter is read out by the PXI. With an upper range limit of 621.2 mbar and a span of 100 mbar for the differential pressure transmitter, and a range and maximum reading of 5 V for the PXI, the maximum error of the measured pressure drop is: $\Delta p = \pm (0.22\,\mathrm{mbar} + noise)$. In the following, the error bars for the pressure drop in y-direction are directly plotted in all diagrams.

2. Error bars flow quality:
   The flow quality is calculated by equation (7.2). The enthalpy h_0 is the enthalpy of the liquid nitrogen flow before the Joule-Thomson expansion. The voltage U and the current I quantify the powering of heater EH002, which adjusts the flow quality

inside the test section.

$$x = \frac{h - h_\mathrm{l}}{h_\mathrm{v} - h_\mathrm{l}} = \frac{h_0 + \frac{U \cdot I}{\dot{m}} - h_\mathrm{l}}{h_\mathrm{v} - h_\mathrm{l}} \tag{7.2}$$

According to equation (7.1) the maximum error of the flow quality is calculated as follows:

$$\begin{aligned}
\Delta x = & \\
& = \left|\frac{\partial x}{\partial h_0} \cdot \Delta h_0\right| + \left|\frac{\partial x}{\partial U} \cdot \Delta U\right| + \left|\frac{\partial x}{\partial I} \cdot \Delta I\right| + \\
& + \left|\frac{\partial x}{\partial \dot{m}} \cdot \Delta \dot{m}\right| + \left|\frac{\partial x}{\partial h_\mathrm{l}} \cdot \Delta h_\mathrm{l}\right| + \left|\frac{\partial x}{\partial h_\mathrm{v}} \cdot \Delta h_\mathrm{v}\right| = \\
& = \left|\frac{1}{h_\mathrm{v} - h_\mathrm{l}} \cdot \Delta h_0\right| + \left|\frac{I}{\dot{m} \cdot (h_\mathrm{v} - h_\mathrm{l})} \cdot \Delta U\right| + \\
& + \left|\frac{U}{\dot{m} \cdot (h_\mathrm{v} - h_\mathrm{l})} \cdot \Delta I\right| + \left|\frac{-I \cdot U}{\dot{m}^2 \cdot (h_\mathrm{v} - h_\mathrm{l})} \cdot \Delta \dot{m}\right| + \\
& + \left|\frac{h_0 + \frac{U \cdot I}{\dot{m}} - h_\mathrm{v}}{(h_\mathrm{v} - h_\mathrm{l})^2} \cdot \Delta h_\mathrm{l}\right| + \left|\frac{-h_0 - \frac{U \cdot I}{\dot{m}} + h_\mathrm{l}}{(h_\mathrm{v} - h_\mathrm{l})^2} \cdot \Delta h_\mathrm{v}\right| \quad .
\end{aligned} \tag{7.3}$$

- Error for the heater current:
  The current is measured by the Fluke Philips multimeter. With a range of 3 A and maximum reading of 1.9 A, the maximum error of the measured current is: $\Delta I = \pm 0.0041$ A.
- Error for the heater voltage:
  The voltage is measured by the Keithley multimeter. With a maximum reading of 120 V, the maximum error of the measured voltage is: $\Delta V = \pm 0.11$ V.
- Error for the enthalpy h_0:
  The enthalpy before the Joule-Thomson expansion is determined by the help of the NIST Database, using the measured values of the pressure PTN01 and the temperature TTN01.
  - Error for the pressure PTN01:
    The pressure PTN01 is measured by the WIKA absolute pressure transmitter and read out by the PXI. With a span of 6 bar and an average noise of

the signal during the measurement campaign of ± 0.02 bar, and a range and maximum reading of 5 V for the PXI, the maximum error of the measured pressure PTN01 is: $\Delta p(\text{PTN01}) = \pm 53$ mbar.

- Error for the temperature TTN01:
  The temperature TTN01 is measured by a Pt1000. The Pt1000 has been validated in nitrogen two-phase flow by measuring the saturation pressure with pressure sensor PTN01 and looking up the corresponding saturation temperature in the NIST Database. The error of the pressure sensor PTN01 in bar is translated into an error in Kelvin of ± 0.22 K by the help of the boiling point curve of nitrogen. The average noise of the temperature signal during the measurement campaign has been ± 0.25 K. The error of the PXI is already included in the validation. The maximum error of the measured temperature TTN01 is: $\Delta T(\text{TTN01}) = \pm 0.47$ K.

The error of the enthalpy h_0 is obtained by converting the error of the pressure PTN01 and the error of the temperature TTN01 into a difference in enthalpy by the help of the NIST Database. The maximum error of the enthalpy h_0 before the Joule-Thomson expansion yields: $\Delta h_0 = \pm 1\,\text{kJ}\,\text{kg}^{-1}$.

- Error for the enthalpy on boiling point curve h_l:
  The enthalpy h_l at the boiling point is determined by the help of the NIST Database, using the measured value of the pressure PTN03.
  - Error for pressure PTN03:
    The pressure PTN03 is measured by the WIKA absolute pressure transmitter and read out by the PXI. With a span of 6 bar and an average noise of the signal during the measurement campaign of ± 0.02 bar, and a range and maximum reading of 5 V for the PXI, the maximum error of the measured pressure PTN03 is: $\Delta p(\text{PTN03}) = \pm 53$ mbar.

  The error of the enthalpy h_0 is obtained by converting the error of the pressure PTN03 into a difference in liquid saturation enthalpy by the help of the NIST Database. The maximum error of the enthalpy at the boiling point h_l is: $\Delta h_\text{l} = \pm 0.44\,\text{kJ}\,\text{kg}^{-1}$.

- Error for the enthalpy at the dewing point curve h_v:
  The enthalpy h_v is determined analogically to the enthalpy h_l by the help of the signal of pressure PTN03 and the NIST Database. The maximum error of the enthalpy on the dewing point h_v is: $\Delta h_\text{v} = \pm 0.11\,\text{kJ}\,\text{kg}^{-1}$.

- Error for the mass flow:
  The mass flow is determined by the pressure drop over an orifice.
  - Error for the differential pressure (for mass flow):
    The pressure drop is measured by the Rousemount differential pressure transmitter. With an upper range limit of 621.2 mbar and a span of 60 mbar for the differential pressure transmitter, the maximum error of the measured pressure drop is: $\Delta p(\dot{m}) = \pm 0.19\,\mathrm{mbar}$.

  The error of the mass flow is obtained by converting the error of the pressure drop into a difference in mass flow by the help of a calibration curve. With an average noise of the signal during the measurement campaign of $\pm 0.07\,\mathrm{g\,s^{-1}}$, and a range and maximum reading of 5 V for the PXI, the maximum error of the measured mass flow is: $\Delta\dot{m} = \pm 0.09\,\mathrm{g\,s^{-1}}$.

The total maximum error of the flow quality depends on the absolute mass flow and the power of heater EH002, that means the measured voltage and current. Table 7.2 summarizes four different cases: high and low mass flow and high and low heat input, respectively high and low flow quality. In the following, the error bars for the flow quality in x-direction are omitted in all diagrams because of clarity reasons.

Tab. 7.2: Maximum error of the flow quality at four different measurement points: low and high mass flow and low and high flow quality.

$\dot{m}$ in $\frac{\mathrm{g}}{\mathrm{s}}$	$x = 0.05$	$x = 0.6$
0.7	± 0.012	± 0.086
2.0	± 0.0095	± 0.035

7.3 Results and discussion of the nitrogen two-phase flow pressure drop measurements

The pressure drop of nitrogen two-phase flow has been measured in horizontal, vertical upward and vertical downward flow orientation. The measurements have been conducted under quasi-adiabatic conditions and the saturation pressure (PTN03) in the test section has been regulated at 2.8 bar, corresponding to a saturation temperature of 87 K. The nitrogen two-phase flow pressure drop has been determined at different flow qualities and different mass flows. It has been scanned through the two-phase area from flow qualities close to zero up to flow qualities of 50 % to 80 %. The reachable value of the flow quality

has been limited at high mass flows by the 120 V power supply of the heater EH002 and at low mass flows by the beginning of dry-out, observable by a sharp increase of temperature TTN04 at the end of the cryostat insert. Measurements at nine different mass flows have been performed. For the evaluation the mass flow is converted into the mass velocity by the help of the pipe's cross-section to obtain a quantity that is independent of the design of the measurement setup, see table 7.3. The small increase of the flow quality inside the test section, even under adiabatic conditions, owing to the pressure drop over the test section length, is taken into account. The measured pressure drops of each part are always plotted versus the average flow quality of the part. However, the changes of the flow quality are only visible in the third or fourth digit after the decimal point.

Tab. 7.3: Mass flow and mass velocity values of the nine measurements. The pipe of the test section has an inner diameter of 6 mm.

number measurement	1	2	3	4	5	6	7	8	9
mass flow in $\mathrm{g\,s^{-1}}$	2.02	1.94	1.69	1.58	1.09	1.00	0.99	0.86	0.64
mass velocity in $\mathrm{kg\,m^{-2}\,s^{-1}}$	71.44	68.61	59.77	55.88	38.55	35.37	35.01	30.42	22.64

Before discussing the measurement results in detail and separately by the flow direction, it is shown, where the measurement conditions are located in the flow pattern map, that means, which flow regimes occur during the measurements. For the flow in the horizontal part of the test section the flow pattern map according to Taitel and Dukler, as described in section 5.1.2, is used. In figure 7.4 the locations of the nitrogen two-phase flow at four selected mass velocities within the range of the measured mass velocities and at flow qualities in 5 % steps from 5 % to 80 % are displayed. The measurement conditions cover three different flow pattern depending on the mass velocity and the flow quality: stratified flow, wavy flow and annular flow. At a low mass velocity of about $21\,\mathrm{kg\,m^{-2}\,s^{-1}}$ the flow goes over from stratified to wavy flow with increasing flow quality, but the annular flow regime is never reached. At higher mass velocities a transition from stratified to wavy and finally to annular flow occurs with increasing flow quality. The higher the mass flow, the earlier, that means at lower flow qualities, the transition takes place. At high mass velocities of about $71\,\mathrm{kg\,m^{-2}\,s^{-1}}$ the flow is directly located in the wavy flow regime, even at low flow qualities. For vertical upward and vertical downward flow the flow pattern map of Hewitt and Roberts, as described in section 5.1.2, is used. Figure 7.5 shows the corresponding flow pattern map, displaying the flow regime of the nitrogen flow at the conditions mentioned above. As it can be seen, the flow in the vertical upward and downward part of the test

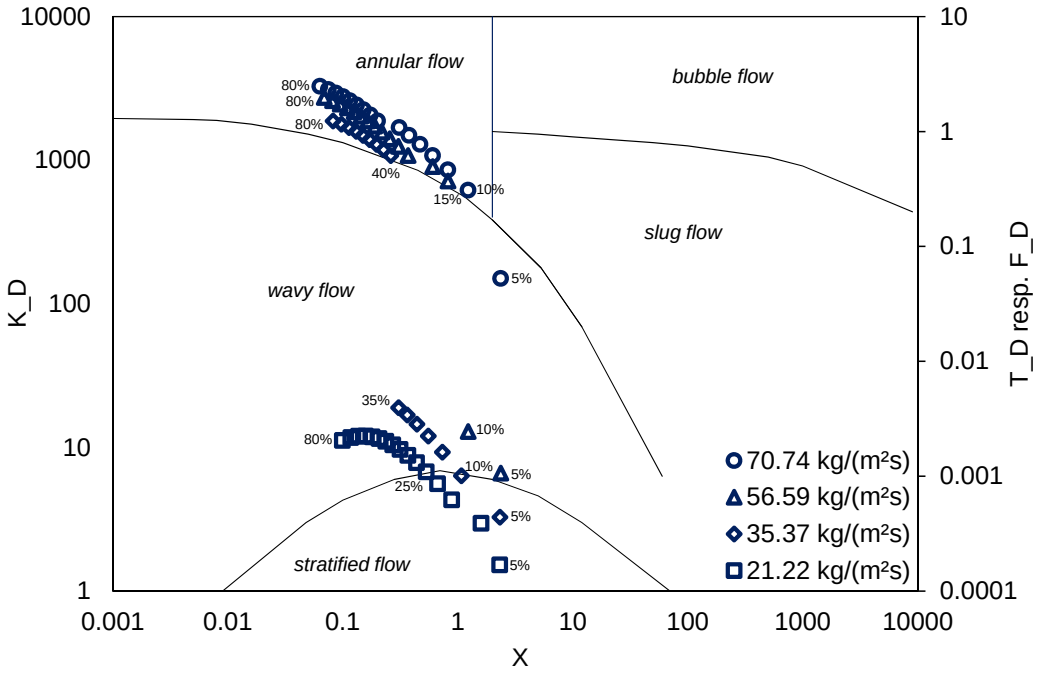

Fig. 7.4: Flow pattern map according to Taitel and Dukler for horizontal flow as explained in section 5.1.2. Indicated is the flow regime of nitrogen two-phase flow calculated at four different mass velocities and flow qualities in 5 % steps from 5 % to 80 %. The transition from wavy to annular flow occurs so fast, that a 5 % increase of the flow quality results in a jump form wavy to annular flow.

section has lower momentum flow densities of the vapour and the liquid phase as the flow pattern map was originally developed for, but by extrapolating the boundaries between the different flow regimes, it can be stated, that the flow is probably located in the chaotic flow regime. The annular flow regime is never entered in the vertical parts of the test section for nitrogen flow at the measurement conditions. In contrast to horizontal flow, vertical flow is stronger influenced by gravity. Thus, the interfacial shear, that means the velocity difference between the vapour and the liquid phase, has to be higher than in horizontal flow to dominate over gravity and to form the annular flow pattern.

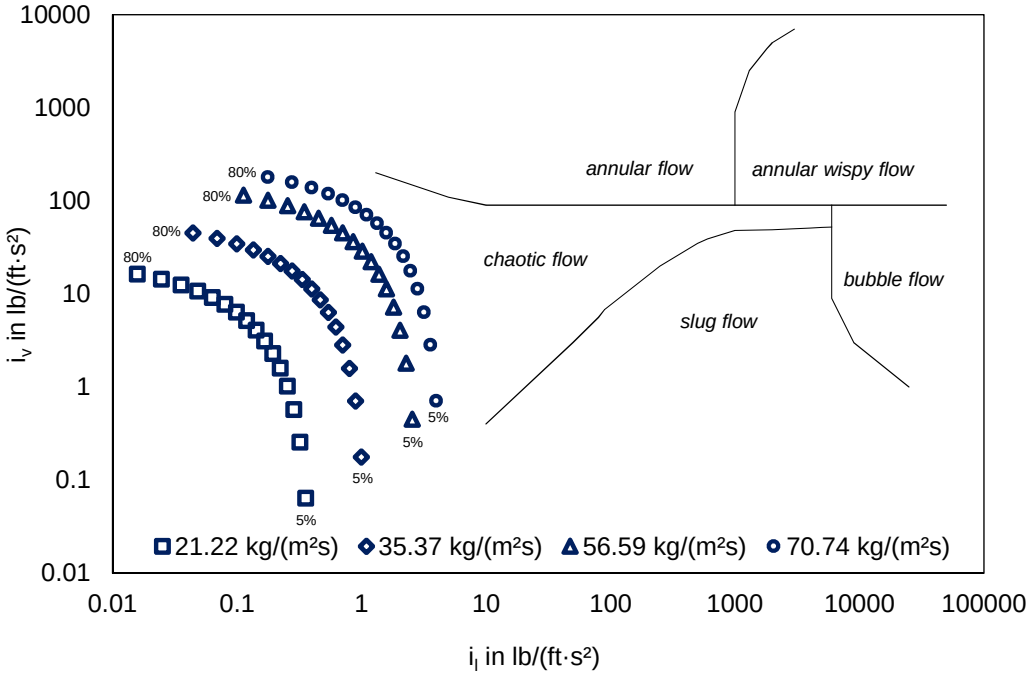

Fig. 7.5: Flow pattern map according to Hewitt and Roberts for vertical flow as explained in section 5.1.2. Indicated is the flow regime of nitrogen two-phase flow calculated at four different mass velocities and flow qualities in 5 % steps from 5 % to 80 %.

7.3.1 Results and discussion of the horizontal flow measurements

Figure 7.6 shows the pressure drop measured in the 3.2 m long horizontal part of the test section versus the flow quality for nine different mass velocities. In horizontal flow conditions the frictional pressure drop causes the main contribution to the total pressure drop. For flow qualities higher than about 20 %, the pressure drop is positively correlated with the flow quality owing to the increased interaction between the liquid and the vapour phase. At low mass velocities, the pressure drop increases only slightly with the flow quality, but the higher the mass velocity the steeper the pressure drop rises. At flow qualities lower than 20 %, it seems, despite the noise of the pressure drop signal, that the pressure drop is constant or decreases slightly with increasing flow quality. Moreover, the pressure drop rises with faster mass velocity. The difference between the pressure drop at different mass velocities becomes more distinct at higher flow qualities and higher mass velocities. The latter effect resembles the quadratic dependence of the frictional pressure drop on the mass

velocity known from single-phase flow. The behaviour of the pressure drop at horizontal flow could be explained by flow regime transitions. Only if the flow is in the stable annular flow regime, the pressure drop increases significantly with the flow quality. As can be seen in figure 7.4, the nitrogen two-phase at, for example, a mass velocity of $35\,\mathrm{kg\,m^{-2}\,s^{-1}}$ reaches the annular flow regime for flow qualities higher than 40 %. That corresponds well with the clear increase of the pressure drop in figure 7.6. If the mass velocity is higher, the annular flow regime is entered at a lower flow quality and the pressure drop curve rises earlier.

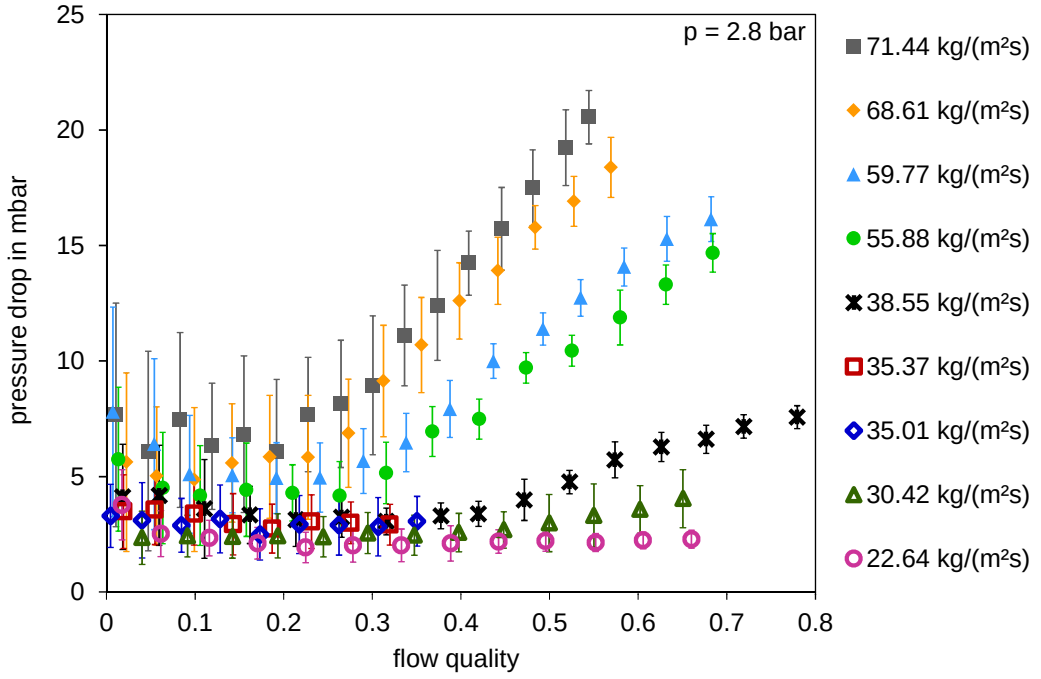

Fig. 7.6: Measured nitrogen two-phase pressure drop in the 3.2 m long **horizontal** part of the test section versus the flow quality for nine different mass velocities. Measurement conditions: adiabatic, $p = 2.8$ bar. For the flow quality errors in x-direction please refer to table 7.2.

As in horizontal flow, the frictional pressure drop contributes most to the total pressure drop, the measurement data from the horizontal part of the test section are used to determine the best existing model from literature for the two-phase frictional pressure drop of nitrogen flow at the conditions of the ICARUS thermal shield. The measurement data have been compared to the results of the program, presented in chapter 6, applying ten different frictional pressure drop models. The applied models are the following: Müller-Steinhagen

and Heck, Sun-Mishima, Beattie-Whalley, McAdams et al., Souza-Pimenta, Cicchitti et al., Friedel, Gronnerud, Cavallini et al. out of [30] as well as Bandel proposed in [36]. For the void fraction the correlation according to Rouhani I from [17] has always been used. The calculated results are only presented for the models best fitting the measured data. These models are Müller-Steinhagen and Heck, see figure 7.7, Gronnerud, see figure 7.8, and Friedel, see figure 7.9. The program gives the best overall result when using the frictional pressure drop model according to Müller-Steinhagen and Heck. That model is also recommend for argon and nitrogen flow by the authors themselves in [36].

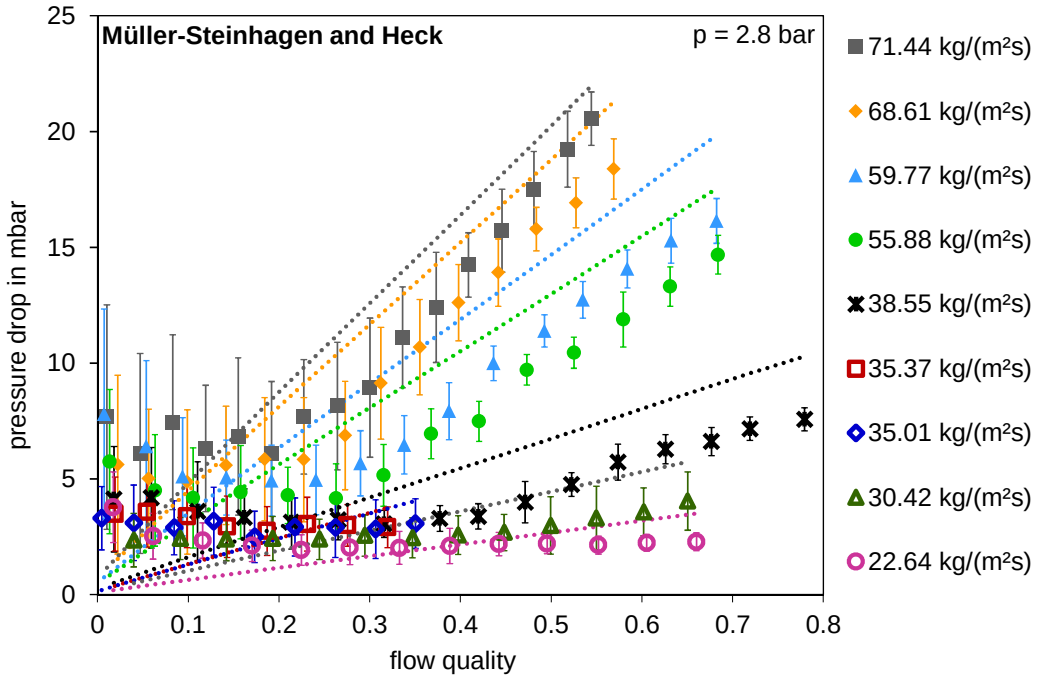

Fig. 7.7: Comparison of the measurement data (markers) for the pressure drop in the **horizontal** part with the calculated pressure drop (dotted lines). Applied frictional pressure drop model: Müller-Steinhagen and Heck. For the flow quality errors in x-direction please refer to table 7.2.

With the model of Gronnerud, the calculated results reproduce better the shape of the pressure drop course versus the flow quality, but the pressure drop at low mass velocities is underpredicted. For the planned scale-up to the thermal shield of the ICARUS detector an overprediction of the pressure drop is preferred to be on the safe side.

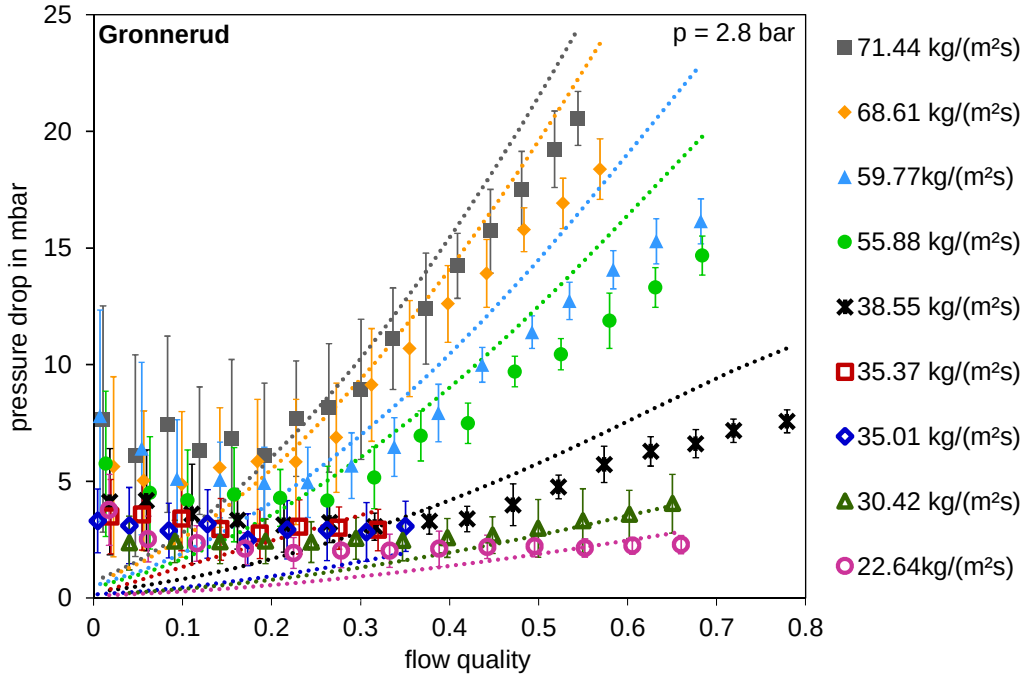

Fig. 7.8: Comparison of the measurement data (markers) for the pressure drop in the **horizontal** part with the calculated pressure drop (dotted lines). Applied frictional pressure drop model: Gronnerud. For the flow quality errors in x-direction please refer to table 7.2.

If the model according to Friedel is applied, the pressure drop at low flow qualities is predicted better, but throughout the whole range of flow qualities the pressure drop is far overpredicted. The program is never able to calculate the minimum of the pressure drop at about 20 %, whatever frictional pressure drop model is used. It is remarkable, that all above mentioned homogeneous frictional pressure drop models (Mc. Adams et al., Cicchitti et al. and Beattie and Whalley) largely underestimate the measured pressure drop, what is not depicted here.

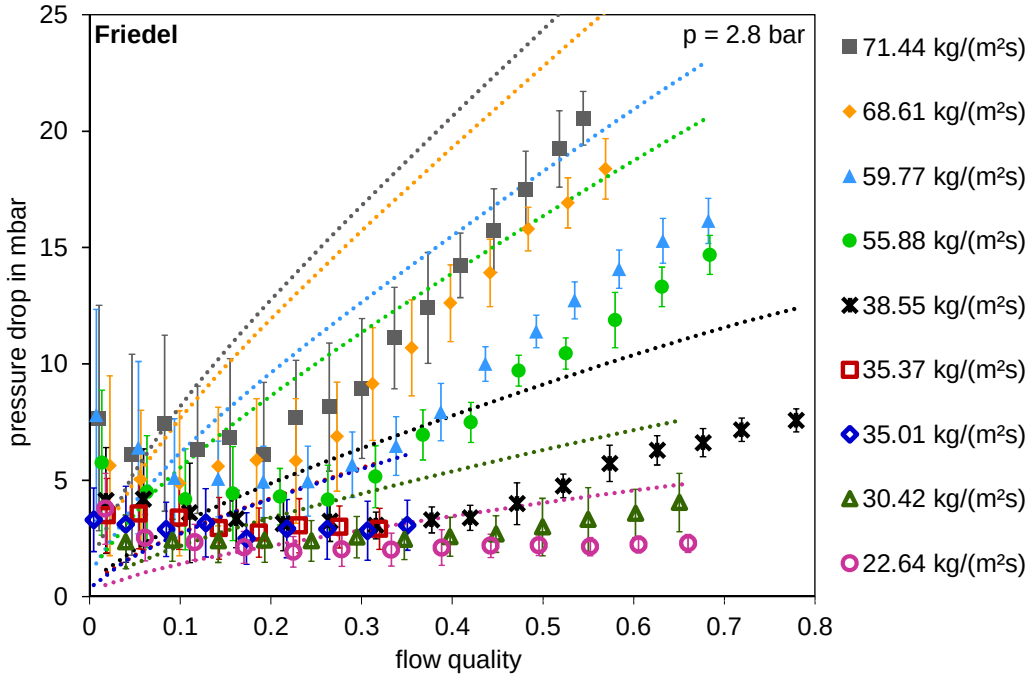

Fig. 7.9: Comparison of the measurement data (markers) for the pressure drop in the **horizontal** part with the calculated pressure drop (dotted lines). Applied frictional pressure drop model: Friedel. For the flow quality errors in x-direction please refer to table 7.2.

7.3.2 Results and discussion of the vertical upward flow measurements

Figure 7.10 shows the pressure drop measured in the 1 m long vertical upward part of the test section versus the flow quality for nine different mass velocities. In vertical upward flow orientation the gravitational pressure causes the main contribution to the total pressure drop. The gravitational pressure drop reduces with increasing flow quality, as the average density is reduced with increasing flow quality. The pressure drop decreases steeply up to flow qualities of about 10 %, then it declines more moderately, as the change of the void fraction with the flow quality is more distinct at low flow qualities, see figure 5.5. The influence of the mass velocity on the pressure drop is not so pronounced as in the case of horizontal flow, the pressure drop differences between the different mass velocities are small. Up to flow qualities of about 30 % the differences between the mass velocities are marginal by also taking into account the error of the measurement signal. For flow qualities greater than 30 % a trend of higher pressure drop for lower mass velocities is visible.

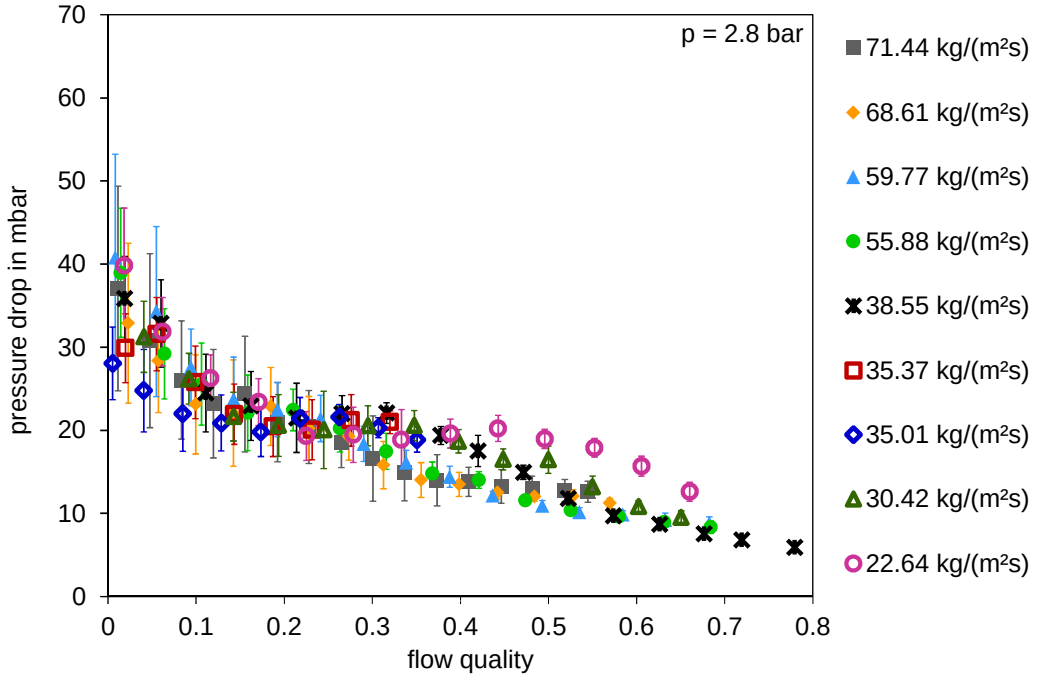

Fig. 7.10: Measured nitrogen two-phase pressure drop in the 1 m long **vertical upward** part of the test section versus the flow quality for nine different mass velocities. Measurement conditions: adiabatic, $p = 2.8$ bar. For the flow quality errors in x-direction please refer to table 7.2.

As in vertical upward flow, the gravitational pressure drop contributes most to the total pressure drop, the best existing correlation from literature for the two-phase void fraction at the conditions of the ICARUS thermal shield has been evaluated with the measurement data from the vertical upward part. The measurement data have been compared to the results of the program, presented in chapter 6, applying eleven different void fraction correlations. The correlations are the following: Crisholm, Yashar et al, Smith, Massena, Hug-Loth, Steiner, Premoli et al., Osmachkin-Borisov and the Rouhani I out of [17] and the correlation proposed by the authors themselves. Additionally, the version of the Rouhani I correlation according to [27] and the correlation according to Chexal-Lellouche has been used. For the frictional pressure drop the model according to Müller-Steinhagen and Heck, as chosen in section 7.3.1, has been used. The calculated results are only presented for the correlations best fitting the measured data. The program gives the best overall result when using the void fraction correlation according to Rouhani I, see figure 7.11. However, the

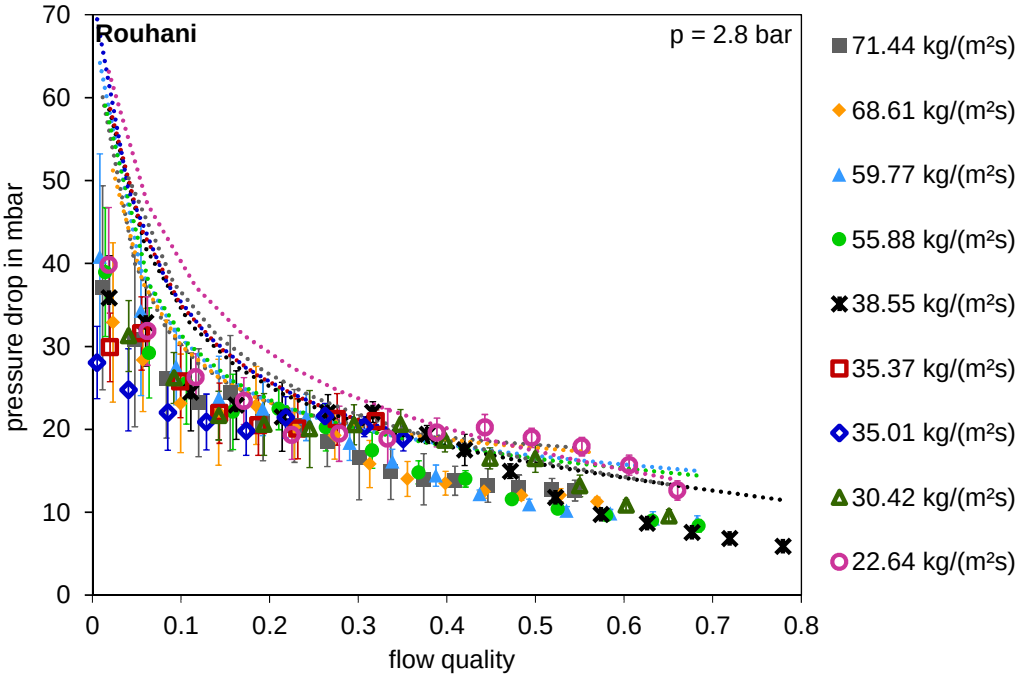

Fig. 7.11: Comparison of the measurement data (markers) for the pressure drop in the **vertical upward** part with the calculated pressure drop (dotted lines). Applied void fraction correlation: Rouhani. For the flow quality errors in x-direction please refer to table 7.2.

Rouhani I correlation predicts for low flow qualities high pressure drop values, including a steep decrease of the pressure drop at flow qualities from 0 % to 20 %. It overpredicts the pressure drop at low flow qualities compared to the measured data. For the planned scale-up to the thermal shield of the ICARUS detector, the focus is on the accurate prediction of the pressure drop at flow qualities higher than 10 %. The pressure drop at low flow qualities up to 10 % to 15 % is better reproduced by the Crisholm correlation, but which underpredicts the pressure drop for all higher flow qualities, see figure 7.12. Interestingly, all void fraction correlations taking into account a dependency of the void fraction on the mass velocity, tend to overpredict the pressure drop, especially at low flow qualities up to 10 %. On the contrary, all void fraction correlations neglecting a dependency of the void fraction on the mass velocity, succeed to predict the pressure drop for the measurement data at low flow qualities up to 10 % better, but strongly underestimate the pressure drop at higher flow qualities.

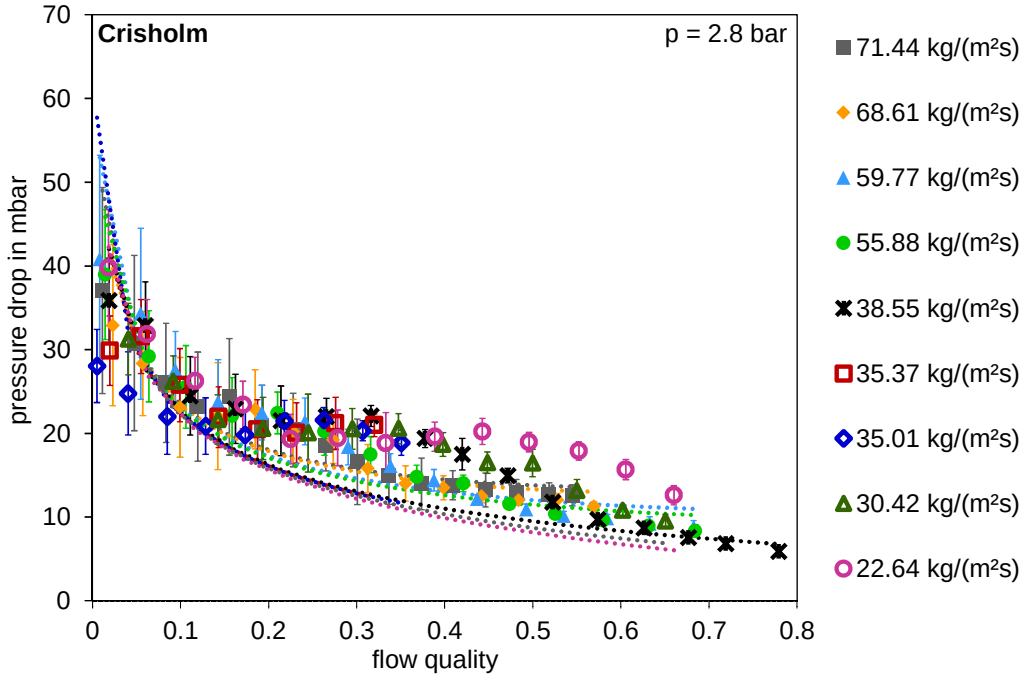

Fig. 7.12: Comparison of the measurement data (markers) for the pressure drop in the **vertical upward** part with the calculated pressure drop (dotted lines). Applied void fraction correlation: Crisholm. For the flow quality errors in x-direction please refer to table 7.2.

7.3.3 Results and discussion of the vertical downward flow measurements

Figure 7.13 shows the pressure drop measured in the 1 m long vertical downward part of the test section versus the flow quality for nine different mass velocities. In vertical downward flow the gravitational pressure drop should be, in theory, the main contributor to the total pressure drop, resulting in a pressure gain for downward flow. However, as can be seen in figure 7.13, the pressure drop for all mass velocities and over the whole range of flow qualities is close to zero. Only at low flow qualities smaller than 10 %, despite the noise of the signal, the measurement data suggest a small pressure gain. This observation confirms the statement of [10], who claims that the gravitational pressure drop must not be included into the total pressure drop for vertical downward flow. It seems that the effect of a pressure gain during vertical downward flow, as it is quite known from single-phase liquid flow, is eliminated when only a few bubbles are formed granted that buoyancy forces counteract the gravitational forces. At higher flow qualities as well as higher mass

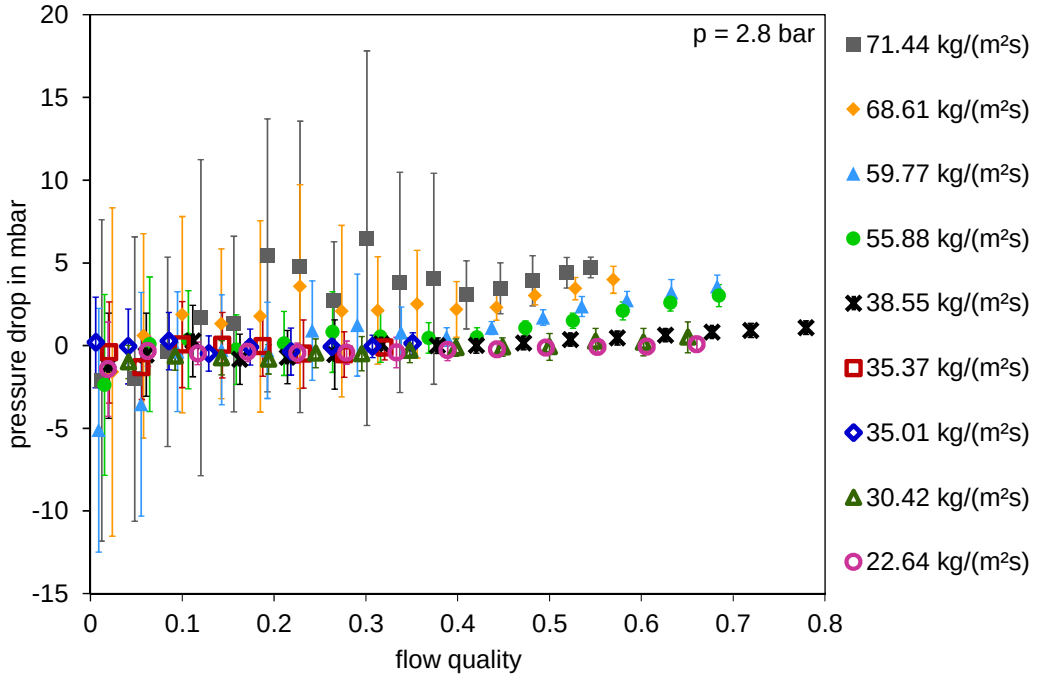

Fig. 7.13: Measured nitrogen two-phase pressure drop in the 1 m long **vertical downward** part of the test section versus the flow quality for nine different mass velocities. Measurement conditions: adiabatic, $p = 2.8$ bar. For the flow quality errors in x-direction please refer to table 7.2.

velocities the rising frictional pressure drop is the main contributor to the overall pressure drop. But the frictional pressure drop in the vertical downward part is smaller than the frictional pressure drop in the horizontal part at the same flow quality and mass velocity, what contradicts [33]. As seen in figure 7.14 the program fails to predict the pressure drop of the vertical downward part of the test section when applying the Rouhani correlation for the void fraction and the Müller-Steinhagen and Heck model for the frictional pressure drop, as chosen in section 7.3.1 and section 7.3.2. All the other void fraction correlation also fail, what is not depicted here. This unexpected behaviour of the pressure drop at vertical downward flow orientation is further investigated in the next section.

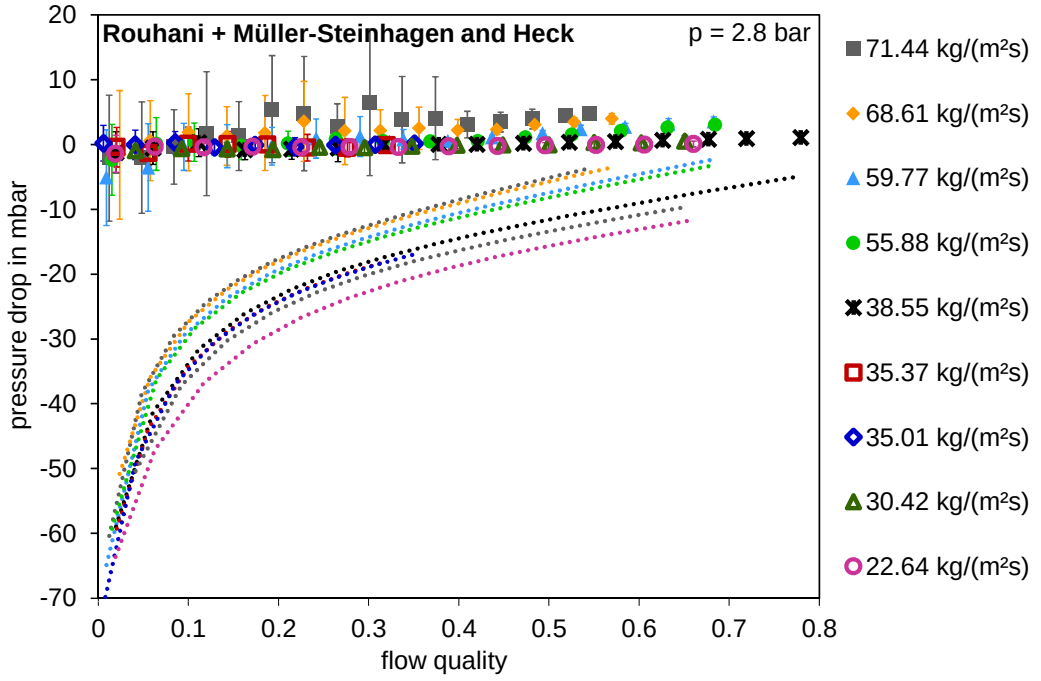

Fig. 7.14: Comparison of the measurement data (markers) for the pressure drop in the **vertical downward** part with the calculated pressure drop (dotted lines). Applied void fraction correlation: Rouhani. For the flow quality errors in x-direction please refer to table 7.2.

7.4 Validation of the two-phase flow pressure drop measurements in the vertical downward part

In order to validate the measurement data, especially in the vertical downward direction and at low flow qualities, the pressure drop in liquid flow has been measured. Subsequently, the flow has been directly heated into the two-phase area with heater EH002 (needle valve completely open) and the response of the differential pressure transmitters have been observed. Figure 7.15 shows the course of the differential pressure for all three parts of the test section as well as the course of the temperature TTN03 versus time. The step function of the applied heating power is shown by the calculated enthalpy of the flow. The horizontal line indicates the enthalpy at the boiling point. At the beginning of the measurement heater EH002 is off and the flow at a pressure of about 2.8 bar and at a temperature of about 82 K is definitely in the liquid phase according to NIST. As can be seen, the frictional pressure drop in the horizontal part of the test section is, as expected,

extremely small. Because the lower limit of the differential pressure sensor for the horizontal part is 0 mbar, the noise of the sensor seems to be only in the direction of positive values. The pressure loss in the vertical upward part and the pressure gain in the vertical downward part are the same, according to the absolute value, and also correspond to the expected value in liquid flow. Then, the heater EH002 is switched on and increased stepwise until a flow quality of about 8 % is reached. Temperature TTN03 indicates from which time on the flow has reached the two-phase area. According to NIST, the saturation temperature corresponding to the saturation pressure of 2.8 bar is about 87 K. One can observe that, even shortly before the flow reaches two-phase conditions, probably when the first bubbles are formed locally in the heater, the pressure gain in the vertical downward part jumps to a value close to zero. The pressure loss in the vertical upward part only drops when the two-phase conditions are reached and it drops in a more moderate way. When the heater power is reduced again, mirror-inverted to switching on the heater, firstly the pressure drop in the vertical upward part sharply increases again, whereas the pressure gain on the vertical downward part rises with some time delay. In summary, two observations can be made. Firstly, the pressure gain in vertical downward flow can be measured correctly with the experimental setup for liquid flow, proofing that the pressure gain in vertical downward two-phase flow is negligible. Secondly, entering the two-phase area by heating causes delay in boiling and the flow is not in thermodynamic equilibrium as, for vertical upward flow, the same pressure drop values as in liquid flow are measured at a time when the flow is theoretically already in two-phase conditions. The measurement data for the pressure drop in vertical upward flow at low flow qualities is lower than the predicted one, because in the measurements described before in section 7.3 the two-phase area is entered by a Joule-Thomson expansion forcing the flow instantly into thermodynamic equilibrium. This is one possible explanation for the differences for low flow quality described by the models and former studies and the here presented measurement data.

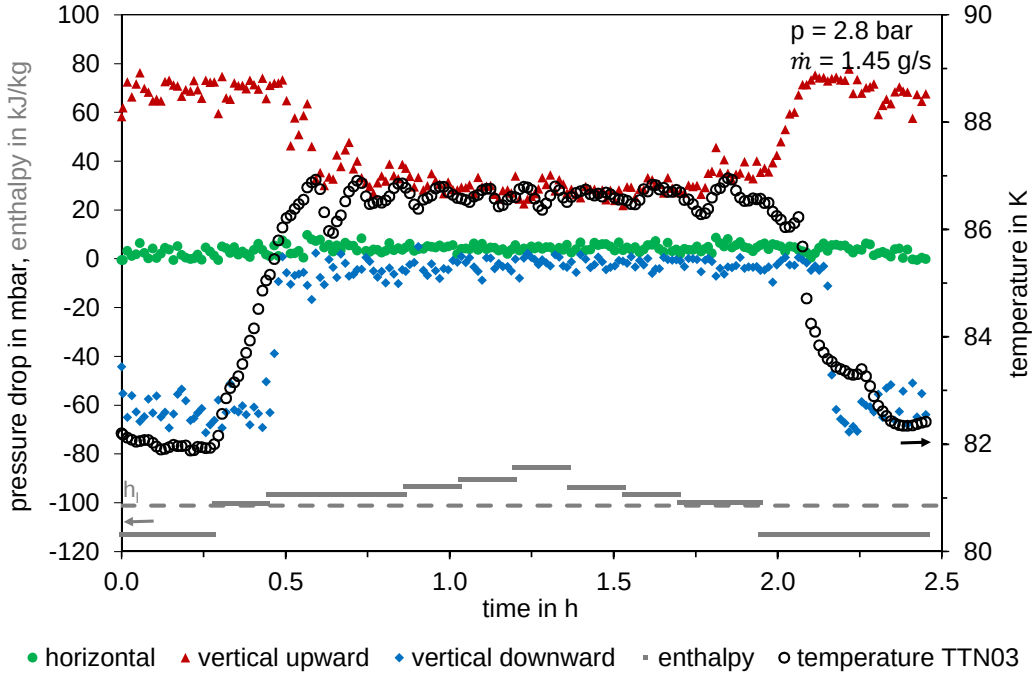

Fig. 7.15: Behaviour of the pressure drop in all three parts of the test section while heating from single-phase flow into two-phase flow region. Two-phase flow conditions are reached when temperature TTN03 is constant at around 87 K and 0.5 h. The calculated enthalpy of the flow represents the step function of the applied heater power of EH002. The horizontal dashed line indicates the enthalpy at the boiling point. Measurement conditions: $p = 2.8\,\mathrm{bar}$, $\dot{m} = 1.45\,\mathrm{g\,s^{-1}}$.

7.5 Cool-down behaviour of the experimental setup

The cool-down behaviour of the small-scale experimental setup has been investigated. The first cool-down test started from an initial setup temperature of about 286 K under the following conditions: precooler filled with LN_2 at 78 K, needle-valve completely open, opening inlet valve CVN01: 50 %, opening outlet valve CVN02: 100 %. Figure 7.16 shows the change of the temperatures TTN01, TTN03, TTN04, TTN05 and TTN06 versus time as well as the change of the mass flow and the change of the pressure PTN03 versus time. To memorize, the temperature sensors TTN01, TTN03 and TTN04 are located at different positions of the cryostat insert, whereas TTN05 is attached on the lowest top plate and TTN06 is mounted at the bottom of the radiation shield, see figure 7.1. The inlet valve CVN01 is opened after approximately 25 min. The temperatures TTN01 to

TTN05 drop from their initial value to 82 K within 15 min. The closer the temperature sensor is located at the beginning of the test insert, the faster the temperature decreases. The temperature TTN06 of the radiation shield only decreases slowly. Interestingly, the temperature TTN04 firstly drops to the final value of about 82 K, but then rises again, until it reaches the temperature of the warmer lowest top plate (TTN05) and finally, both temperatures TTN04 and TTN05, drop again and reach 82 K. It seems that the

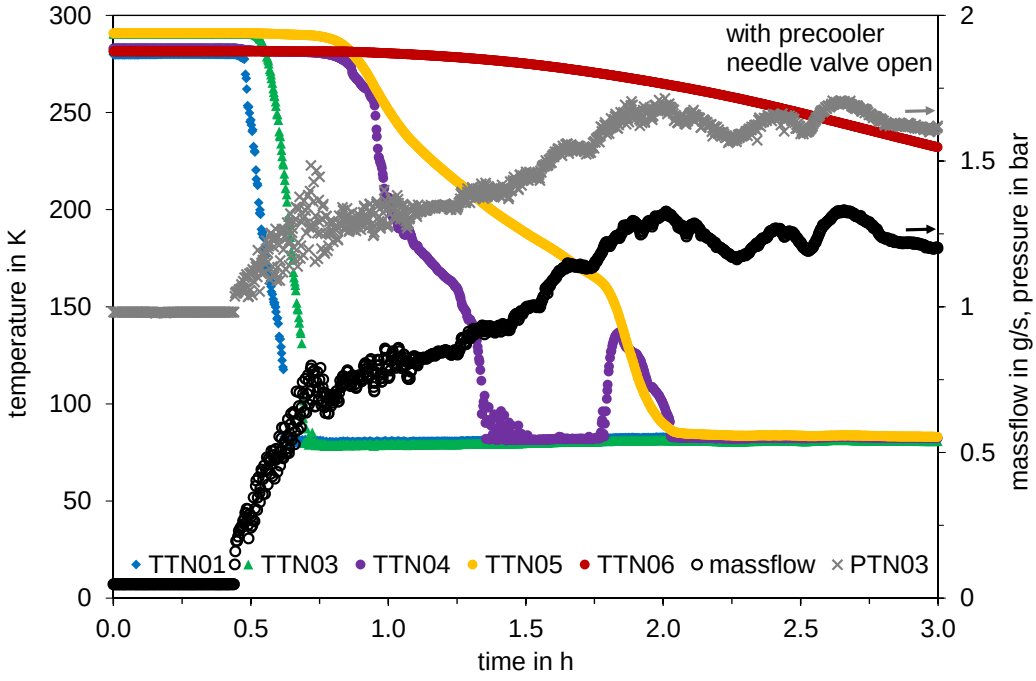

Fig. 7.16: Cool-down curve of the experimental setup also indicating the mass flow and pressure change while cool down. Cool-down conditions: precooler filled with LN_2, **needle-valve completely open**, opening inlet valve CVN01: 50 %, opening outlet valve CVN02: 100 %.

temperature sensor TTN04, which is located close to the lowest top plate of the cryostat, is influenced by two different mechanisms, on the one hand the cooling due to the nitrogen flow, and on the other hand the heating due to the still warm lowest top plate, enhanced by the good thermal conductivity of cooper. As soon as the lowest top plate (TTN05) has reached the same temperature as the end of the test insert (TTN04), the latter phenomena ceases and the total insert cools down. The mass flow and analogically the pressure rise steeply, shortly after the opening of inlet valve CVN01 and then approach an approximate

constant value. The better the insert is cooled down, the lower is the heat input into the nitrogen flow and the less of the nitrogen flow evaporates. Hence, the mass flow increases because of the higher density of the liquid compared to the vapour. The whole cool down takes about 100 minutes.

A second cool-down test has been performed from a lower temperature of about 264 K and under the same conditions as the first cool-down except of the needle valve adjusted to operation conditions. Figure 7.17 and figure 7.18 show the course of the temperatures TTN01 to TTN06 versus time as well as the course of the mass flow or the pressures PTN01 (before needle valve) and PTN03 (after needle valve) versus time. As can be seen, it is not possible, even not after one day, to cool down the insert with the needle valve adjusted to operation conditions. Temperature TTN01 and TTN02 drop about 100 K and the temperatures TTN03 and TTN04 only drop scarcely. The mass flow is with 0.06 g s^{-1} distinctively lower than in the first cool-down test. Visible in figure 7.18, the pressure

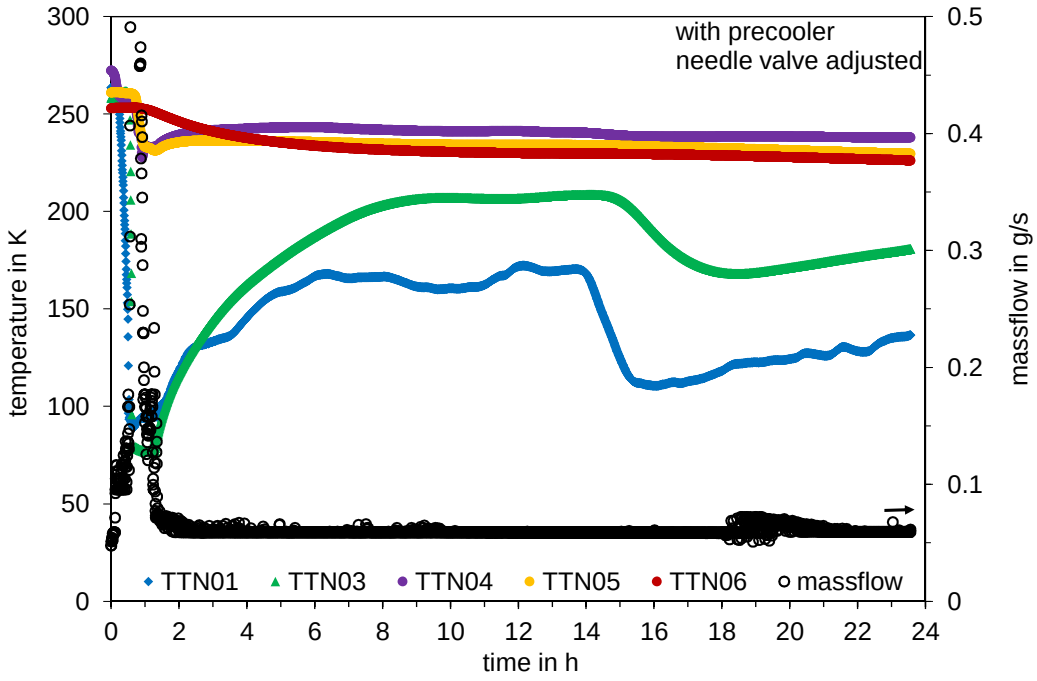

Fig. 7.17: Cool-down curve of the experimental setup also indicating the mass flow change while cool down. Cool-down conditions: precooler filled with LN_2, **needle-valve adjusted to operation condition**, opening inlet valve CVN01: 50 %, opening outlet valve CVN02: 100 %.

is only build up before the needle valve (PTN01), whereas the pressure after the needle valve (PTN03) stays at its initial value. An interesting effect is, that directly after opening the inlet valve CVN01 the insert starts to cool down, but then apparently so much liquid evaporates that the system is kind of blocked and warms up again. On this observation the proposed design of the cooling system for the large-scale ICARUS detector's thermal shield is based, see chapter 8.

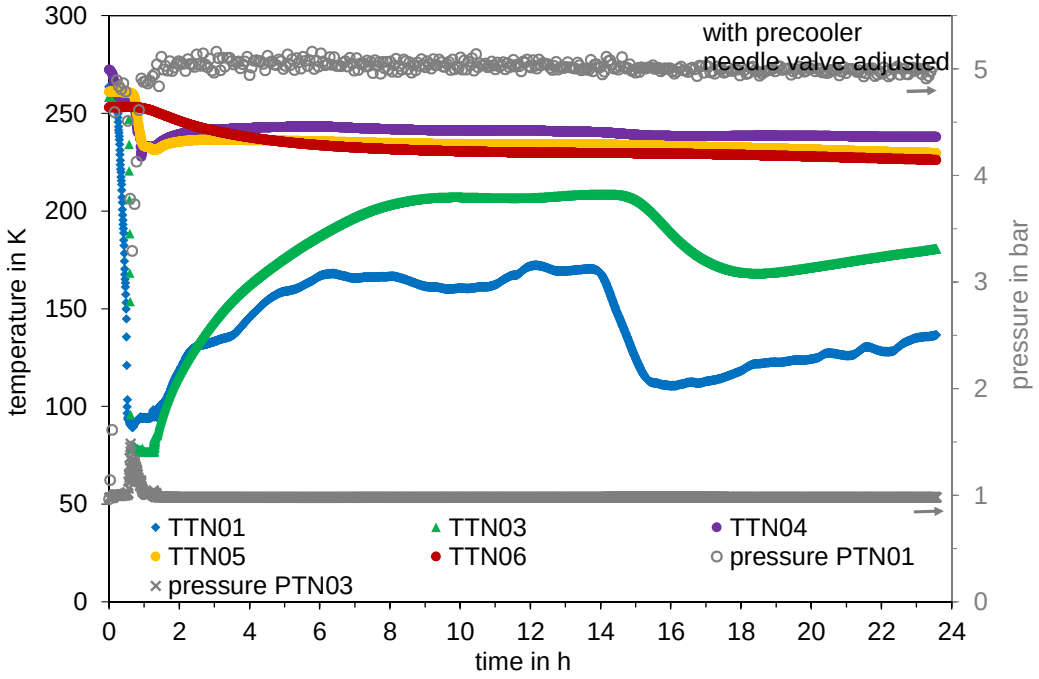

Fig. 7.18: Cool-down curve of the experimental setup also indicating the pressure change while cool down. Cool-down conditions: precooler filled with LN_2, **needle-valve adjusted to operation condition**, opening inlet valve CVN01: 50 %, opening outlet valve CVN02: 100 %.

8 Nitrogen two-phase cooling circuit for the thermal shield of the ICARUS detector

In this chapter the two-phase pressure drop of nitrogen flow in one 11 m long cooling loop of the thermal shield of the ICARUS detector is calculated. Moreover, an initial design for the nitrogen two-phase cooling circuit for the thermal shield is presented and discussed, considering all previous depicted results. However, the proper ICARUS T600 detector is treated as "black box", as the design of the detector itself is not within the responsibility of the Cryolab at CERN. One takes a closer look at required safety measures of the full-scale cooling system. An additional heat input during an incident can build up high pressure in cryogenic systems as the coolant evaporates. At ambient pressure the volume ratio between the vapour phase at room temperature and the liquid phase is about 700. Safety measures to prevent excessive overpressure are discussed.

8.1 Pressure drop in an 11 m long cooling loop of the thermal shield

The pressure drop in one 11 m long cooling loop of the thermal shield of the ICARUS detector is calculated. To memorize the design of the thermal shield please refer to section 4.3. The pressure drop is computed by the developed Matlab® program, described in chapter 6, using the correlation according to Rouhani for the void fraction and the model according to Müller-Steinhagen and Heck for the frictional pressure drop. Both are considered to fit the experimental data best for nitrogen two-phase flow at the conditions of the thermal shield, see section 7.3.

The following input values have been passed to the program: inner pipe diameter of 10 mm, pipe section 1 and pipe section 3 (horizontal) with a length of 3.6 m each, pipe section 2 (vertical upward) with a length of 3.9 m, mass flow of $2\,\mathrm{g\,s^{-1}}$, heat load of $20\,\mathrm{W\,m^{-2}}$ per panel, inlet saturation pressure of 2.8 bar and inlet flow quality of 10 %. Figure 8.1 shows the increase of the gravitational, frictional and momentum pressure drop versus the length

of the cooling loop as well as the decrease of the absolute pressure along the shield length as computed by the Matlab® program. As can be seen in figure 8.1 the total pressure drop over the cooling loop is 98.5 mbar. The gravitational pressure drop, only located in the vertical upward section of the cooling loop, contributes with 96.6 % most to the total pressure drop. The frictional pressure drop only constitutes 3.3 % of the total pressure drop and the momentum pressure drop is rather negligible. The absolute pressure falls from 2.8 bar to 2.7015 bar, which corresponds to a temperature drop of less than 400 mK. The calculated cool-down fulfils the given requirement of a temperature gradient of the thermal shield of less than 500 mK, see section 4.3.

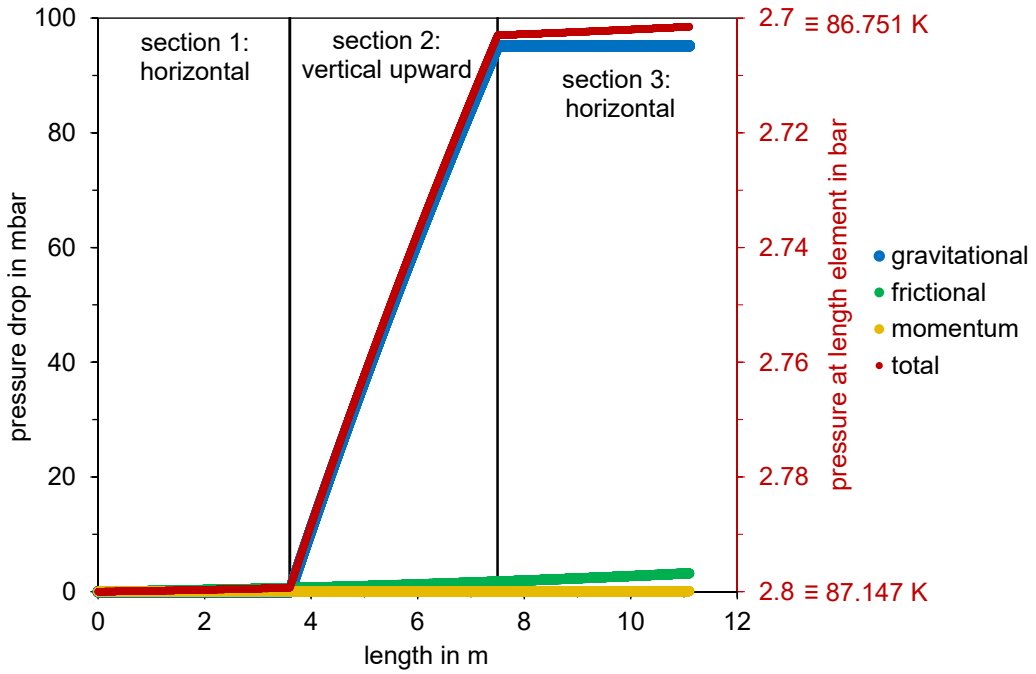

Fig. 8.1: Calculated pressure drop and corresponding reduction of the absolute pressure and temperature versus the length of the 11 m long cooling loop with an inner diameter of 10 mm. The total pressure drop is the sum of the gravitational, frictional and momentum pressure drop. Conditions: $\dot{m} = 2\,\mathrm{g\,s^{-1}}$, $p_{\mathrm{in}} = 2.8\,\mathrm{bar}$, $x_{\mathrm{in}} = 10\,\%$ and $\dot{q} = 20\,\mathrm{W\,m^{-2}}$ thermal shield panel.

Figure 8.2 depicts the change of the flow quality, the void fraction and the density versus the length. The flow quality, originating from 10 %, mounts linearly over the length of the cooling loop due to the homogeneous heat input. The void fraction rises simultaneously,

it increases more sharply at low flow qualities. The void fraction is always higher than the flow quality. The average density declines towards the vapour density over the length of the cooling loop as the flow continuously evaporates.

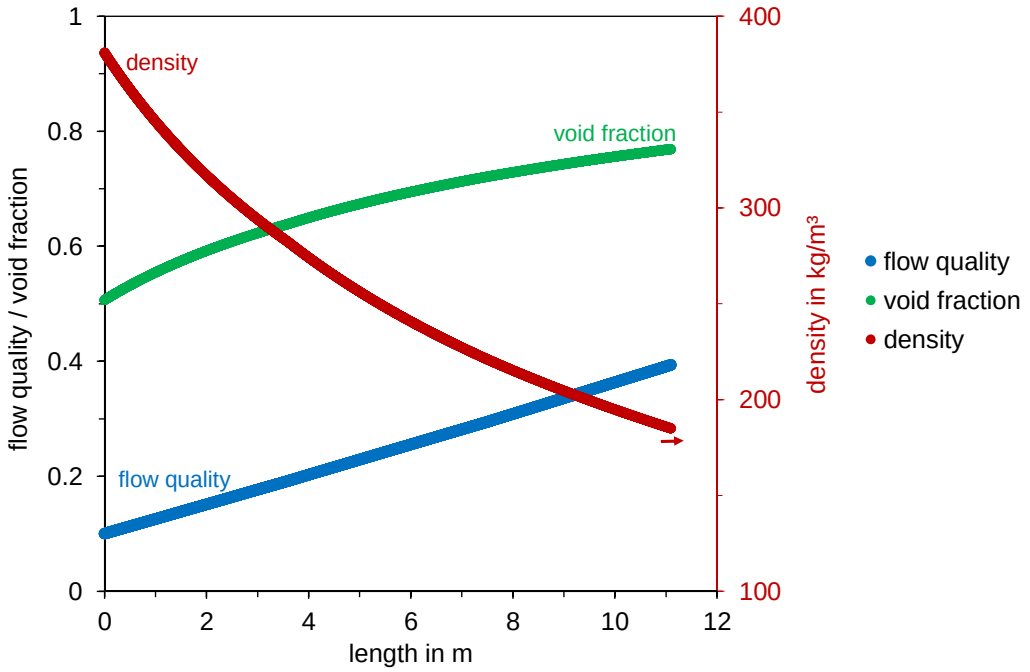

Fig. 8.2: Calculated change of the flow quality, void fraction and two-phase density versus the length of the 11 m long cooling loop with an inner diameter of 10 mm. Inlet conditions: $\dot{m} = 2\,\mathrm{g\,s^{-1}}$, $p_{\mathrm{in}} = 2.8\,\mathrm{bar}$, $x_{\mathrm{in}} = 10\,\%$ and $\dot{q} = 20\,\mathrm{W\,m^{-2}}$ thermal shield panel.

In the following the pressure drop over the 11 m long cooling loop is not only calculated at nominal conditions, but also at varying mass flow, inlet flow quality and heat load. The parametric study should investigate the behaviour of the cooling system when deviations from the nominal conditions occur. The total pressure drop is computed for mass flows in the range of $0.8\,\mathrm{g\,s^{-1}}$ to $3.2\,\mathrm{g\,s^{-1}}$ ($\pm 60\,\%$ of the nominal value of $2\,\mathrm{g\,s^{-1}}$), for the nominal inlet flow quality of 10 % and a lower one of 1 %, as well as for the nominal heat load of $20\,\mathrm{W\,m^{-2}}$ and a reduced one of $10\,\mathrm{W\,m^{-2}}$, see figure 8.3. A lower heat load is chosen, because it is common practice that the given constraints include an operational margin. The following dependencies can be observed. At constant heat load, but decreasing inlet flow quality, the total pressure drop rises. At constant flow quality, but decreasing heat load, the total pressure drop is also augmented.

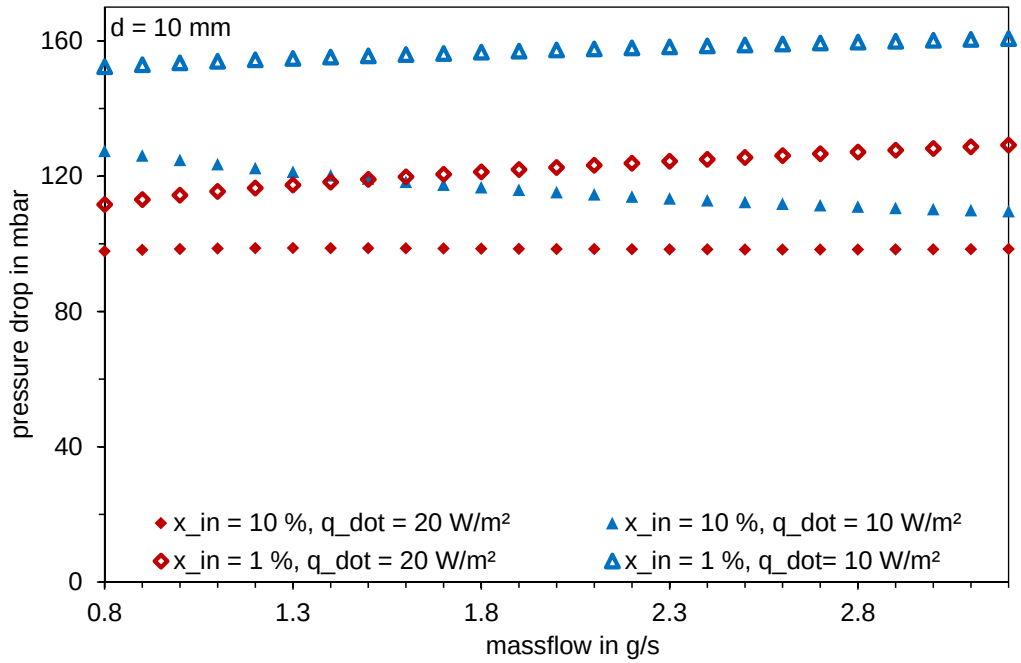

Fig. 8.3: Total pressure drop over the 11 m long cooling loop with an **inner diameter of 10 mm** versus mass flow in the range of $0.8\,\mathrm{g\,s^{-1}}$ to $3.2\,\mathrm{g\,s^{-1}}$. Parametric study for different combination of $x_{\mathrm{in}} = 1\,\%$, $x_{\mathrm{in}} = 10\,\%$ and $\dot{q} = 10\,\mathrm{W\,m^{-2}}$, $\dot{q} = 20\,\mathrm{W\,m^{-2}}$ at $p_{\mathrm{in}} = 2.8\,\mathrm{bar}$.

To memorize, the gravitational pressure drop is the biggest contributor to the total pressure drop. In both cases, the average flow quality along the loop is reduced, and consequently, the average two-phase density increases, resulting in a higher gravitational pressure drop. The dependency of the total pressure drop on the mass flow is more complex. At low inlet flow qualities of 1 % the total pressure drop and the mass flow are positively correlated. At high inlet flow qualities of 10 % and a heat load of $20\,\mathrm{W\,m^{-2}}$ the total pressure drop is nearly constant over the mass flow range, whereas at a heat load of $10\,\mathrm{W\,m^{-2}}$ the total pressure is negatively correlated with the mass flow. To memorize, the void fraction according to the correlation of Rouhani increases with rising flow quality as well as rising mass velocity. At constant inlet flow quality and constant heat load, but higher mass flow, the outlet flow quality diminishes. Depending on the absolute value of both, the flow quality and the mass velocity, either the effect of increased mass velocity or the effect of reduced flow quality dominates. In the former case the void fraction rises, leading to a lower gravitational pressure drop. In the latter case of reduced flow quality the void fraction drops, resulting

in a higher gravitational pressure drop. The flow quality effect seems to outweigh the mass velocity effect rather at low flow qualities because the slope of the void fraction versus the flow quality is larger at low flow qualities, see figure 5.5. In the case, in which the effect of increasing mass flow predominates the effect of reduced flow quality, and the pressure drop and the mass flow are negatively correlated, the cooling system destabilizes itself and can run into a dry-out. Assuming that the mass flow temporarily decreases in one of the 42 parallel cooling loops due to mass flow fluctuations, the pressure drop in this cooling loop is higher compared to the other cooling loops, preventing fluid to sufficiently enter this cooling loop and causing a dry-out. With smaller pipe diameter, that means, higher mass velocity, the dependency of the void fraction according to Rouhani on the mass velocity is diminished, see figure 5.6, and consequently, the effect of the flow quality starts to always predominate the effect of the mass velocity, see figure 8.4.

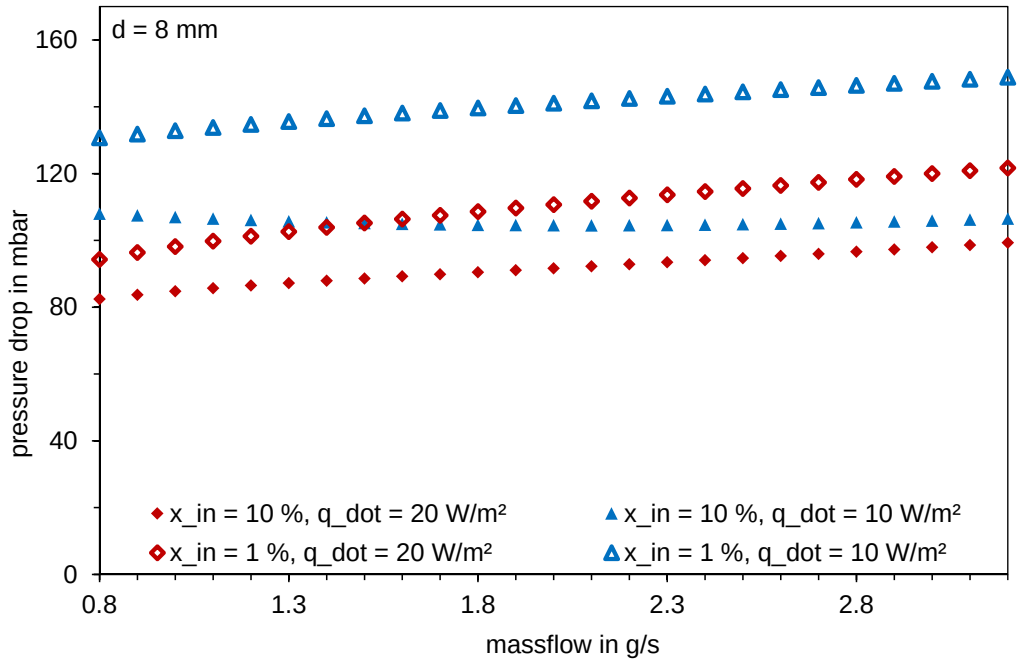

Fig. 8.4: Total pressure drop over the 11 m long cooling loop with an **inner diameter of 8 mm** versus mass flow in the range of $0.8\,\mathrm{g\,s^{-1}}$ to $3.2\,\mathrm{g\,s^{-1}}$. Parametric study for different combination of $x_{\mathrm{in}} = 1\,\%$, $x_{\mathrm{in}} = 10\,\%$ and $\dot{q} = 10\,\mathrm{W\,m^{-2}}$, $\dot{q} = 20\,\mathrm{W\,m^{-2}}$ at $p_{\mathrm{in}} = 2.8\,\mathrm{bar}$.

At a pipe diameter of 6 mm the destabilizing effect is even eliminated as the pressure drop and the mass flow are always positively correlated, see figure 8.5. The differences

between various inlet flow qualities or various heat loads become less distinct at low pipe diameters. For a pipe diameter of 6 mm and nominal conditions with an inlet flow quality of 10 % and a heat load of $20\,\mathrm{W\,m^{-2}\,s^{-1}}$ the total pressure drop along the cooling loop increases to 108 mbar. Nonetheless, with a corresponding temperature drop of 433 mK the requirements regarding the temperature gradient along the thermal shield are fulfilled.

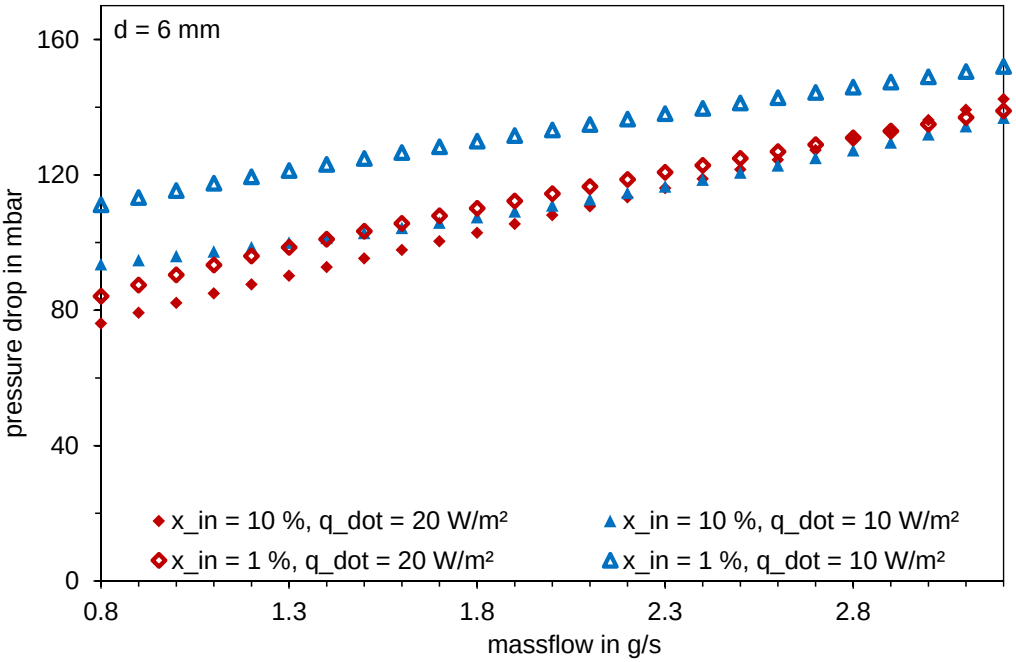

Fig. 8.5: Total pressure drop over the 11 m long cooling loop with an **inner diameter of 6 mm** versus mass flow in the range of $0.8\,\mathrm{g\,s^{-1}}$ to $3.2\,\mathrm{g\,s^{-1}}$. Parametric study for different combination of $x_{\mathrm{in}} = 1\,\%$, $x_{\mathrm{in}} = 10\,\%$ and $\dot{q} = 10\,\mathrm{W\,m^{-2}}$, $\dot{q} = 20\,\mathrm{W\,m^{-2}}$ at $p_{\mathrm{in}} = 2.8$ bar.

In figure 8.6 and figure 8.8 (flow pattern map for horizontal flow according to Taitel and Dukler) as well as figure 8.7 and figure 8.9 (flow pattern map for vertical flow according to Hewitt and Roberts) it can be seen which flow pattern will occur in the 11 m long cooling loop with an inner diameter of 10 mm or 6 mm. The lowest discussed mass flow of $0.8\,\mathrm{g\,s^{-1}}$, the nominal mass flow of $2.0\,\mathrm{g\,s^{-1}}$ and the highest discussed mass flow of $3.2\,\mathrm{g\,s^{-1}}$ as well as all combinations of the inlet flow qualities and heat loads are included in the maps. The markers represent always the inlet and the outlet condition of each section of the cooling panels. As the cooling loop has two horizontal, but only one vertical upward section, there are four markers in the horizontal flow pattern map for each condition, but only two

markers in the vertical flow pattern map. For an inner pipe diameter of 10 mm stratified or wavy flow occur in the horizontal sections and chaotic flow occurs in the vertical upward section.

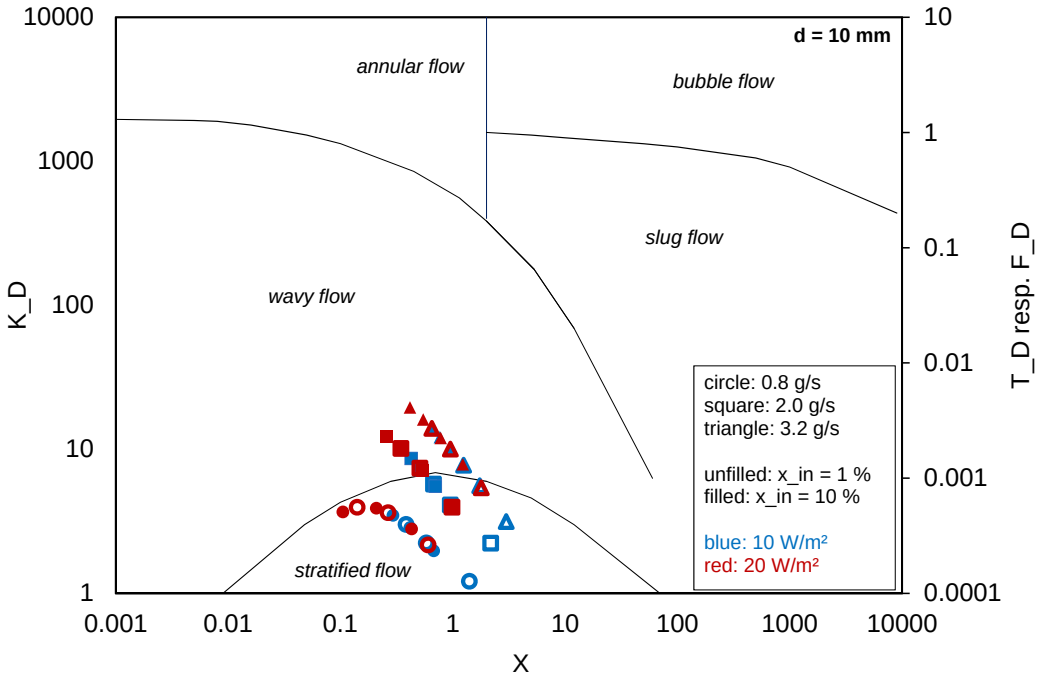

Fig. 8.6: Flow pattern map according to Taitel and Dukler for horizontal flow as explained in section 5.1.2. Indicated is the flow regime of nitrogen two-phase flow in the 11 m long cooling loop with an **inner diameter of 10 mm** at three different mass flows and the conditions equivalent to figure 8.3.

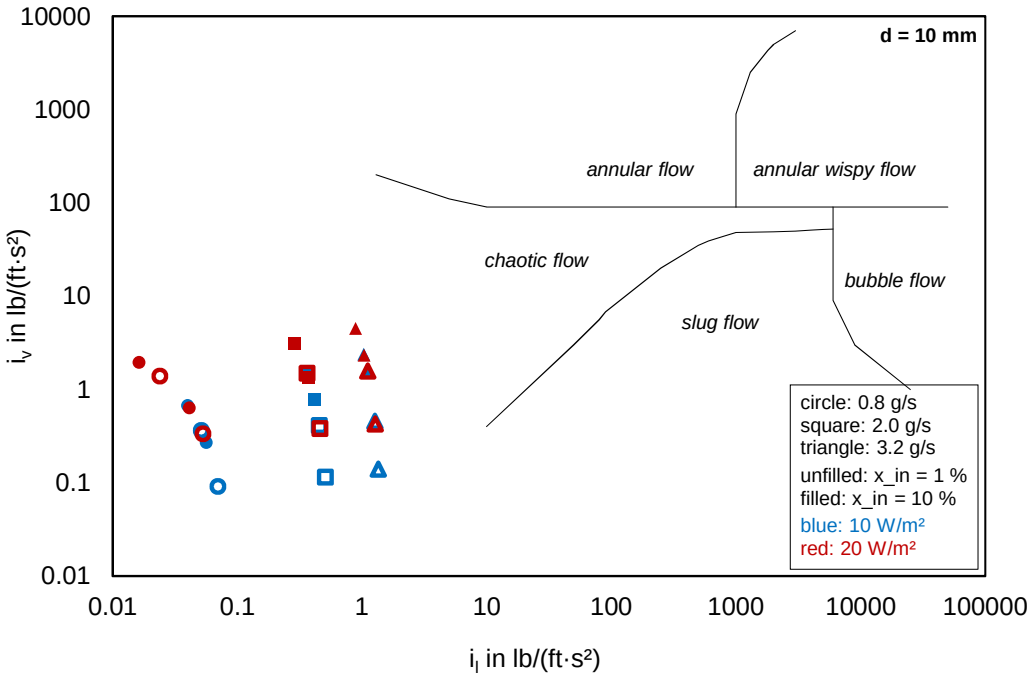

Fig. 8.7: Flow pattern map according to Hewitt and Roberts for vertical flow as explained in section 5.1.2. Indicated is the flow regime of nitrogen two-phase flow in the 11 m long cooling loop with an **inner diameter of 10 mm** at three different mass flows and the conditions equivalent to figure 8.3.

For an inner pipe diameter of 6 mm the flow regime of the vertical upward section is still chaotic, whereas the flow regime for the horizontal part is shifted more in the direction of annular flow. Nevertheless, for low mass flows and low flow qualities, stratified or wavy flow still occurs. For the nominal mass flow of $2.0\,\mathrm{g\,s^{-1}}$, nominal heat load of $\dot{q} = 20\,\mathrm{W\,m^{-2}}$ and nominal inlet flow quality of $x_{\mathrm{in}} = 10\,\%$, annular flow occurs in the horizontal part. That would also be preferable with regard to a stable flow with well defined frictional pressure drop, see section 7.3.1. Consequently, based on operational considerations the design of the cooling loop with an inner pipe diameter of 6 mm should be preferred because the working conditions of the cooling system are more stable.

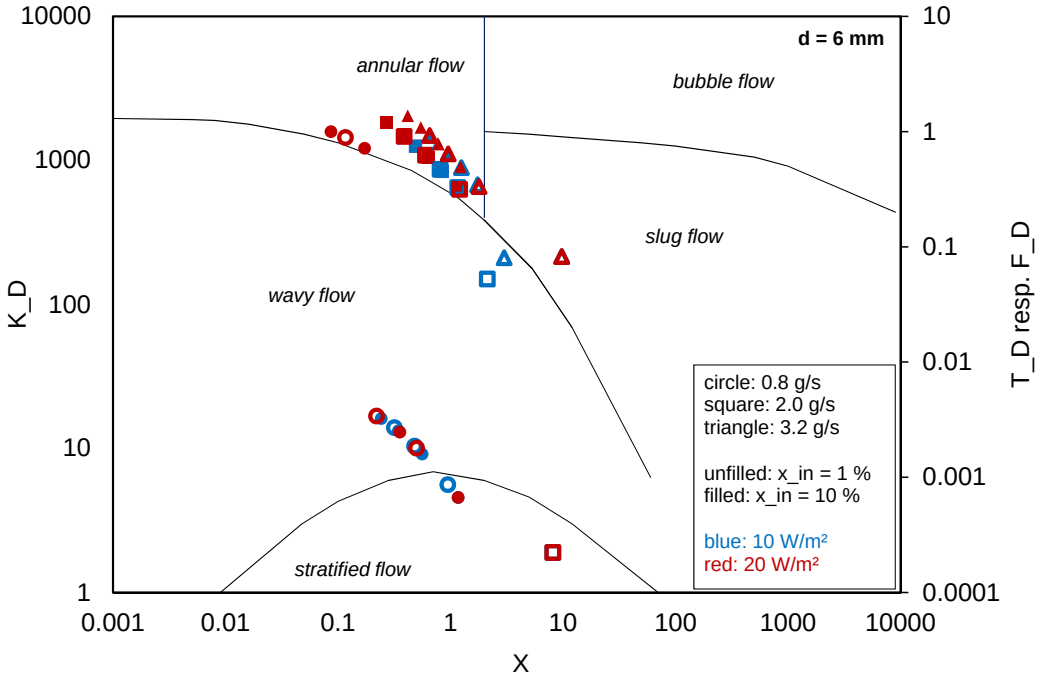

Fig. 8.8: Flow pattern map according to Taitel and Dukler for horizontal flow as explained in section 5.1.2. Indicated is the flow regime of nitrogen two-phase flow in the 11 m long cooling loop with an **inner diameter of 6 mm** at three different mass flows and the conditions equivalent to figure 8.5.

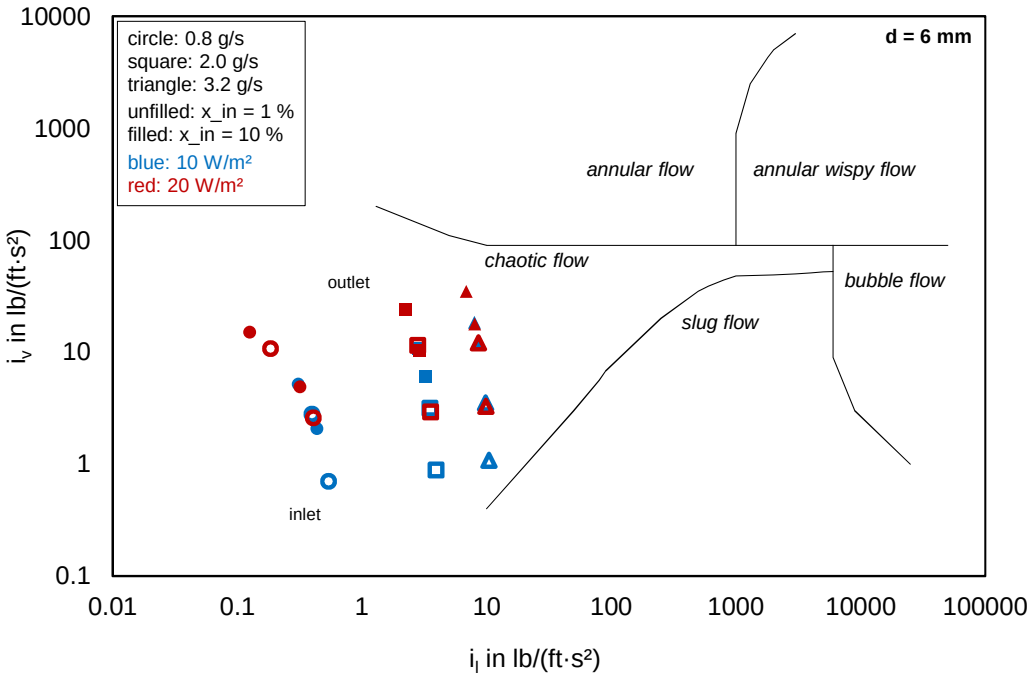

Fig. 8.9: Flow pattern map according to Hewitt and Roberts for vertical flow as explained in section 5.1.2. Indicated is the flow regime of nitrogen two-phase flow in the 11 m long cooling loop with an **inner diameter of 6 mm** at three different mass flows and the conditions equivalent to figure 8.5.

8.2 Design of the cooling circuit with focus on the thermodynamic conditions

Figure 8.10 shows the piping and instrumentation diagram (P&ID) of the nitrogen two-phase cooling circuit for the thermal shield of the ICARUS T600 detector and figure 8.11 illustrates the thermodynamic cooling process in the p-h diagram. Liquid nitrogen is provided by the phase separator. The vessel has a diameter of 0.8 m and a height of 2 m, thus, having a capacity of 1 m^3. Starting with an initial filling quantity of 80 %, the operation of the cooling system can be maintained for about 1 hour without any supply. The vessel represents with 2.1 bar the lowest pressure level of the whole cooling circuit. The pressure is kept by the pressure sensor PT01 regulating control valve CV02. The corresponding saturation temperature of nitrogen to 2.1 bar is higher than the freezing temperature of argon at ambient pressure. Hence, freezing of argon is prevented under all

circumstances. The filling level of the vessel is adjusted by the level gauge LT01 controlling the nitrogen supply through control valve CV01, enabling 179.2 g nitrogen flow through the cooling system per second, see section 4.3. To create a mass velocity of 25.5 $\mathrm{kg\,m^{-2}\,s^{-1}}$, equivalent to the mass velocity in a 10 mm pipe of the thermal shield, the inner supply pipe diameter is determined at 95 mm. The hydrostatic height of the liquid nitrogen in the vessel as well as the vertical pipe after the vessel allow to subcool the liquid nitrogen, which is especially important for the operation of the subsequent pump being disturbed of a too high vapour content in the flow. The pump operates at a performance of 3 bar pressure difference. The valves CV03 and CV04 enable an exchange of the pump in case of breakdown. The bypass can be fully opened while cool down and is otherwise controlled by pressure sensor PT02 with control valve CV05 to keep the pressure after the pump constant. The heater EH01 before the detector provides a heating power of approximately 4 kW adjusting the initial point for the isenthalpic Joule-Thomson expansion within the detector, so that the flow quality after the expansion into the two-phase-area is around 10 %. The two-phase area is entered by an isenthalpic Joule-Thomson expansion realized by capillaries and not by heating in order to prevent boiling delay. The bypass around the detector itself has to be opened during cool down. After the system is cooled down it can be closed and the flow can pass through the Joule-Thomson expansion. The pipe length between the control valves CV03 and CV04 is assumed to be 15 m, between the control valves CV04, CV05 and CV06 20 m and between the control valves CV05 and CV06, excluding the detector itself, 10 m. For illustrating the cooling cycle in the p-h diagram the following three assumptions have been made. Firstly, the pressure drop of the liquid nitrogen flow is negligible. Secondly, the heat input in all vacuum-insulated pipes is 5 $\mathrm{W\,m^{-1}}$. Thirdly, the heat input of the pump is 10 W.

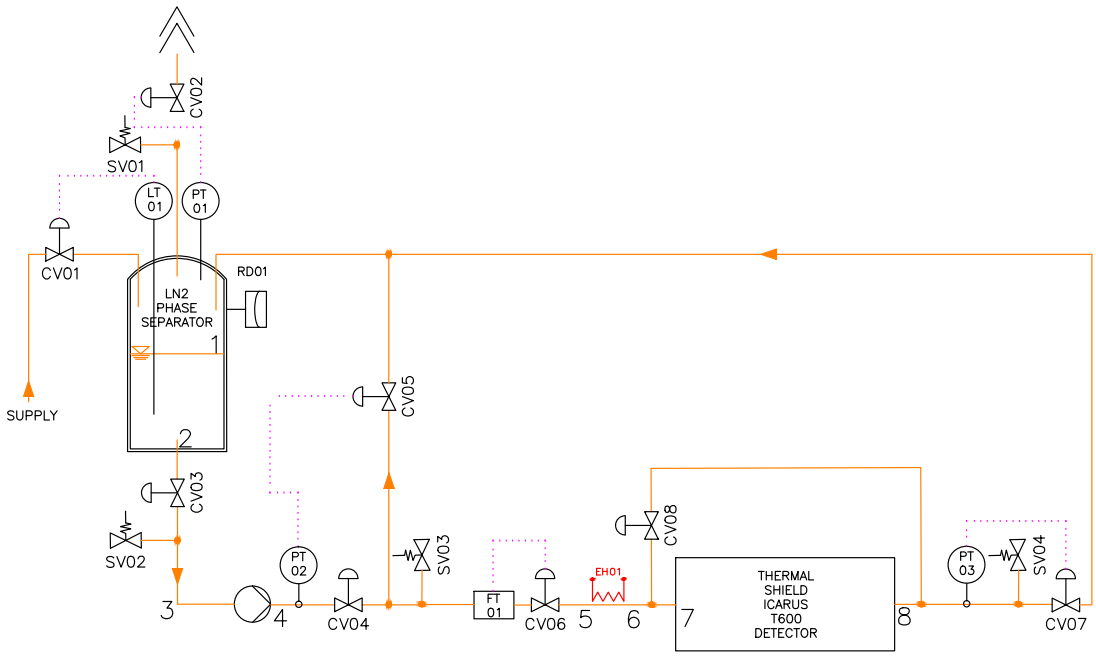

Fig. 8.10: P&ID of the nitrogen two-phase cooling circuit for the thermal shield of ICARUS T600 detector.

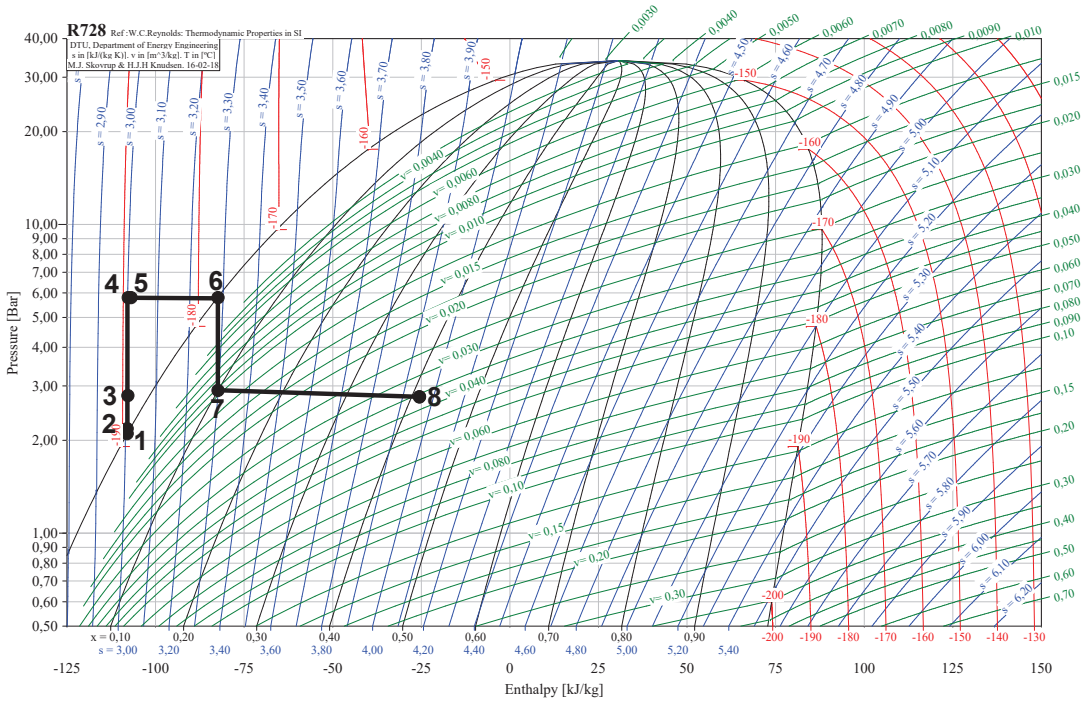

Fig. 8.11: Pressure-enthalpy diagram of nitrogen showing the thermodynamic process in the cooling circuit for the thermal shield of the ICARUS detector. The numbers correspond to the numbers used in the P&ID, see figure 8.10.

8.3 Pressure safety analysis and required safety devices

Generally, the control loop design of the thermal shield of the ICARUS T600 detector ensures safe operation. The inlet control valve CV06 controls the mass flow via the flowmeter FT01, whereas the outlet control valve CV07 controls the pressure via the pressure sensor PT03. If the pressure in the thermal shield exceeds the specified upper threshold, control valve CV07 keeps the pressure at nominal conditions. Consequently, the pressure in the thermal shield drops and the system is in safe operation again. If it would be the other way round – the inlet control valve controls the pressure and the outlet control valve controls the mass flow – both valves would close in case of pressure build-up, creating a closed system in which the pressure is trapped and cannot be released during normal operating procedures. This control loop design of the thermal shield is important also for

the cool-down process allowing to control the pressure after the isenthalpic Joule-Thomson expansion with the possibility to keep the system at the required temperature level.

Nevertheless, the cooling system of the thermal shield of the ICARUS detector has to be protected against excessive pressures by use of safety valves or rupture disks. Each subsystem, which can be completely closed, has to be separately equipped with according safety devices. As can be seen in figure 8.10 the inner vessel of the phase separator is protected by the safety valve SV01, whereas the outer vacuum vessel is protected by the rupture disk RD01 ensuring absolute leak-tightness working in an underpressure environment. All parts of the piping system have a separate safety valve, SV02, SV03 and SV04 respectively. The design of the safety devices has been done in the following five steps according to the standards DIN EN 13648 [37] and DIN EN ISO 4126 [38] as well as [12].

1. Determination of the heat input during a hazardous incident:
   The heat input in the system is increased dramatically by venting of air into the insulation vacuum. The mechanism of the resulting heat input into the system is quite complex as probably water out of the atmospheric moist air is frozen out as well as oxygen is condensed at the cold inner surface, influencing the heat transfer. Lehmann [39, 40] conducted some measurements determining the maximum heat input of $\dot{q} = 2000\,\mathrm{W\,m^{-2}}$ in case of air inleak the insulation vacuum of a liquid nitrogen cooling panel covered with 10 layers of MLI (multi-layer-insulation).

2. Determination of the required mass flow to be discharged through the safety device:
   The required mass flow to be discharged through the safety device is calculated in compliance with DIN EN 13648-3 according to the following equation:

$$\dot{m} = \frac{\dot{Q}}{\Delta h_\mathrm{v}} = \frac{\dot{q} \cdot A}{\Delta h_\mathrm{v}} \quad . \tag{8.1}$$

   If the fluid volume contains liquid and respectively vapour, the evaporation enthalpy Δh_v is usually defined as the enthalpy difference between the saturated vapour and the saturated liquid at the given pressure. But if vessel contains single-phase liquid or vapour, the standard definition of the evaporation enthalpy is not applicable any more and a superficial specific evaporation enthalpy $\Delta h'_\mathrm{v}$ is introduced:

$$\Delta h'_\mathrm{v} = v \cdot \left[\frac{\partial h}{\partial v}\right]_\mathrm{p} \quad . \tag{8.2}$$

   As the cross-section A of the safety device is proportional to $A \sim \dot{Q}\,\sqrt{v}\,v^{-1}\,\left[\frac{\partial h}{\partial v}\right]_\mathrm{p}^{-1}$ (as we will see later), the maximum value of $Y = \sqrt{v}\,v^{-1}\,\left[\frac{\partial h}{\partial v}\right]_\mathrm{p}^{-1}$ will be used for the design of the safety device. In figure 8.12 Y is logarithmically plotted versus the

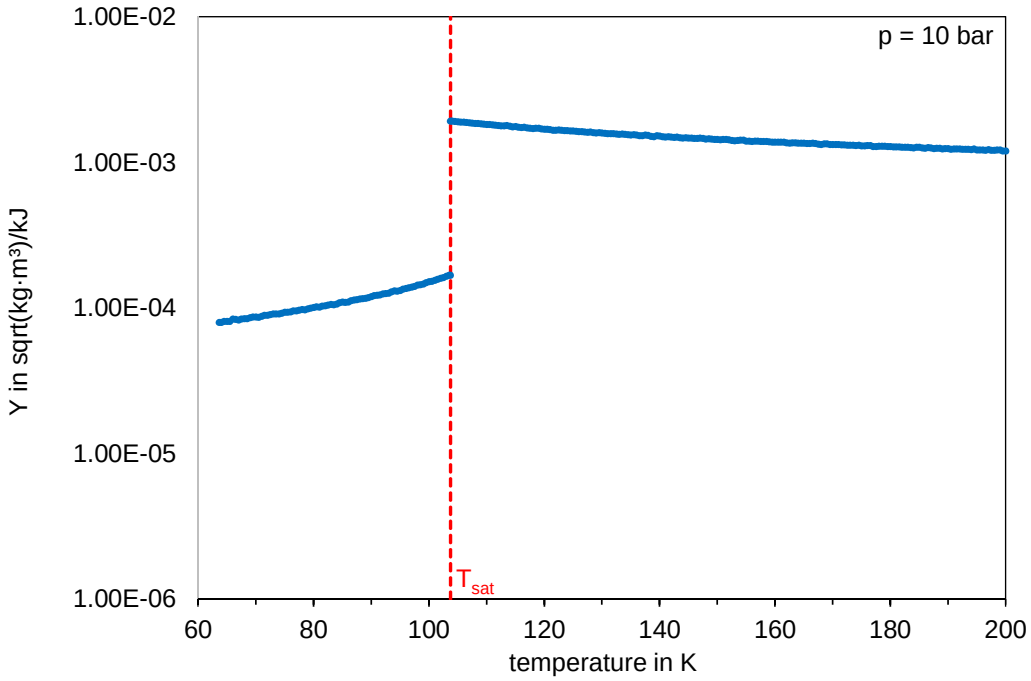

Fig. 8.12: Heat load - mass flow transfer function $Y = \sqrt{v}\, v^{-1} \left[\frac{\partial h}{\partial v}\right]_{\mathrm{p}}^{-1}$ in $\sqrt{\mathrm{kg} \cdot \mathrm{m}^3}\,\mathrm{kJ}^{-1}$ versus temperature at a pressure of 10 bar for nitrogen. The red dashed line indicates the saturation temperature of nitrogen at 10 bar. At temperatures lower than the saturation temperature the flow is in the liquid phase, whereas at temperatures higher than the saturation temperature the flow is in the vapour phase.

temperature at an exemplary pressure of 10 bar. As can be seen the maximum of Y for undercritical pressures is for both, liquid area (area left from red dotted line) and vapour area (area right from red dotted line), at saturation conditions.

For the rupture disk the required mass flow to be discharged is determined by a crack in the inner vessel releasing liquid nitrogen into the insulating shell. For the calculation a crack with an inner diameter of 50 mm is assumed.

3. Determination of the required cross-section of the safety device:
   The mass flow through the safety device is calculated according to the following general equation:

$$\dot{m} = \mathrm{K_{dr}} \cdot \sqrt{\frac{p_0}{v_0}} \cdot C \cdot A \quad . \tag{8.3}$$

K_d is the valve discharge coefficient which is specified for both, liquid and gas flow, by the manufacturer and which is averaged between the liquid discharge coefficient and the vapour one for two-phase flow. K_{dr} including a safety factor of 0.9 is $K_d/0.9$. For rupture disks the discharge coefficient is normally referred to as α_d. Customary values of discharge coefficients can be found in the standards. C is the flow coefficient, a dimensionless measure for the flow through a safety device, only depending on fluid properties and the pressure ratio of back pressure p_b to set pressure p_0. The flow coefficient increases with decreasing pressure ratio $p_b\, p_0^{-1}$ until it reaches its maximum at the so-called critical pressure ratio. The computational decline of the flow coefficient for pressure ratios smaller than the critical one is only theoretical, but in reality the flow coefficient stays constant at its maximum value. At pressure ratios greater than the critical pressure ratio the flow through the safety device is at subsonic conditions, whereas at pressure ratios smaller than the critical one the flow is at sonic conditions, characterized by a constant sonic speed and a pressure jump between the critical pressure in the lowest cross-section of the safety device and the back pressure. The critical pressure ratio is the smallest physically possible pressure ratio and the sonic speed is the highest physically possible speed because otherwise the kinetic energy of the released fluid would exceed the initial potential energy of the pressurized fluid. The flow coefficient is determined by one of the following equations depending on the thermodynamic flow condition through the safety device. If the flow is in supersonic conditions the back pressure ratio is replaced by the critical pressure ratio.

- Single-phase gas flow through safety device:
  The flow coefficient for gas flow through the safety device is calculated from equation (8.4) according to DIN EN ISO 4126-7. The equation has been analytically derived by coupling the first law of thermodynamics with the continuity equation assuming ideal gas and an isentropic (adiabatic and no friction) expansion neglecting the inlet kinetic energy of the gas. κ is the isentropic coefficient determined to 1.4 for nitrogen considered as diatomic ideal gas.

$$C = \sqrt{\frac{2\kappa}{\kappa - 1}\left[\left(\frac{p_b}{p_0}\right)^{\frac{2}{\kappa}} - \left(\frac{p_b}{p_0}\right)^{\frac{\kappa+1}{\kappa}}\right]} \tag{8.4}$$

- Two-phase flow through safety device:
  The flow coefficient for two-phase flow throughout the whole safety device is calculated from equation (8.5) according to DIN EN ISO 4126-10 as well as Leung [41, 42]. The advantage of this so-called ω-method is that the flow properties

at the entrance of the safety device, which are easily accessible, are used. It assumes a frictionless flow, no heat transfer to the surroundings and mechanical equilibrium, that means no slip between the two phases. The parameter ω takes the compressibility of the two-phase flow into account. The first term of equation (8.6) describes the compressibility of the flow due to the vapour volume and the second term reflects the compressibility due to phase change occurring during depressurization. The factor N, see equation (8.7), is the boiling-delay factor taking into account that the flow might not be in thermodynamic equilibrium, which becomes more probable with increasing pressure difference over the valve. The parameter ω_{eq} assumes homogeneous two-phase equilibrium, this means $N = 1$. At constant set pressure p_0 and constant back pressure p_b but variable inlet flow quality x_0, the critical pressure ratio is decreasing with increasing flow quality approaching the value of the critical pressure ratio of the gas flow at $x_0 = 1$.

$$C = \frac{\sqrt{2\left[\omega \cdot \ln\left(\frac{p_0}{p_\mathrm{b}}\right) - (\omega - 1)\left(1 - \frac{p_\mathrm{b}}{p_0}\right)\right]}}{\omega\left(\frac{p_0}{p_\mathrm{b}} - 1\right) + 1} \tag{8.5}$$

$$\omega = \frac{x_0 \cdot v_{\mathrm{v}0}}{\kappa \cdot v_0} + \frac{c_{\mathrm{pl}0} \cdot T_0 \cdot p_0}{v_0}\left(\frac{v_{\mathrm{v}0} - v_{\mathrm{l}0}}{\Delta h_{\mathrm{v}0}}\right)^2 \cdot N \tag{8.6}$$

$$N = \left(x_0 + c_{\mathrm{pl}0} \cdot p_0 \cdot T_0 \cdot \frac{v_{\mathrm{v}0} - v_{\mathrm{l}0}}{{\Delta h_{\mathrm{v}0}}^2} \cdot \ln\left(\frac{p_0}{p_\mathrm{b}}\right)\right)^{\frac{2}{5}} \tag{8.7}$$

- Initially subcooled liquid potentially evaporating in safety device:
  The flow coefficient for initially subcooled flow throughout the safety device is calculated from equation (8.11) according to Schmidt [43], to which DIN EN ISO 4126-10 is referring to. The approach of Schmidt is an extension of the ω-model for two-phase flow. The model of Schmidt distinguishes between three different cases introducing the following three pressure ratios

$$\eta_\mathrm{b} = p_\mathrm{b}\, p_0^{-1} \tag{8.8}$$

$$\eta_{\mathrm{sat}} = p_{\mathrm{sat}}\, p_0^{-1} \tag{8.9}$$

$$\eta_{\mathrm{crit}} = p_{\mathrm{crit}}\, p_0^{-1} \quad . \tag{8.10}$$

If the flow is subsonic, $\eta = \eta_\mathrm{b}$ in the following equations and the safety device is divided into a flow region with liquid flow up to p_sat and a subsequent flow region with two-phase flow from p_sat to p_b. If the flow is supersonic and was initially slightly subcooled so that $p_\mathrm{crit} < p_\mathrm{sat}$, $\eta = \eta_\mathrm{crit}$ in the following equations. If the flow is supersonic and was initially highly subcooled so that $p_\mathrm{crit} > p_\mathrm{sat}$, $\eta = \eta_\mathrm{sat}$ in the following equations, the equation (8.11) simplifies to equation (8.14). At constant set pressure p_0 and constant back pressure p_b but variable inlet subcooling, the critical pressure ratio increases with decreasing initial subcooling.

$$C = \frac{\sqrt{2 \cdot (1 - \eta_\mathrm{sat}) + 2 \cdot \left[\omega \cdot \eta_\mathrm{sat} \cdot \ln\left(\frac{\eta_\mathrm{sat}}{\eta}\right) - (\omega - 1)\,(\eta_\mathrm{sat} - \eta)\right]}}{\omega\left(\frac{\eta_\mathrm{sat}}{\eta} - 1\right) + 1} \tag{8.11}$$

$$\omega = \frac{x_0 \cdot v_\mathrm{v0}}{\kappa \cdot v_0} + \frac{c_\mathrm{pl0} \cdot T_0 \cdot p_0 \cdot \eta_\mathrm{sat}}{v_0} \left(\frac{v_\mathrm{v0} - v_\mathrm{l0}}{\Delta h_\mathrm{v0}}\right)^2 \cdot N \tag{8.12}$$

$$N = \left(x_0 + c_\mathrm{pl0} \cdot p_0 \cdot T_0 \cdot \eta_\mathrm{sat} \cdot \frac{v_\mathrm{v0} - v_\mathrm{l0}}{{\Delta h_\mathrm{v0}}^2} \cdot \ln\left(\frac{\eta_\mathrm{sat}}{\eta}\right)\right)^{\eta_\mathrm{sat}^{-0.6}} \tag{8.13}$$

$$C = \sqrt{2 \cdot (1 - \eta_\mathrm{sat})} \tag{8.14}$$

4. Sizing inlet piping:
   The pressure drop of the safety valve inlet pipe has to be smaller than 3 % of the gauge set pressure of the safety valve according to DIN EN 13648-3 and DIN EN ISO 4126-9. Otherwise the big pressure loss in the inlet pipe can result in some negative dynamic effects leading to an unstable operation of the safety valve. High frequency vibrations, causing the safety valve to open and close quickly, so-called chattering, drastically reduce its lifetime. The additional heat load of the inlet pipe has only to be considered for design if the inlet pipe exceeds a length of 0.6 m. For the four safety valves SV01 to SV04 the maximum pressure drop of the inlet pipe is reasonably estimated by the following equation:

$$\Delta p = \left(f_\mathrm{in} + f_\mathrm{p} \cdot \frac{L}{d}\right) \cdot 0.5 \cdot \rho \cdot u^2 = \left(f_\mathrm{in} + f_\mathrm{p} \cdot \frac{L}{d}\right) \cdot 0.5 \cdot v \cdot \frac{\dot{m}^2}{A^2} \quad . \tag{8.15}$$

   The friction factor f_in is assumed to be 0.5 for a very sharp angular inlet and the friction factor f_p is approximated as a constant of 0.05, not dependent on the Reynolds

number and the roughness of the wall. For two-phase flow in the inlet pipe the pressure drop is multiplied by a safety coefficient of two.

For rupture disks the pressure drop of the inlet pipe does not need to be checked as rupture disks do not create a resonant system.

5. Sizing outlet piping:
   For the present safety devices there exist no outlet pipes as the nitrogen is directly discharged into the surrounding environment in case of a hazardous event. Due to the risk of oxygen deficiency it is necessary to install an oxygen monitoring system in the laboratory halls including an alarm and evacuation system. Ventilation of the laboratory halls must be possible.

The p-h diagram, see figure 8.13, illustrates the thermodynamic transformation of the fluid for all safety devices. Until the opening of the safety device the thermodynamic transformation of the system can be described as an isochoric transformation, whereas after actuating of the safety device the thermodynamic transformation is isobaric (black lines). The expansion through the safety device itself is approximated by an isenthalpic expansion (black dotted lines for exemplary inlet conditions on the dewing point curve). It is important to emphasize that due to the further heat input after opening of the safety device the inlet conditions of the safety device change; the system can shift isobaricly starting from subcooled liquid through the two-phase area to superheated vapour. But calculations for all safety devices prove that for inlet conditions exactly on the dewing point curve the generated mass flow to be discharged is the greatest. Consequently, all safety devices have to be designed for that case. Table 8.1 shows this fact exemplary for safety valve SV03 with a set pressure of 10 bar. The design of all safety devices at the critical inlet conditions on the dewing point curve are compiled in table 8.2.

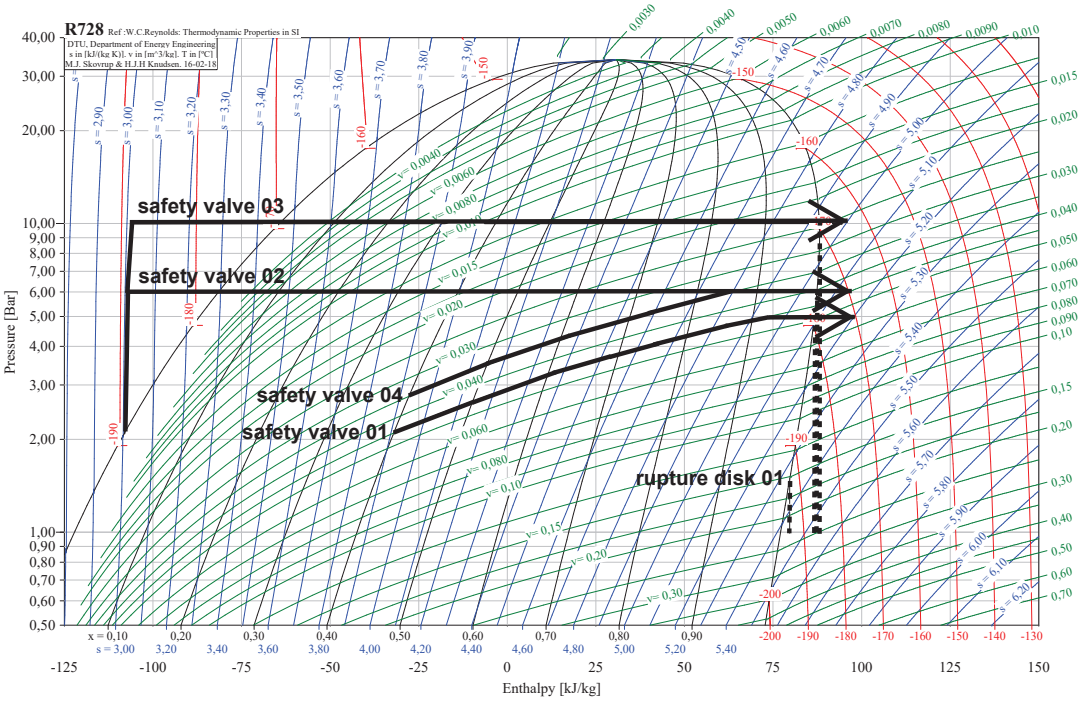

Fig. 8.13: Pressure-enthalpy diagram of nitrogen indicating the thermodynamic transformations of the subsystems of the thermal shield cooling system at a hazardous event, each equipped with a safety valve. Originating from the nominal operation point, the pressure in each subsystem increases along an isochoric transformation, until the valve opens at its set pressure and the transformation becomes isobaric (black lines). All safety devices are designed that they are able to discharge the flow originating from the dewing point curve (black dotted lines).

Tab. 8.1: Required cross-sections of the safety valve SV03 for different inlet conditions at $p_0 = 10\,\mathrm{bar}$.

inlet conditions	cross section in mm^2
subcooled liquid	
$T = 84.12\,\mathrm{K}$	2.98
$T = 100.00\,\mathrm{K}$	4.11
two-phase area	
$x = 10\,\%$	12.16
$x = 50\,\%$	19.73
$x = 90\,\%$	25.03
saturated vapour	
$T = 103.75\,\mathrm{K}$	43.02
superheated vapour	
$T = 113.75\,\mathrm{K}$	40.75
$T = 123.75\,\mathrm{K}$	38.49

Tab. 8.2: Required size of the safety devices in the nitrogen cooling circuit of the thermal shield. For the location of the different safety devices in the circuit refer to figure 8.10.

	rupture disk RD01	safety valve SV01	safety valve SV02	safety valve SV03	safety valve SV04
hazardous event	crack inner vessel	venting insulation vacuum	venting insulation vacuum	venting insulation vacuum	venting insulation vacuum
set pressure in bar	2.1	5	6	10	6
back pressure in bar	1	1	1	1	1
cross section in mm^2	$1.59 \cdot 10^4$	87.35	52.62	43.02	35.08
diameter in mm	142.46	10.55	8.18	7.40	6.68
flow conditions	supersonic	supersonic	supersonic	supersonic	supersonic
length inlet pipe in m	not restricting	0.5	0.2	0.2	0.2
diameter inlet pipe in mm	not restricting	20	20	20	20

9 Conclusion

The large-scale ICARUS T600 detector is designed to detect neutrinos allowing research in the field of neutrino oscillations. Is will be filled with liquid argon and operate at ambient pressure. Consequently, its operation temperature is determined at 87 K, the saturation temperature of argon at ambient pressure. For studying the interactions between neutrinos and argon atoms as precisely as possible, temperature gradients and the resulting convection of the liquid argon inside the detector has to be minimized. Hence, the detector is equipped with a thermal shield, which is actively cooled with boiling nitrogen at the same temperature as the detector. It operates at a pressure of 2.8 bar, which is the saturation pressure of nitrogen at 87 K. The thermal shield should be able to absorb an outer heat flux of $20\,\mathrm{W\,m^{-2}}$ and should have a temperature gradient less than 500 mK. Theoretically, not considering the pressure drop along the cooling circuit, the temperature stays constant during evaporation in the chosen two-phase flow regime. The only temperature change is caused by the small pressure drop along the cooling loop. Due to the strict temperature constraints, it is important to study the pressure drop of the nitrogen two-phase flow along the cooling circuit of the thermal shield in different orientations of the flow in respect to gravity.

An overview of the existing literature of two-phase flow has been given. Characteristic properties of two-phase flow are the flow quality, the void fraction and the flow pattern. The first two properties quantify the proportion of the vapour phase to the total flow. The latter describes the distribution of the two phases at the cross-section of the pipe. The total pressure drop of two-phase flow is the sum of the gravitational, frictional and momentum pressure drop. In contrast to the well-known pressure drop in single-phase liquid or vapour flow, the momentum pressure drop, describing the acceleration of the flow during evaporation, has to be taken into account for two-phase flow. As most of the correlations for the void fraction and the frictional pressure drop of two-phase flow are empirical correlations, it is difficult to utilize them at other conditions they were originally developed for. A lack of a database for the pressure drop of nitrogen two-phase flow at the conditions of the ICARUS thermal shield underlines the need of a further investigation.

An experimental setup has been built in order to determine the pressure drop in nitrogen two-phase flow in a horizontal, vertical upward and vertical downward part. The

measurements have been conducted under quasi-adiabatic conditions and at a pressure of 2.8 bar. The mass velocity has been varied in the range of $20\,\mathrm{kg\,m^{-2}\,s^{-1}}$ to $70\,\mathrm{kg\,m^{-2}\,s^{-1}}$ and it has been scanned through the two-phase area from a flow quality close to zero to flow qualities up to 0.7 depending on the total mass flow rate. At that conditions, chaotic flow occurs in the vertical parts of the test section, whereas the flow in the horizontal part is located in the stratified, wavy or annular flow regime, depending on the flow quality and the mass velocity. In horizontal flow, the frictional pressure drop accounts for the largest contribution to the total pressure drop. For flow qualities higher than 20 % the pressure drop is positively correlated with both, the flow quality and the mass velocity. In vertical upward flow, the gravitational pressure drop is the largest contributor to the total pressure drop. The pressure drop reduces with increasing flow quality, with a sharp decline at low flow qualities. The dependency of the pressure drop on the mass velocity is not as pronounced as in horizontal flow. In vertical downward flow the pressure drop is close to zero over the whole range of flow qualities and mass velocities. It seems that, even in slightly subcooled liquid, when the first vapour bubbles are formed, the gravitational pressure gain due to gravity, well-known from single-phase liquid flow, is eliminated. A Matlab® program has been developed, which computes the two-phase pressure drop of boiling nitrogen in the range of saturation pressures of 2.6 bar to 2.9 bar by coupling the momentum and energy equations. By comparing the experimental data with the calculated data from the Matlab® program, it has been figured out, that the void fraction correlation of Rouhani and the frictional pressure drop model of Müller-Steinhagen and Heck fit best the nitrogen two-phase pressure drop in horizontal and vertical upward flow. A cool down of the experimental setup from room temperature is only possible if there is now flow restriction by a needle valve. The established Matlab® program is used to calculate the two-phase flow pressure drop in one 11 m long cooling loop of the ICARUS thermal shield. With an inner pipe diameter of 10 mm, an inlet flow quality of 10 % and a heat load of $20\,\mathrm{W\,m^{-2}}$, the total pressure drop of the loop is 98.5 mbar. The temperature drop related to this pressure drop is less than 400 mK, fulfilling the given requirements. However, there exists a risk that the system destabilizes itself owing to no or a negative correlation of the pressure drop to the mass velocity. By decreasing the inner pipe diameter to 6 mm, the flow in the horizontal part is shifted towards the annular flow regime and the destabilizing effect is eliminated. The total pressure drop over the loop rises to 108 mbar, but the corresponding temperature drop still stays below 500 mK. A design of the whole nitrogen cooling circuit of the thermal shield has been proposed. A bypass around the actual detector is essential for cool down. It is crucial to properly equip the cooling circuit with correspondingly sized safety valves and rupture disk, as high pressure can be built up in cryogenic systems by additional heat input.

List of Tables

List of Figures

Bibliography

[1] About CERN, 06.02.2016. URL `http://home.cern/about`.

[2] ICARUS neutrino experiment to move to Fermilab, 06.02.2016. URL `http://press.web.cern.ch/press-releases/2015/04/icarus-neutrino-experiment-move-fermilab`.

[3] Christine Sutton. *Raumschiff Neutrino: Die Geschichte eines Elementarteilchens.* Birkhäuser, Basel, Berlin, 1994.

[4] Bogdan Povh, Klaus Rith, Christoph Scholz, Frank Zetsche, and Werner Rodejohann. *Particles and Nuclei: An Introduction to the Physical Concepts.* Graduate Texts in Physics. Springer, Berlin, Heidelberg, 7th edition, 2015.

[5] private communication.

[6] Josef M. Gaßner. Urknall, Weltall und das Leben: Neutrino-Oszillation - Physik Nobelpreis 2015, 17.06.2016. URL `https://www.youtube.com/watch?v=UVovr3_Mq-I`.

[7] A. Zani. ICARUS and Sterile Neutrinos. *Nuclear and Particle Physics Proceedings*, 265-266:330–332, 2015.

[8] Maurizio Bonesini. The WA104 Experiment at CERN. *Journal of Physics: Conference Series*, 650: 012015, 2015.

[9] C. Rubbia. The liquid-argon time projection chamber: A new concept for neutrino detectors. *European Organization for Nuclear Research, EP Internal Report*, 77(8), 1977.

[10] D. H. Beggs and J. P. Brill. A Study of Two-Phase Flow in Inclined Pipes. *Journal of Petroleum Technology*, 25(05):607–617, 2013.

[11] John-R. Thome. *Engineering Data Book III.* Wolverine Tube Inc., 2004.

[12] *VDI Heat Atlas.* Springer, Berlin, Heidelberg, 2010.

[13] Yemada Taitel and A. E. Dukler. A model for predicting flow regime transitions in horizontal and near horizontal gas-liquid flow. *AIChE Journal*, 22(1):47–55, 1976.

[14] Franz Mayinger. *Strömung und Wärmeübergang in Gas-Flüssigkeits-Gemischen.* Springer, Wien, 1982.

[15] G. F. Hewitt and D. N. Roberts. Studies of two-phase flow patterns by simultaneous X-ray and flash fotography. *United Kingdom Atomic Energy Authority Research Group Memorandum*, 1969.

[16] Jesús Moreno Quibén and John R. Thome. Flow pattern based two-phase frictional pressure drop model for horizontal tubes, Part II: New phenomenological model. *International Journal of Heat and Fluid Flow*, 28(5):1060–1072, 2007.

[17] Yu Xu and Xiande Fang. Correlations of void fraction for two-phase refrigerant flow in pipes. *Applied Thermal Engineering*, 64(1-2):242–251, 2014.

[18] S. Levy. Steam Slip—Theoretical Prediction From Momentum Model. *Journal of Heat Transfer*, 82 (2):113, 1960.

[19] Hideo Fujie. A relation between steam quality and void fraction in two-phase flow. *AIChE Journal*, 10(2):227–232, 1964.

[20] Huq, Realzu, John Loth L. Analytical two-phase flow void prediction method. *Journal of Thermophysics and Heat Transfer*, 6(1):139–144, 1992.

[21] B. Chexal and G. Lellouche. A Full-Range Drift-Flux Correlation for Vertical Flows (Revision 1). *Electric Power Research Institut (EPRI)*, 1986.

[22] Bindi Chexal, Jeff Horowitz, Gail McCarthy, Mati Merilo, Jean-Pierre Sursock, Palo Alto, Jim Harisson, Craig Peterson, John Shatford, Dan Hughes, Mostafa Ghiaasiaan, Vijay Dhir, Wolfgang Kastner, and Wolfgang Köhler. Two-Phase Pressure Drop Technology for Design and Analysis. *Electric Power Research Institut (EPRI)*, 1999.

[23] S.Z Rouhani and E. Axelsson. Calculation of void volume fraction in the subcooled and quality boiling regions. *International Journal of Heat and Mass Transfer*, 13(2):383–393, 1970.

[24] Findlay J. Zuber N. Average volumetric concentration in two-phase flow. *Journal of Heat Transfer*, pages 453–462, 1965.

[25] Jesús Moreno Quibén and John R. Thome. Flow pattern based two-phase frictional pressure drop model for horizontal tubes. Part I: Diabatic and adiabatic experimental study. *International Journal of Heat and Fluid Flow*, 28(5):1049–1059, 2007.

[26] Paul Coddington and Rafael Macian. A study of the performance of void fraction correlations used in the context of drift-flux two-phase flow models. *Nuclear Engineering and Design*, 215(3):199–216, 2002.

[27] Z. Rouhani. Modified Correlations for Void and Twp-Phase Pressure Drop. *AB Atomenergi*, (AE-RTV-841), 1974.

[28] A. Khalil, G. McIntosh, and R. W. Boom. Experimental measurement of void fraction in cryogenic two phase upward flow. *Cryogenics*, 21(7):411–414, 1981.

[29] F. Garcia, R. Garcia, J.C Padrino, C. Mata, J.L Trallero, and D.D Joseph. Power law and composite power law friction factor correlations for laminar and turbulent gas–liquid flow in horizontal pipelines. *International Journal of Multiphase Flow*, 29(10):1605–1624, 2003.

[30] Yu Xu, Xiande Fang, Xianghui Su, Zhanru Zhou, and Weiwei Chen. Evaluation of frictional pressure drop correlations for two-phase flow in pipes. *Nuclear Engineering and Design*, 253:86–97, 2012.

[31] Dongsheng Chen and Yumei Shi. Study on two-phase pressure drop of LNG during flow boiling in a 8mm horizontal smooth tube. *Experimental Thermal and Fluid Science*, 57:235–241, 2014.

[32] J. Wu, T. Koettig, Ch. Franke, D. Helmer, T. Eisel, F. Haug, and J. Bremer. Investigation of heat transfer and pressure drop of CO2 two-phase flow in a horizontal minichannel. *International Journal of Heat and Mass Transfer*, 54(9-10):2154–2162, 2011.

[33] L. Friedel. Improved frictional pressure drop correlations for horizontal and vertical two phase flow. *3R International*, 18(7):485–491, 1979.

[34] H. Müller-Steinhagen and K. Heck. A simple friction pressure drop correlation for two-phase flow in pipes. *Chemical Engineering and Processing: Process Intensification*, 20(6):297–308, 1986.

[35] R. Gronnerud. Investigation of liquid hold-up, flow resistance and heat transfer in circulation type evaporators: Part IV. Two-phase flow resistance in boiling refrigerants. *Bulletin de l'Institut du Froid*, 1:127–138, 1972.

[36] H. Müller-Steinhagen and D. Steiner. Druckverlust bei der Strömung von Argon und Stickstoff in einem horizontalen Verdampferrohr. *VT Verfahrenstechnik*, 9:512–523, 1983.

[37] DIN EN 13648-3. Crogenic vessels - Safety devices for protection against excessive pressure Part 3: Determination of required discharge - Capacity and sizing, 2003.

[38] DIN EN ISO 4126. Safety devices for protection against excessive pressure, 2013.

[39] W. Lehmann. Sicherheitstechnische Aspekte bei Auslegung und Betrieb von LHE-badgekühlten Supraleiter-Magnetkryostaten. In *Vortrag DKV-Jahrestagung 1990*.

[40] W. Lehmann and G. Zahn. Safety aspects for LHE cryostats and LHE containers. In *International Croygenic Engineering Conference 1978*, volume 7, pages 569–579.

[41] C. Joseph Leung. Easily Size Relieve Devices and Piping for Two-Phase Flow. *Chemical Engineering Process CEP and AIChE publication*, 7(12):28–50, 1996.

[42] C. Joseph Leung. The Omega Method for Discharge Rate Evolution. In *International Symposium on Runaway Reactions and Pressure Relief Design 1995*.

[43] J. Schmidt. Sizing of nozzles, venturis, orifices, control and safety valves for initially sub-cooled gas/liquid two-phase flow – The HNE-DS method. *Forschung im Ingenieurwesen*, 71(1):47–58, 2007.

Used applications

[1] NIST Reference Fluid Thermodynamic and Transport Properties Database online available: http://webbook.nist.gov/chemistry/fluid/

[2] CoolPack of IPU

[3] AutoCAD Mechanical 2013

[4] Autodesk Inventor Professional 2014

[5] MATLAB R2014a

A Components of the small-scale experimental setup

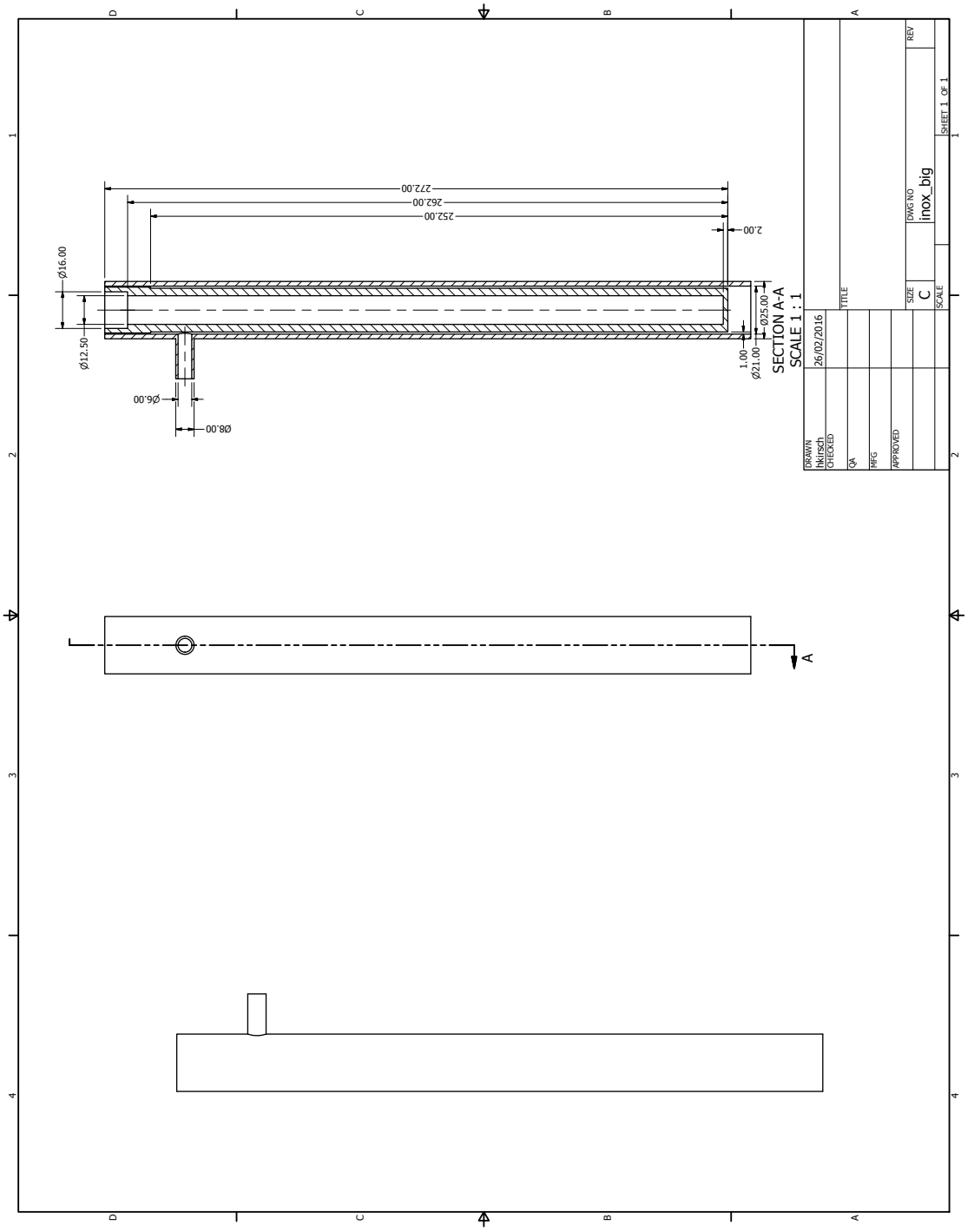

Fig. A.1: Design of the cartridge heater system EH002. The cartridge heater consists of two concentric cylinders forming an annular gap for the flow to pass through. The heating source is placed in the inner cylinder.

D

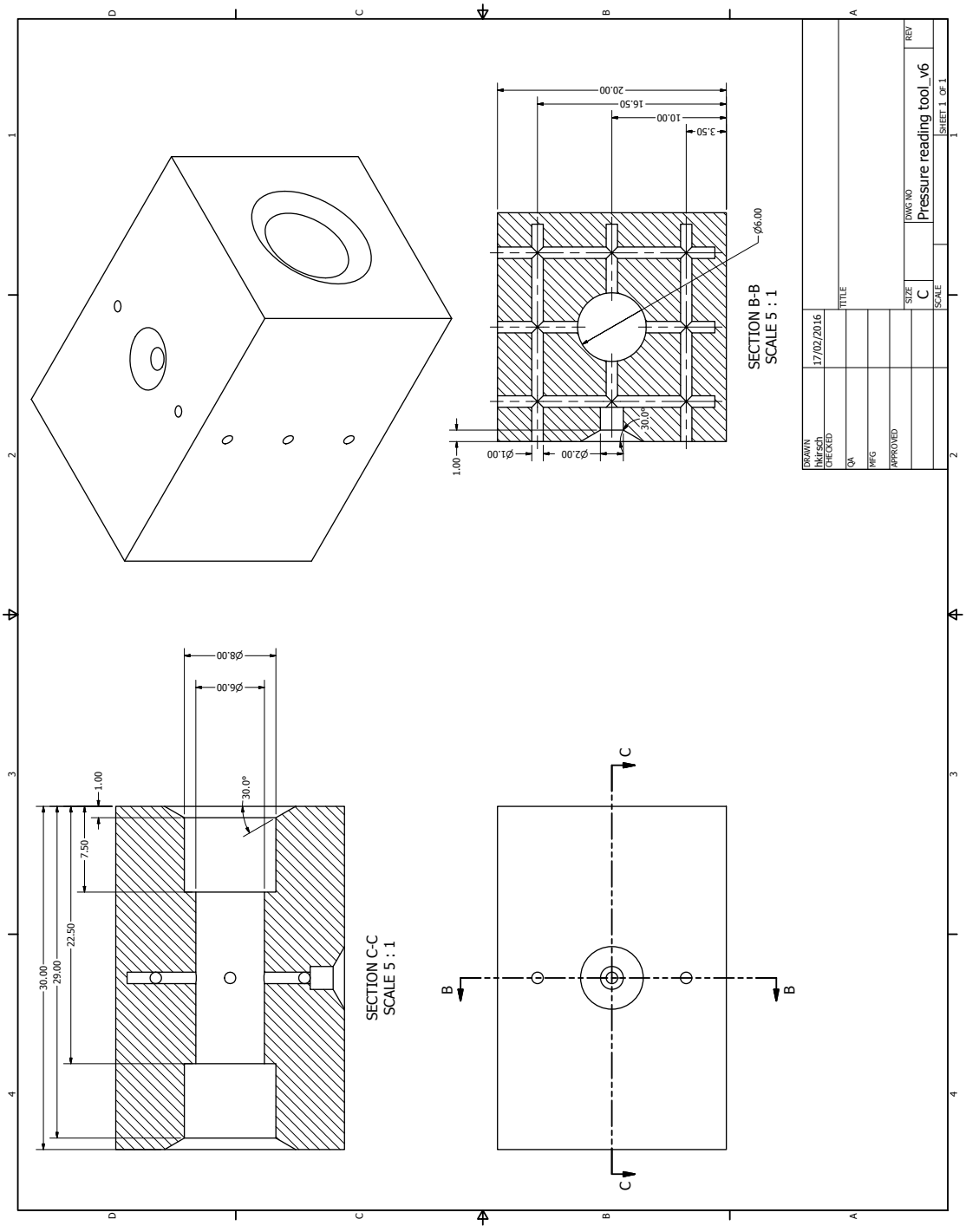

Fig. A.2: Design of the pressure tap device. The pressure drop is averaged over the pipe cross-section by means of four evenly distributed holes.

B Matlab® program

The Matlab® program calculates the pressure drop of nitrogen two-phase flow at saturation pressures in the range of 2.6 bar to 2.9 bar. Variables in red have to be specified by the user. Different void fraction and frictional pressure drop correlations (highlighted in blue) can be embedded into the program.

F

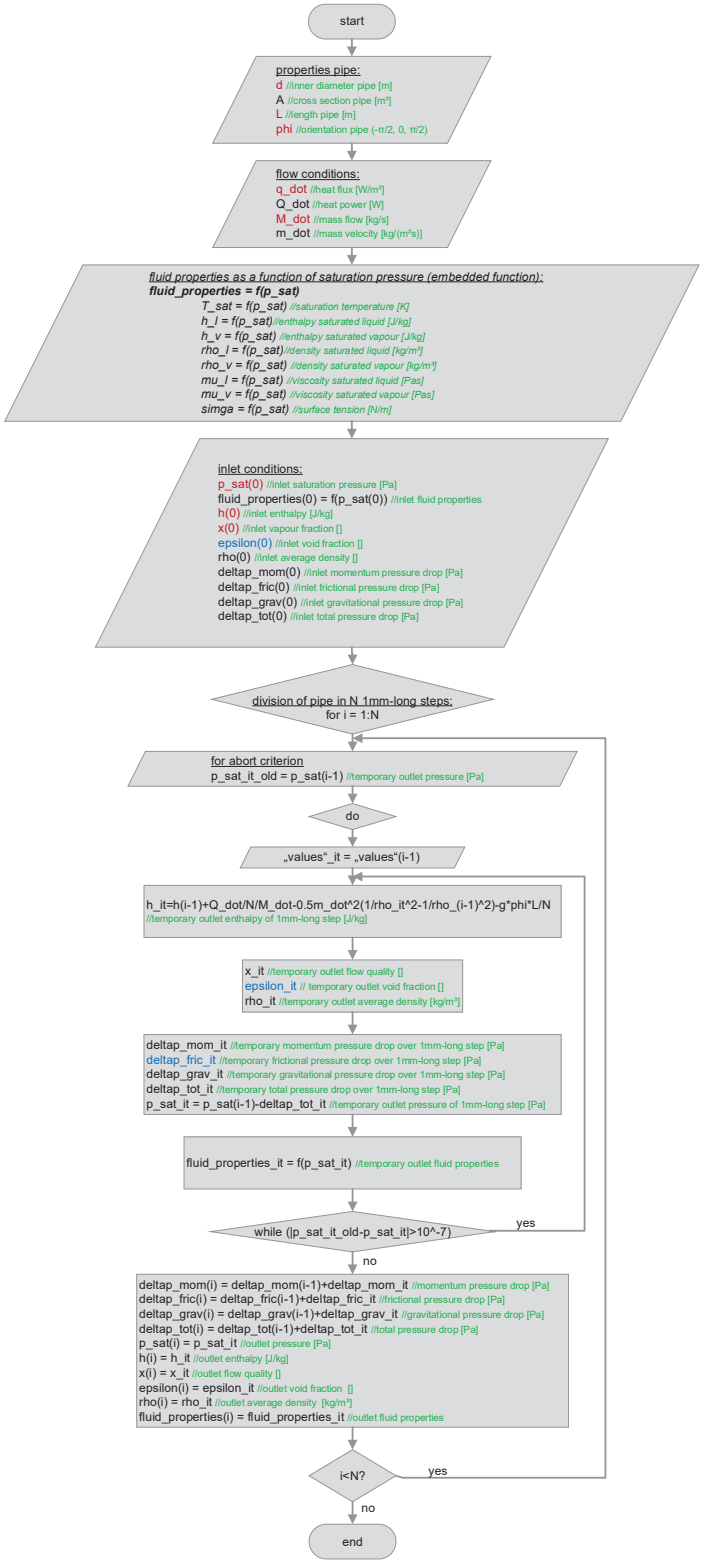

Fig. B.1: Simplified flow chart of the Matlab® program.

C Correlations used for two-phase flow pressure drop

void fraction correlation according to Rouhani [17]:

$$\epsilon = \frac{J_\mathrm{v}}{C_0 \cdot J + U_\mathrm{vj}} \tag{C.1}$$

$$J = J_\mathrm{v} + J_\mathrm{l} = \frac{x \cdot G}{\rho_\mathrm{v}} + \frac{(1-x) \cdot G}{\rho_\mathrm{l}} \tag{C.2}$$

$$C_0 = 1 + 0.2 \cdot (1-x) \tag{C.3}$$

$$U_\mathrm{vj} = 1.18 \cdot \left(\frac{\mathrm{g} \cdot \sigma \cdot (\rho_\mathrm{l} - \rho_\mathrm{v})}{\rho_\mathrm{l}^2} \right)^{0.25} \tag{C.4}$$

frictional pressure drop model according to Müller-Steinhagen and Heck [30]:

$$Re_{\mathrm{v0}} = \frac{G \cdot d}{\mu_{\mathrm{v}}} \tag{C.5}$$

$$Re_{\mathrm{l0}} = \frac{G \cdot d}{\mu_{\mathrm{l}}} \tag{C.6}$$

$$f_{\mathrm{i0}} = \frac{64}{Re_{\mathrm{0i}}} \quad \text{for} \quad Re_{\mathrm{i0}} \leq 1187 \tag{C.7}$$

$$f_{\mathrm{i0}} = 0.25 \cdot \left(log \left(\frac{150.39}{Re_{\mathrm{i0}}^{0.98865}} - \frac{152.66}{Re_{\mathrm{i0}}} \right) \right)^{-2} \quad \text{for} \quad Re_{\mathrm{i0}} > 1187 \tag{C.8}$$

$$\left(\frac{\Delta p}{\Delta L} \right)_{\mathrm{i}} = f_{\mathrm{i0}} \frac{G^2}{2 \cdot d \cdot \rho_{\mathrm{i}}} \tag{C.9}$$

$$Y^2 = \frac{\left(\frac{\Delta p}{\Delta L} \right)_{\mathrm{v}}}{\left(\frac{\Delta p}{\Delta L} \right)_{\mathrm{l}}} \tag{C.10}$$

$$\phi_{\mathrm{l}}^2 = Y^2 \cdot x^3 + (1-x)^{\frac{1}{3}} \left(1 + 2 \cdot x \cdot \left(Y^2 - 1 \right) \right) \tag{C.11}$$

$$\left(\frac{\Delta p}{\Delta L} \right)_{\mathrm{2ph}} = \phi_{\mathrm{l}}^2 \cdot \left(\frac{\Delta p}{\Delta L} \right)_{\mathrm{l}} \tag{C.12}$$